

High speed perfusion imaging based on laser speckle fluctuations

Copyright © 2010 by Matthijs Draijer

This research is supported by the Dutch Technology Foundation STW, which is the applied science division of NWO, and the Technology Programme of the Ministry of Economic Affairs (project number 6443).

Cover design by Benne Draijer.

Fonts : Yanone Kaffeesatz (Jan Gerner, www.yanone.de) & Mentone (Jan Schmoeger, www.paragraph.com.au).

Printed by Ridderprint, Ridderkerk, The Netherlands, 2010

ISBN 978-90-365-2979-2

HIGH SPEED PERFUSION IMAGING BASED ON LASER SPECKLE FLUCTUATIONS

PROEFSCHRIFT

ter verkrijging van
de graad van doctor aan de Universiteit Twente,
op gezag van de rector magnificus,
prof. dr. H. Brinksma,
volgens besluit van het College voor Promoties
in het openbaar te verdedigen
op vrijdag 5 maart 2010 om 15.00 uur

door

Matthijs Johannes Draijer

geboren op 22 maart 1980
te Almelo

Dit proefschrift is goedgekeurd door:

prof. dr. A. G. J. M. van Leeuwen (promotor)

dr. ir. W. Steenbergen (co-promotor)

Spreuken 2:6

Contents

- 1 Introduction** 1
 - 1.1 General Introduction 2
 - 1.2 Scope of the thesis 3
 - 1.3 Overview of this thesis 4
 - References 5

- 2 Review of laser speckle contrast techniques for visualizing tissue perfusion** 9
 - 2.1 Introduction 10
 - 2.2 Speckle contrast 11
 - 2.2.1 What are speckles ? 11
 - 2.2.2 What is speckle contrast ? 12
 - 2.3 Theories relating speckle contrast to particle speed 13
 - 2.4 Speckle contrast flow measurement techniques 16
 - 2.4.1 Double and single exposure speckle photography 16
 - 2.4.2 Laser speckle contrast analysis (LASCA) 17
 - 2.4.3 Laser speckle imaging (LSI) 20

Contents

2.4.4	Other techniques	22
2.5	Applications	24
2.6	Comparison with laser Doppler perfusion imaging	25
2.7	Conclusions	29
	References	30
3	The Twente Optical Perfusion Camera: system overview and performance for video rate laser Doppler perfusion imaging	39
3.1	Introduction	40
3.2	The Twente Optical Perfusion Camera	42
3.2.1	Camera selection based on signal-to-noise ratio	42
3.2.2	Noise correction	47
3.2.3	Speed performance of system	48
3.3	Demonstration of real time imaging capabilities	49
3.3.1	Methods and results	51
3.4	Discussion	54
3.5	Conclusion	58
	References	58
4	Burn imaging with a whole field laser Doppler perfusion imager based on a CMOS imaging array	63
4.1	Introduction	64
4.2	Subjects and methods	66
4.2.1	Patients	66
4.2.2	Equipment	66

4.2.3	Clinical methodology	67
4.3	Results	68
4.3.1	Partial thickness burns	68
4.3.2	Blisters	69
4.3.3	Dead skin	71
4.3.4	Crusts	71
4.3.5	Comparison with the PIM II	72
4.4	Discussion	75
4.4.1	General aspects	75
4.4.2	Blisters	76
4.4.3	Dead skin	76
4.4.4	Crust	76
4.4.5	PIM II	77
4.5	Conclusion	78
	References	78
5	Time domain algorithm for accelerated determination of the first order moment of photo current fluctuations in high speed laser Doppler perfusion imaging	83
5.1	Introduction	84
5.2	Method	86
5.2.1	Theory	86
5.2.2	Materials	88
5.3	Results	91
5.4	Discussion	91

Contents

5.4.1	Comparison of both algorithms	91
5.4.2	Calculation speed	96
5.4.3	Implementing TD on high speed CMOS-cameras	96
5.5	Conclusion	97
	References	97
6	Relation between the contrast in time integrated dynamic speckle patterns and the power spectral density of their temporal intensity fluctuations	103
6.1	Introduction	104
6.2	Theory	106
6.2.1	Transferfunction	106
6.2.2	Contrast	106
6.3	Results	109
6.4	Discussion	110
6.5	Conclusion	113
	References	113
7	Summary and Outlook	117
7.1	Summary	118
7.2	Outlook	121
7.2.1	CMOS technology	121
7.2.2	LASCA versus LDPI	122
7.2.3	Applications	123
	References	124

Samenvatting	125
Bibliografie	128
Dankwoord	129
Publications	133
Curriculum Vitae	135

1

Introduction

Abstract – In this chapter an introduction will be given to the research areas of high-speed laser Doppler perfusion imaging and laser speckle contrast techniques. Furthermore, the aim of the performed research will be introduced, and finally an overview of the topics in this thesis will be given.

1.1 General Introduction

Noninvasive imaging of blood flow in tissue is of major importance for certain applications in dermatology [1], neurology [2], surgery [3] and wound care [4]. Over recent decades, several techniques have been developed for imaging tissue perfusion. Most of these techniques exploit the random interference pattern generated from diffusely backscattered light from the skin, generally known as speckle pattern.

The most well-known technique using this speckle pattern is laser Doppler perfusion imaging (LDPI) [5, 6]. In LDPI the skin is illuminated with coherent laser light. A fraction of the laser light interacts with moving red blood cells and obtains a Doppler shift. A mixture of Doppler shifted and unshifted light interferes on a detector, resulting in a speckle pattern which changes over time. This leads to the generation of a photocurrent that fluctuates in time. The moments of the power spectrum $S(\omega)$ of this photoelectric current are given by :

$$M_i \propto \int_0^{\infty} \omega^i S(\omega) d\omega \quad (1.1)$$

In LDPI the zeroth order moment ($i = 0$) is a measure for the concentration of red blood cells whereas the first order moment ($i = 1$) is a measure for the flux or perfusion [7].

Currently, laser speckle contrast analysis (LASCA) and other laser speckle contrast techniques are gaining interest as alternative methods for perfusion

imaging [8, 9]. Laser speckle contrast techniques are based on the spatial and temporal statistics of the speckle pattern. The contrast in a speckle pattern is defined as :

$$C \equiv \frac{\sigma}{\langle I \rangle} = \frac{\sqrt{\langle I^2 \rangle - \langle I \rangle^2}}{\langle I \rangle} \quad (1.2)$$

where the brackets denote averaging. The motion of particles in the illuminated medium causes fluctuations in the speckle pattern when recorded with an imaging array, using a long integration time. These intensity fluctuations blur the image and reduce the contrast to an extent that is related to the speed of the particles inside the illuminated medium, such as moving red blood cells.

1.2 Scope of the thesis

Till recently the largest advantage of LASCA was its being a full-field technique, whereas LDPI was a scanning technique. This scanning mode resulted in long measurement times, which made LDPI less favorable for the clinical environment. This disadvantage decreased when LDPI became a full-field technique by the introduction of high speed CMOS cameras for the detection of the Doppler-shifted light [10–12]. From that moment on, both techniques had a measurement time in the millisecond range. The introduction of the high-speed CMOS-cameras in LDPI directly reveals another advantage of LASCA over LDPI. To perform LASCA measurements an inexpensive camera which can achieve a frame-rate of 200 Hz is sufficient, whereas for LDPI, a state-of-the-art high-speed camera which can achieve a frame-rate of about 25 kHz is needed.

In this thesis we study the implications of the implementation of a CMOS-camera in a LDPI measurement-setup, study the application of full field LDPI on burn diagnosis, review laser speckle contrast techniques and present a comparison of LDPI with LASCA.

1.3 Overview of this thesis

A review of the contribution of laser speckle contrast techniques to the field of perfusion visualization and a discussion of the development of these techniques is given in **chapter 2**. In this chapter the working principle of LASCAs is discussed and the development of laser speckle contrast techniques over the last decades is reviewed.

In commercially available LDPI devices the area under investigation is scanned with a narrow laser beam and consequently, obtaining a perfusion image of 64×64 pixels takes approximately 3 minutes. This long scanning time impedes the observation of fast perfusion changes, for instance during reperfusion after occlusion. To obtain real time reperfusion images a refresh rate of approximately 25 Hz is needed. Also from the perspective of the patient, a short imaging time, e.g., for burn patients, and in general for young children and elder patients, is beneficial. So, in **chapter 3** the Twente Optical Perfusion Camera (TOPCam), a LDPI measurement setup based on CMOS technology, is presented and measurements are shown. Unlike previous devices, the TOPCam is able to acquire a perfusion image within milliseconds, and to perform video rate perfusion imaging. Various instrumental aspects will be discussed and performance studies on phantoms and *in-vivo* measurements will be presented.

Proper determination of the burn depth is crucial for the choice of the optimal wound treatment. In burns with an intermediate depth (also called partial thickness burns), the early prognostication of the likely burn wound outcome is difficult during the first days after injury. In literature, several potential objective methods to determine burn depth in an early stage after injury are reported, one of which is LDPI [13–15]. The superficial partial thickness burns have a more active microcirculation compared to normal 'unaffected' skin, while the microcirculation in deep partial thickness burn wounds is impaired or lost. These differences are used in the burn assessment with LDPI. In **chapter 4** a study is presented to evaluate the capability and efficacy of the TOPCam to measure perfusion differences in burn wounds. Since blisters, curvature and crusts can influence the perfusion values in the LDPI measurement, the effects of different wound appearances are investigated.

In **chapter 5**, a Time Domain algorithm is presented for determining the first order spectral moment. Nowadays the perfusion in one pixel is cal-

culated by recording a complete time signal (e.g. 512 or 1024 points), determine the power spectrum using the Fast Fourier Transform, and obtain the first order moment of the power spectrum as a measure for the flux or perfusion. In this way, calculating the perfusion is time consuming and inefficient in terms of memory and data transport: because in this procedure all raw speckle images are needed simultaneously, and for each pixel the spectrum has to be taken for each pixel and the spectrum has to be squared and integrated over all frequencies to obtain one number for the perfusion. We evaluated another approach in which a calculation algorithm for the first order moment working in the time domain is utilized. This Time Domain algorithm involves less computational steps and requires less data to be transported and stored.

The physical model behind LDPI by Bonner and Nossal [7] has shown that, for low blood concentrations, the concentration of red blood cells and their average velocity are both linearly represented by the zeroth and first order moment. The physical model behind laser speckle contrast flowmetry are inspired by Dynamic Light Scattering theories, implying assumptions regarding the dynamics of the particles and the associated optical intensity correlations. In **chapter 6** we present a theory which connects the contrast in time integrated dynamic speckle patterns (e.g. laser speckle contrast techniques) and the power spectral density of temporal intensity fluctuations of non-integrated speckle patterns (e.g. laser Doppler perfusion imaging) without prior assumptions regarding the speed distribution of particles and the extent of multiple scattering.

Finally, a summary and outlook of the research of this thesis will be given in **chapter 7**.

References

1. S. W. Kim, S. C. Kim, K. C. Nam, E. S. Kang, J. J. Im & D. W. Kim (2008). "A new method of screening for diabetic neuropathy using laser doppler and photoplethysmography". *Medical & Biological Engineering & Computing*, **46**, 61–67.
2. A. Porebska, P. Nowacki, K. Safranow & M. Nowik (2008). "Hemodynamic blood flow disturbances in the middle cerebral arteries in patients with atrial fibrillation during acute ischemic stroke". *Clinical Neurology and Neurosurgery*, **110**(5), 434–440.

3. F. G. Bechara, M. Sand, M. Stuecker, D. Georgas, K. Hoffmann & P. Altmeyer (2008). “Laser Doppler scanning study of axillary skin before and after liposuction curettage in patients with focal hyperhidrosis”. *Dermatology*, **216**(2), 173–179.
4. E. La Hei, A. Holland & H. Martin (2006). “Laser Doppler imaging of paediatric burns: Burn wound outcome can be predicted independent of clinical examination”. *Burns*, **32**, 550–553.
5. T. J. H. Essex & P. O. Byrne (1991). “A laser Doppler scanner for imaging blood flow in skin”. *Journal of Biomedical Engineering*, **13**, 189–194.
6. K. Wårdell, A. Jakobsson & G. E. Nilsson (1993). “Laser Doppler perfusion imaging by dynamic light scattering”. *IEEE Transactions on biomedical Engineering*, **40**(4), 309–316.
7. R. Bonner & R. Nossal (1981). “Model for laser Doppler measurements of blood flow in tissue”. *Applied Optics*, **20**(12), 2097–2107.
8. J. D. Briers (2001). “Laser Doppler, speckle and related techniques for blood perfusion mapping and imaging”. *Physiological Measurements*, **22**, R35–R66.
9. J. D. Briers (2007). “Laser speckle contrast imaging for measuring blood flow”. *Optica Applicata*, **XXXVII**, 139–152.
10. A. Serov, W. Steenbergen & F. F. M. de Mul (2002). “Laser Doppler perfusion imaging with a complimentary metal oxide semiconductor image sensor”. *Optics Letters*, **27**(5), 300–302.
11. A. Serov, B. Steinacher & T. Lasser (2005). “Full-field laser Doppler perfusion imaging and monitoring with an intelligent CMOS camera”. *Optics Express*, **13**(10), 3681–3689.
12. A. Serov & T. Lasser (2005). “High-speed laser Doppler perfusion imaging using an integrating CMOS image sensor”. *Optics Express*, **13**(17), 6416–6428.
13. A. Mandal (2006). “Burn wound depth assessment – is laser Doppler imaging the best measurement tool available?” *International Wound Journal*, **3**(2), 138–144.

14. E. J. Droog, W. Steenbergen & F. Sjöberg (2001). “Measurement of depth of burns by laser Doppler perfusion imaging”. *Burns*, **27**, 561–568.
15. F. W. Kloppenberg, G. I. Beerthuisen & H. J. ten Duis (2001). “Perfusion of burn wounds assessed by laser Doppler imaging is related to burn depth and healing time.” *Burns*, **27**, 359–363.

2

Review of laser speckle contrast techniques for visualizing tissue perfusion

This chapter has been published as : M.J. Draijer, E. Hondebrink, T.G. van Leeuwen, and W. Steenbergen (2009)
"Review of laser speckle contrast techniques for visualizing tissue perfusion", *Lasers in Medical Science*, **24(4)**,
639-651.

Abstract – When a diffuse object is illuminated with coherent laser light, the backscattered light will form an interference pattern on the detector. This pattern of bright and dark areas is termed a *speckle pattern*. When there is movement in the object, the speckle pattern will change over time. Laser speckle contrast techniques use this change in speckle pattern to visualize the tissue perfusion.

We present and review the contribution of laser speckle contrast techniques to the field of perfusion visualization and discuss the development of the techniques.

2.1 Introduction

Imaging blood flow in the tissue is of major importance in the clinical environment [1–10]. Over recent decades, several techniques have been developed for imaging tissue perfusion. Most of these techniques [10–13] exploit the interference pattern generated from diffusely backscattered light from the skin [14]. Currently, laser speckle contrast techniques are gaining interest [15, 16]. Laser speckle contrast techniques are based on the spatial and temporal statistics of the speckle pattern. The motion of particles in the illuminated medium causes fluctuations in the speckle pattern on the detector. These intensity fluctuations blur the image and reduce the contrast to an extent that is related to the speed of the illuminated objects, such as moving red blood cells. In this paper, we will present the principles and various implementations of the speckle contrast method, review the contribution of laser speckle contrast techniques to the field of perfusion imaging and describe their technical development.

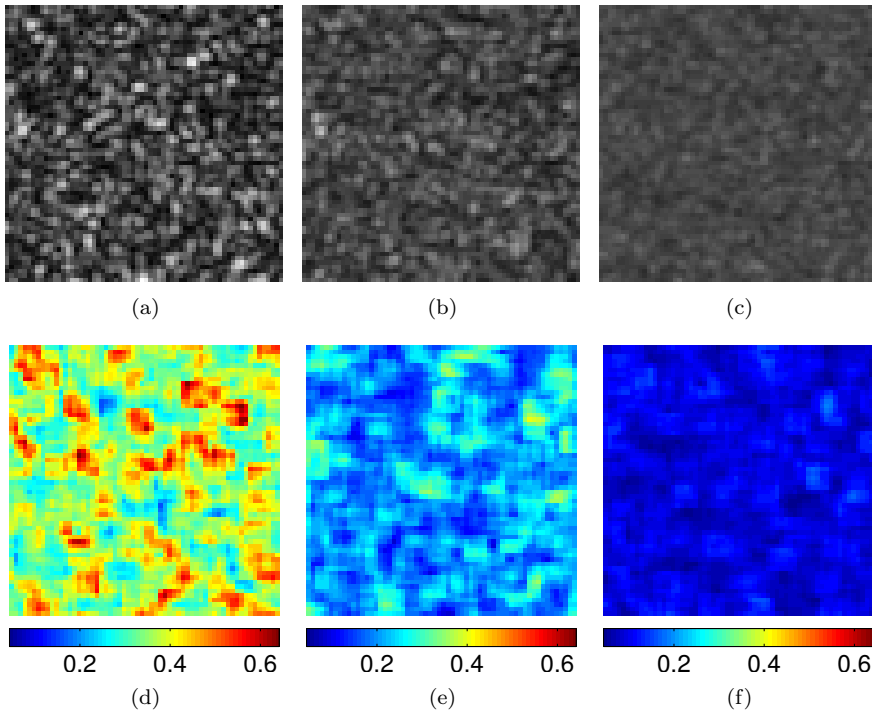


Figure 2.1: (a), (b) and (c) Simulated blurred speckle patterns with an exposure time of 1, 5 and 25 ms respectively, (d), (e) and (f) conjugated contrast images, with contrast values calculated for 5×5 pixels. The contrast value is shown in the colorbar.

2.2 Speckle contrast

2.2.1 What are speckles ?

When an optically rough object is illuminated with coherent laser light and the diffusely backscattered light is collected on a screen, the backscattered light will create an interference pattern on this screen. This interference pattern consists of bright and dark areas; the so-called *speckles*. If the object does not move and the laser is stable, the interference pattern does not change over time, and the pattern is termed a *static speckle pattern*. If the

object moves or particles move within the medium, the interference pattern will change in time and the pattern is termed *dynamic*. This dynamic behavior is mainly caused by the Doppler shifts of the light that interacts with the moving particles. Figure 2.1(a) shows a simulated speckle pattern formed when the diffusely backscattered light is emitted from a circular area [17].

2.2.2 What is speckle contrast ?

Speckle flow techniques are based on the changes over time of the dynamic speckle pattern generated by motion in the sample. In these techniques, this changing speckle pattern is recorded with a camera which has an integration time in the order of the speckle decorrelation-time (i.e. in the millisecond range). Due to the long integration time compared to the typical decorrelation-time of the speckle pattern, the speckle pattern will be blurred in the recorded image. The level of blurring is quantified by the speckle contrast. The speckle contrast C is usually defined as the ratio of the standard deviation σ of the intensity I to the mean intensity $\langle I \rangle$ of the speckle pattern:

$$C \equiv \frac{\sigma}{\langle I \rangle} = \frac{\sqrt{\langle I^2 \rangle - \langle I \rangle^2}}{\langle I \rangle} \quad (2.1)$$

If there is no or little movement in the object, there will be no or only a little blurring. Goodman and Parry [18] showed that for a static speckle pattern, under ideal conditions (i.e. perfectly monochromatic and polarized waves and absence of noise) the standard deviation σ equals the mean intensity $\langle I \rangle$ and the speckle contrast is equal to unity, which is the maximum value for the contrast. Such a speckle pattern is termed “*fully developed*”. When there is movement in the object, the speckle pattern will be blurred and the standard deviation of the intensity will be small compared to the unchanged mean intensity, resulting in a reduced speckle contrast. Figure 2.1 shows 3 simulated speckle images with different exposure times and their corresponding contrast maps. The latter are obtained by calculating the contrast over an area of 5×5 pixels. The speckle images are simulated by making use of the concept of a copula [17]: a circular region in a square matrix is filled with complex numbers of unity amplitude and uniformly distributed phases. After Fourier transforming the matrix, and multiplying it point-by-point by its complex conjugate, an artificial speckle pattern is generated. By shifting the circular region with complex numbers one column

each time and recalculating the speckle pattern, a dynamic speckle pattern can be generated. The speckle pattern is decorrelated if all the complex numbers in the circular region are changed (i.e. after the same amount of steps as the diameter of the circular region). So the diameter of the circular region can be related to the speckle decorrelation time, in this way different exposure times can be simulated.

2.3 Theories relating speckle contrast to particle speed

A dynamic speckle pattern can be described in terms of a power spectrum of the intensity fluctuations. In the time domain, an analogous description is by the autocorrelation function of the intensity fluctuations. An important feature of such a temporal correlation function is the decorrelation time. Under the assumption of a random Gaussian or Lorentzian velocity distribution with a mean around zero, the decorrelation time τ_c can be linked to the decorrelation velocity v_c [19–21] by:

$$v_c = \frac{\lambda}{2\pi\tau_c} \quad (2.2)$$

with λ the laser wavelength. Using laser light in the visible range, this relation reduces to $v_c \approx 0.1/\tau_c \text{ } \mu\text{m/s}$. Bonner and Nossal [22] took more factors such as particle-size into account and reduced the relation to $v_c \approx 3.5/\tau_c \text{ } \mu\text{m/s}$. So the decorrelation velocity predicted by Bonner and Nossal differs by one and a half orders of magnitude from the values predicted by Briers and Webster. Which of these relations best predicts the decorrelation velocity is yet unknown.

For laser speckle contrast techniques, the particle velocity and/or the speckle decorrelation time need to be related to the speckle contrast. Ramirez-San-Juan *et al.* [23] investigated the influence of a Gaussian or Lorentzian velocity distribution on the contrast level. Under the assumption of a Lorentzian [23, 24] velocity distribution, the relation between the correlation time τ_c , the exposure time T and the contrast is given by:

$$\frac{\sigma}{\langle I \rangle} = \sqrt{\frac{\tau_c}{2T} \left(1 - \exp\left(-\frac{2T}{\tau_c}\right) \right)} \quad (2.3)$$

2 Review of laser speckle contrast techniques for visualizing tissue perfusion

So a small value of the contrast corresponds with a small τ_c (i.e. fast moving speckles) and a contrast close to unity corresponds to a large τ_c (i.e. stationary speckle pattern). For a Gaussian velocity distribution [19, 23, 25], the relation is given by:

$$\frac{\sigma}{\langle I \rangle} = \sqrt{\frac{\sqrt{\pi} \tau_c}{2 T} \operatorname{erf} \left(\frac{T}{\tau_c} \right)} \quad (2.4)$$

The integral over time of the normalized autocorrelation function of a velocity distribution should equal the correlation time τ_c . However, for equation 2.4 this is not the case, so Ramirez-San-Juan *et al.* [25] proposed to use an alternate expression for the Gaussian velocity distribution :

$$\frac{\sigma}{\langle I \rangle} = \sqrt{\frac{1}{2} \frac{\tau_c}{T} \operatorname{erf} \left(\frac{\sqrt{\pi} T}{\tau_c} \right)} \quad (2.5)$$

In figure 2.2, C is plotted as a function of T/τ_c under the assumption of a Lorentzian and the two Gaussian velocity distributions. There is a clear difference visible between the contrast values based on a Lorentzian or Gaussian velocity distribution for a given T/τ_c . For high contrast levels, correlation times may vary upto one order of magnitude. However, for the alternate Gaussian velocity distribution, there is a good agreement between the Lorentzian and Gaussian velocity distribution for C -values below 0.5. Ramirez-San-Juan *et al.* [23] showed furthermore that for the flow rates used in their experiments, the Gaussian based approach is superior to the normally used Lorentzian approach in speckle contrast techniques. The relation between τ_c and v_c (e.g. equation 2.2) is essential to link the measured contrast values via speckle decorrelation time to the decorrelation velocity.

Recently Duncan *et al.* [26] stated that the Lorentzian velocity distribution model is only applicable for Brownian motion whereas an inhomogeneous (Gaussian) distribution is valid for ordered motion. They claimed that the proper model for the combined effect (i.e Brownian motion and ordered motion) is a Voigt velocity distribution, which is the result of a convolution of a Lorentzian and Gaussian velocity distribution.

Table 2.1: Methods of measuring tissue blood flow with laser speckle contrast techniques.

Technique	Abbrev.	Domain	Principle
Laser Speckle Contrast Analysis [19, 27]	LASCA	spatial	Contrast is determined in 1 image over 5×5 or 7×7 pixels.
Laser Speckle Imaging [28]	LSI	temporal	Contrast is determined in 1 pixel over 25 or 49 images.
Double exposure speckle photography [29, 30]	DESP	spatial	A sequence of two rapid speckle recordings is taken in 1 images. The resulting fringes contain information about the movement.
Single exposure speckle photography [19, 24]	SESP	spatial	Forerunner of LASCA, based on the same principle.
Laser Speckle Temporal Contrast Analysis [31]	LSTCA	temporal	Contrast is determined in 1 pixel over a sequence of images.
Laser Speckle Perfusion Imaging [32, 33]	LSPI	spatial & temporal	Combination of LASCA and LSI.
Laser Speckle Flowgraphy [34]	LSFG	spatial & temporal	The contrast is determined based on an area of 3×3 pixels, in 3 speckle images.
Spatial Derived Contrast with Averaging [35]	SDCav	spatial	Contrast is determined based on averaging a sequence of LASCA-images.
Temporal Laser Speckle Contrast Analysis [36]	tLASCA	spatial & temporal	Contrast is determined based on averaging a sequence of LSI-images.
Spatial Laser Speckle Contrast Analysis [36]	sLASCA	spatial	Contrast is determined based on averaging a sequence of LASCA-images.
Multi-Exposure Speckle Imaging [37]	MESI	spatial	Contrast is determined in 1 image over 7×7 pixels. Exposure time is kept constant and T is controlled by laser pulse duration.

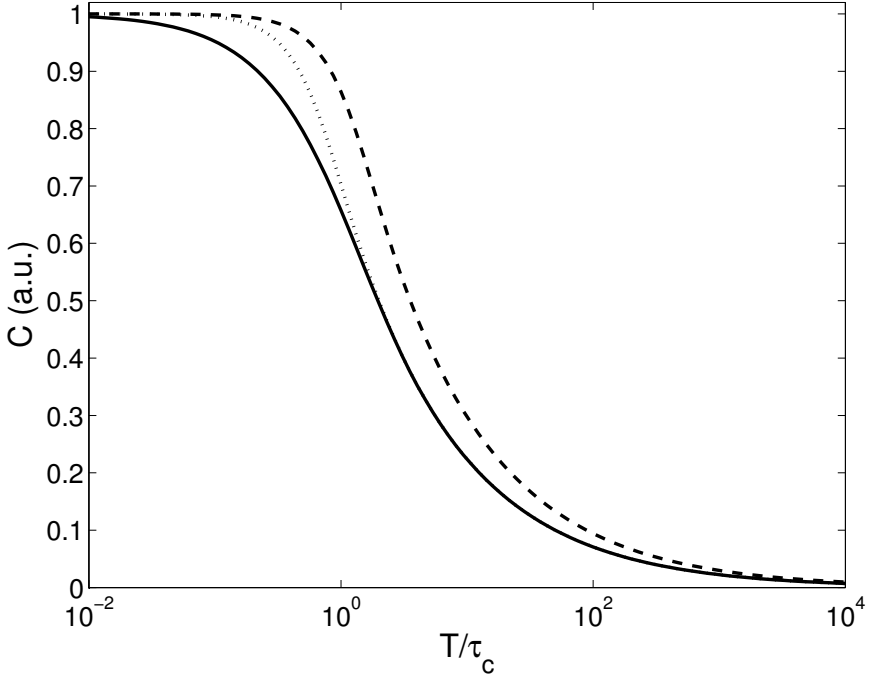


Figure 2.2: C as a function of T/τ_c for a Lorentzian velocity distribution (solid), Gaussian velocity distribution (dashed) and alternate Gaussian velocity distribution (dotted).

2.4 Speckle contrast flow measurement techniques

Several researchers used the principle of speckle contrast to develop techniques for measuring skin perfusion. In this paper several of these techniques will be discussed. Table 2.1 summarizes the various techniques.

2.4.1 Double and single exposure speckle photography

Archbold and Ennos [38] invented double-exposure speckle photography [29, 39], a technique which was the forerunner of LASCA (see section 2.4.2). Strictly speaking, double speckle photography is no speckle contrast tech-

nique since each of the two exposures is a snapshot rather than a blurred image. Double-exposure speckle photography is based on the principle that a photographic record of two identical and mutually displaced speckle structures gives rise to parallel straight fringes in the Fourier plane. The spacing and orientation of these fringes is related to the displacement and direction between both photographs. This makes the technique only applicable for solid bodies or fluids with a stationary flow pattern [38]. Iwai and Shigeta [30] developed a digital version of double-exposure speckle photography. To obtain a velocity map, the whole image should be divided into small regions for analysis over which the velocity can be assumed to be spatially constant. The analysis of these fringe-patterns is complicated compared to analysis performed in speckle contrast techniques, which is a disadvantage.

The first real speckle contrast technique, using a long exposure time, was single speckle photography [40]. Single exposure speckle photography [24] was a laborious process (i.e. making and developing a photograph and analysis of the negative film).

2.4.2 Laser speckle contrast analysis (LASCA)

Briers and Webster [19, 41, 42] developed a digital version of single speckle photography using a monochrome CCD and frame grabber linked to a computer. The digital photograph is processed by the computer and the local contrast is computed in a block of $n \times n$ pixels. This digital version was the first setup which uses *laser speckle contrast analysis* (LASCA) as we know it nowadays. Figure 2.3(a) shows a schematic overview of a LASCA-setup with an expanded laser beam, an imaging system comprising focussing optics, a variable diafragma and a digital camera as essential features. Figure 2.3(b) shows a schematic overview of the way the contrast is calculated in LASCA. The contrast is calculated by :

$$C_{i,j} = \frac{\sqrt{\frac{1}{(n+1)^2} \sum_{x=i-\frac{n}{2}}^{i+\frac{n}{2}} \sum_{y=j-\frac{n}{2}}^{j+\frac{n}{2}} I_{x,y}^2 - \left(\frac{1}{(n+1)^2} \sum_{x'=i-\frac{n}{2}}^{i+\frac{n}{2}} \sum_{y'=j-\frac{n}{2}}^{j+\frac{n}{2}} I_{x',y'} \right)^2}}{\frac{1}{(n+1)^2} \sum_{x=i-\frac{n}{2}}^{i+\frac{n}{2}} \sum_{y=j-\frac{n}{2}}^{j+\frac{n}{2}} I_{x,y}} \quad (2.6)$$

with $I_{i,j}$ the intensity of pixel i,j and $n+1$ the size of the square over which the contrast is calculated. Experiments showed [43, 44] that in LASCA it

2 Review of laser speckle contrast techniques for visualizing tissue perfusion

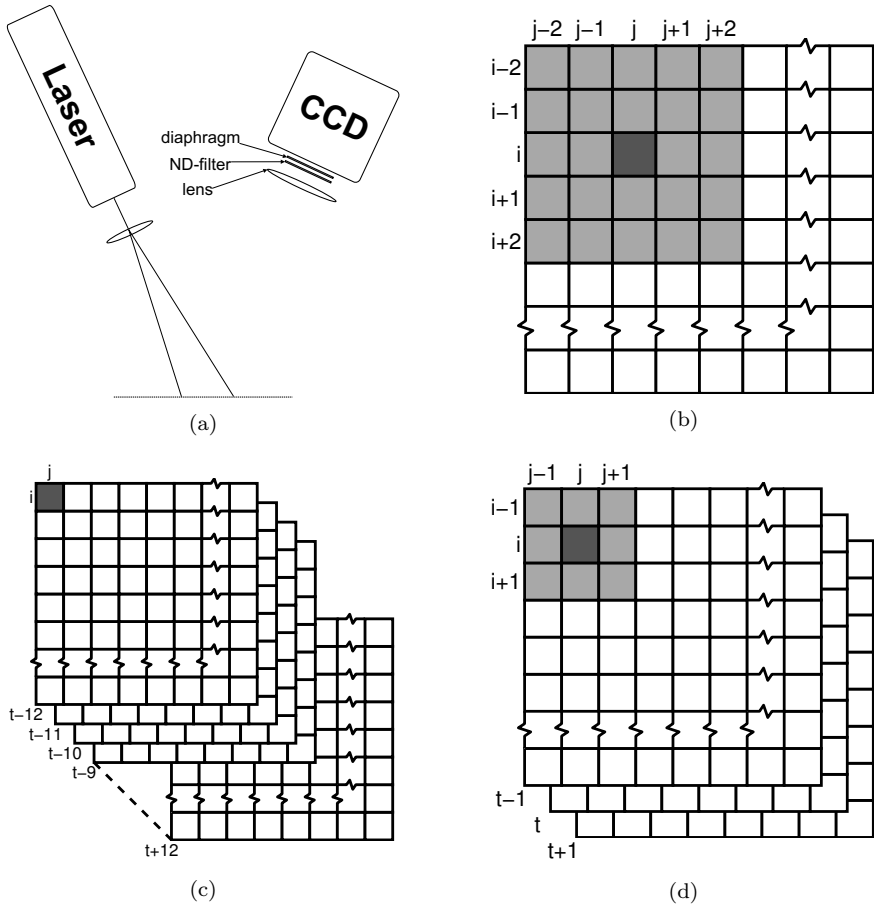


Figure 2.3: (a) LASCA-setup with essential features, (b) schematic overview of the way the contrast is calculated in LASCA. With the squares being pixels of a recorded image, the contrast in pixel (i,j) (dark grey) is determined by calculating the ratio of the standard deviation of the pixels in the pale grey $n \times n$ pixel area to the mean value of the pixels in this area, (c) schematic overview of the way the contrast is calculated in LSI. In pixel (i,j) the contrast is calculated as the ratio of the standard deviation of the intensity at this pixel at different times, and the mean intensity for this pixel and (d) schematic overview of the way the contrast is calculated in LSFSG. The mean blur rate (MBR) is determined by calculating the ratio of the mean value of the pixels in the pale gray area to mean difference of the central point (dark gray) and the pixels in the pale gray area.

was not possible to obtain the full contrast range from 0 to 1.0. Richards and Briers [44, 45] suggested this was due to an offset in the pixel values termed *pedestal* and introduced by the CCD camera. Manually removing this offset resulted in an increase in contrast from 0.41 to 0.95 for a static speckle pattern. The next major improvement to the LASCA-setup was in the image processing. Changing from software written in C++ operating under DOS to Windows in combination with improved code and a 166MHz Pentium processor, reduced the processing time for a full frame from approximately four minutes down to approximately 1 second [44, 46]. Besides improving the computer hardware and software, the development of the LASCA technique continued. An improved version was described by Richards and Briers who implemented a camera with a variable exposure time and ran trials with lasers in the green wavelength range instead of in the red [21, 44, 45]. Several researchers used a slightly different LASCA-setup. For example, in one setup, the backscattered light was collected on the camera without making use of a lens but by making use of a single-mode fiber [47] or adjustable iris and camera in the diffraction plane [48]. Furthermore a polarizer was positioned in between sample and camera to select the linearly polarized light [49] to increase the contrast of the grabbed speckle pattern [21, 44, 45, 47].

LASCA is fast and inexpensive, but there are technical details which should be taken into account for proper measurements. To adjust the “sensitivity” of the LASCA-setup to a certain velocity, the integration time can be adjusted. As the integration time changes, the noise in the measurement also changes. Yuan *et al.* [50] identified a relation linking sensitivity, noise and camera exposure time. They found that with an increasing exposure time up to 2 ms, the sensitivity to relative speckle changes increased. However, the noise in the speckle contrast also increases with increasing exposure time. The optimal contrast-to-noise ratio was found to be at 5 ms, so Yuan *et al.* suggested that ~ 5 ms is an optimal exposure time for LASCA-measurements in the brains of rodents.

To obtain good statistics, the speckle size should be carefully controlled. When speckle size and pixel size are of the same order, the error in calculated contrast is minimized [44, 50]. For image speckle (i.e. image the speckle pattern with a lens in front of for example a camera), the speckle size is dependent on the laser wavelength (λ), the f-number of the lens system ($f_{\#}$) and the magnification (M), as expressed by:

$$d = 2.44\lambda f_{\#}M \tag{2.7}$$

So by controlling the f-number of the lens system (i.e. adjusting the iris of the lens system) the optimal speckle size can be chosen. However, this removes the facility to control the amount of light falling on the camera because Yuan *et al.* [50] showed that a fixed integration time of ~ 5 ms gives the best contrast-to-noise ratio. So neutral density filters should be used to adjust the amount of light falling on the camera [44].

With “classical” LASCA, all depth-information about perfusion is lost, so Zimnyakov and Misnin [48] modified the setup by making use of a localized moving light source in combination with spatial filtering to reveal depth-resolved information about the micro circulation. When a dynamic layer below a static layer is imaged, the resulting speckle pattern will be composed of a stationary speckle pattern in the inner zone of the CCD camera and a dynamic speckle pattern in the outer zone. So by placing filtering diaphragms on the sample, depth information can be obtained. As a consequence of the stationary speckle pattern, the contrast will not drop to 0 for long integration times. To quantify that Zimnyakov and Misnin introduced the term *residual contrast*.

2.4.3 Laser speckle imaging (LSI)

Due to the fact that the contrast is analyzed for a group of pixels in one image, LASCA has the disadvantage of a lack of spatial resolution. So Cheng *et al.* [28] developed *laser speckle imaging* (LSI) to compensate for this disadvantage. LSI is the temporal equivalent of LASCA; the contrast is calculated based on one pixel in a time sequence, rather than based on multiple pixels in one image, as is schematically shown in figure 2.3(c). In LSI, the contrast is calculated by:

$$C_{i,j} = \frac{\sigma}{\langle I \rangle} = \frac{\sqrt{\frac{1}{n+1} \sum_{l=t-n/2}^{t+n/2} I_{i,j,l}^2 - \left(\frac{1}{n+1} \sum_{l'=t-n/2}^{t+n/2} I_{i,j,l'} \right)^2}}{\frac{1}{n+1} \sum_{l=t-n/2}^{t+n/2} I_{i,j,l}} \quad (2.8)$$

where $I_{x,y,t}$ is the intensity of pixel (i, j) at time t and $n + 1$ the number of speckle images over which the contrast is calculated. Note that no flow (i.e. no dynamic speckle pattern) and very high flow (i.e. complete blurred dynamic speckle pattern) both give a contrast equal to 0. This makes LSI

unsuitable for sample with regions where no flow is present. Cheng *et al.* [28] showed that calculating the contrast with LSI gives as expected a five times higher spatial resolution compared to LASCA. They only assumed a linear relationship between the measured flow rate (i.e. $1/\tau_c$) and actual flow rate values, whereas Choi *et al.* [51] showed that there is a linear relationship between these parameters, the range over which this is valid depends on the integration time of the camera (e.g. 0 to 20 mm/s for $T = 1$ ms and 0 to 5 mm/s for $T = 10$ ms), as already was suggested by Yuan *et al.* [50].

Nothdurft and Yao [52] showed that by adjusting the capture parameters (e.g. exposure time, incident power and time interval between subsequent capture), LSI is able to reveal structures which are hidden under the surface. Surface and subsurface inhomogeneities depend differently on these capture parameters, so by tuning the capture parameters, the image contrast values of the surface and subsurface targets can be changed. When the contrast of the surface inhomogeneity is within the noise level of the background image, the surface effect is essentially removed from the image. They did not test LSI on tissue perfusion; that was done by Li *et al.* [31] who named the technique differently, *laser speckle temporal contrast analysis* (LSTCA), but it is based on the same principle as LSI. They presented images of the cerebral blood flow of a rat through the intact skull by making use of temporal averaging of the speckle pattern. They used an exposure time of 5 ms, which is of the same order as that suggested by Yuan *et al.* [50] and an interval time of 25 ms, resulting in a real-time video frame-rate of 33 Hz. They furthermore showed that LSTCA significantly improves the visualization of the blood vessels with respect to LASCA due to the fact that the speckle pattern on the detector is built up of a stationary and a dynamic part. They stated that the stationary part produced by the skull is mainly dependent on local properties of the skull and is therefore temporally homogeneous. So the contrast value in the LSTCA-process is not influenced by the stationary part whereas in the LASCA-process the stationary part will influence the contrast value and lower the SNR.

Völker *et al.* [53] modified LSI by positioning a rotating diffuser, which can be controlled by a motor, to illuminate the sample with a random speckle pattern. In this way, they could suppress the noise in LSI. If the diffuser rotates slowly (e.g. one rotation per hour), temporal fluctuations will occur at time scale τ_0 . However, if the exposure time T of the camera is chosen to be smaller than τ_0 , subsequent speckle images will be statistically independent and analyzing a large number of images results in the perfect averaging of the

contrast without loss of spatial resolution. They showed that the noise level scales with $N^{-0.5}$, with N being the number of independent speckle-images.

Bandyopadhyay *et al.* [54] and Zakharov *et al.* [55] pointed out recently that the commonly used LSI equation (i.e. equation 2.3) involves an approximation (i.e. $\tau_c \ll T$ for Lorentzian velocity distribution) that could result in incorrect data analysis. Cheng and Duong [56] investigated the contribution of such approximation and its impact on LSI data analysis. They showed that the approximation is valid for calculating blood flow changes rather than absolute values for $\tau_c \ll T$.

Furthermore they introduced a time-efficient LSI analysis method by making use of the asymptotic approximation of the commonly used LSI equation (i.e. equation 2.3) instead of using the Newtonian iterative method to solve that equation. Based on these findings, Parthasarathy *et al.* [37] presented a new multi-exposure speckle imaging (MESI) instrument based on their *robust speckle model* that has potential to obtain quantitative baseline flow measures and overcomes their criticism of LASCA and LSI (e.g. lack of quantitative accuracy and the inability to predict flows in the presence of static scatterers such as an intact or thinned skull). To keep the noise contribution of the camera (e.g. readout noise, thermal noise) constant while changing the integration time, they used a fixed exposure time for the camera and gated a laser diode during each exposure to effectively vary the speckle exposure duration T .

2.4.4 Other techniques

LASCA has the disadvantage of a lack of spatial resolution whereas LSI has the disadvantage of a lack of temporal resolution. Therefore, several researchers [32–36] have developed techniques which are combinations of LASCA and LSI. Forrester *et al.* [32, 33] developed *laser speckle perfusion imaging* (LSPI), Tan *et al.* [35] developed *LASCA using spatially derived contrast with averaging* (SDCav), Konishi *et al.* [34] developed *Laser speckle flowgraphy* (LSFG) and Le *et al.* [36] introduced *tLASCA* and *sLASCA* as temporal and spatial equivalents of LASCA.

In LSPI, the mean value of the speckle-intensity, which is called speckle reduction by Forrester *et al.* [32, 33], can be determined by spatial averaging (good temporal resolution), temporal averaging (good spatial resolution) or

a combination of both (acceptable temporal and spatial resolutions). The nonfluctuating component of the measured intensity is quantified by the speckle reduction:

$$I_{REF}(i, j) = \frac{1}{N_{MAX}} \sum_{N=1}^{N_{MAX}} \left[\frac{1}{2m+1} \sum_{i-m}^{i+m} \left(\frac{1}{2n+1} \sum_{j-n}^{j+n} I_{SP,N}(i, j) \right) \right] \quad (2.9)$$

where $I_{SP,N}$ is the intensity of pixel (i, j) in the N^{th} frame in a sequence of N_{MAX} frames and m and n the boundaries for the chosen region around pixel (i, j) . To quantify the fluctuating component, the sum of the difference between the speckle reduction and the speckle-intensity is taken and normalized with the speckle reduction:

$$I_{SD,norm}(i, j) = \frac{\sum_{N=1}^{N_{MAX}} \left[\sum_{i-m}^{i+m} \left(\sum_{j-n}^{j+n} |I_{SP,N}(i, j) - I_{REF}(i, j)| \right) \right]}{I_{REF}(i, j)} \quad (2.10)$$

which is different from the formal definition of contrast as given in equation 2.1, where the numerator is based on the standard deviation of the fluctuation instead of the mean absolute difference of the fluctuations.

To determine the perfusion, the inverse relation of the normalized sum is taken. For obtaining high spatial resolution images, Forrester *et al.* [33] used a frame rate of just over 6 Hz, while with spatial averaging they obtained a semi-real time imaging speed with a frequency of 15 Hz. The method of calculating the flow in LSF, or mean blur rate (MBR) as Konishi *et al.* [34] termed it, is comparable to the combination of spatial and temporal averaging introduced by Forrester *et al.* [33]. In LSF a $3 \times 3 \times 3$ pixel matrix is taken and the MBR is defined as the mean intensity across these 26 pixels (the central point is not taken into account) divided by the mean difference of the central point and the 26 pixels. This is schematically shown in figure 2.3(d). When using a CCD-camera in LSF, the interlace scanning mode of the camera requires compensation for the fact the odd lines are captured at different time to the even lines, so Konishi *et al.* [34] adjusted the definition of the MBR in LSF to:

$$MBR_{n,m,t} = \frac{2 \langle I_{n,m,t} \rangle^2}{\langle I_{n,m,t}^2 \rangle - \langle I_{n,m,t} \rangle^2} \quad (2.11)$$

where the factor 2 in the numerator is related to the number of uncorrelated intensity data taken for the averaging (i.e. even and odd lines).

Tan *et al.* [35] modified the “classical” LASCA to SDCav by introducing averaging over multiple contrast maps, resulting in a decrease in Root Mean Square (RMS) of the value of $1/\tau_c$ with an increasing number of averages. A few years later, this technique of averaging over multiple contrast maps was presented by Le *et al.* [36] under the name sLASCA. They also introduced tLASCA, a technique in which averaging in the spatial domain is performed on contrast maps obtained using LSI. They showed that tLASCA give better results and is faster than sLASCA and LSI.

All techniques discussed here have advantages and disadvantages. Imaging blood flow using LASCA gives a higher temporal resolution compared to LSI and LSFSG, so for fast changing perfusion levels it is the best candidate. LSI on the other hand provides the best spatial resolution which makes it suitable for producing detailed perfusion images. LSFSG is a combination between these two techniques which makes it ideal for situations where a trade-off between temporal and spatial resolution is needed.

Usually a speckle pattern is build up from a dynamic and a static part. As is shown by Yuan *et al.* [50] the static part does not influence the contrast in LSI, which results in a higher SNR for LSI compared to LASCA and LSFSG.

2.5 Applications

The laser speckle contrast techniques discussed above can be used in a wide variety of biomedical applications, and several researchers have presented *in-vivo* results. DaCosta [57] used it to monitor the heartbeat of a human volunteer in a non-invasive way. Sadhwani *et al.* [58] showed that the thickness of a Teflon layer could be determined by using laser speckle contrast techniques, so both, they and Zimnyakov and Misnin [48], suggested that laser speckle contrast techniques could be used for burn depth diagnosis.

Richards and Briers [45] showed that contrast images obtained using LASCA give a good picture of the movement of red blood cells in the hand of a volunteer. Cheng and Duong [56] and Konishi *et al.* [34] even used LSI and LSFSG respectively to map the ocular blood flow in the retina.

Ramirez-San-Juan *et al.* [23] used chicken chorioallantoic membrane (CAM) to prove that the use of the Gaussian-based approach reveals more details such as small vessels than the Lorentzian based approach.

Several researchers reported contrast images of perfusion in rodents [5, 28, 31, 35, 36, 50, 59–64]. Yuan *et al.* [50] used changes in contrast images of the rat brain after electrical stimulation to obtain the optimal exposure time. Kubota [59] used LSCG to investigate the effects of Diode Laser Therapy on blood flow in skin flaps in the Rat Model. To assess changes in blood flow during photo dynamic therapy (PDT), Kruijt *et al.* [62] used LSPI to monitor the vasculature response in arteries, veins and tumour microvasculature in a rat skin-fold observation chamber. Smith *et al.* [63] used contrast images to image the microvascular blood flow using an in vivo rodent dorsal skinfold model during PDT, pulsed dye laser (PDL) irradiation and a combination of both on port wine stains. Dunn *et al.* [5] used LASCA to map the cerebral flow of a rat and simultaneously measure the perfusion using a laser Doppler probe. They showed there is a good agreement between the flow *in-vivo* measured with both techniques. Several researchers like Cheng *et al.* [28], Tan *et al.* [35], Li *et al.* [31], Murari *et al.* [65] and Le *et al.* [36], did similar work to image the cerebral flow but used temporal averaging. Zhu *et al.* [64] monitored thermal-induced changes in tumor blood flow and microvessels in mice by using LASCA, and showed that deformation of vessel is a main factor for changing the blood perfusion of a microvessel.

Besides visualizing blood flow, LASCA can also be used to characterize the composition of atherosclerotic plaques, as achieved by Nadkarni *et al.* [66, 67]. They measured the speckle decorrelation time τ_c which provides an index of plaque viscoelasticity and helps characterize the composition of the plaque, which can be used to identify high-risk lesions. They showed that LASCA is highly sensitive to changes in the plaque composition so it can be used to identify thin-cap fibroatheromas.

2.6 Comparison with laser Doppler perfusion imaging

Nowadays there are two major techniques which are used to image the tissue perfusion. Besides laser speckle contrast techniques, laser Doppler perfusion imaging (LDPI) is used to image the perfusion. In LDPI, optical Doppler shifts are analysed from the temporal intensity fluctuations which are caused by the dynamic speckle pattern. A number of locally measured power spectra of these intensity fluctuations is converted into a perfusion image.

Till recently LASCA had the advantage over LDPI of being a full-field tech-

2 Review of laser speckle contrast techniques for visualizing tissue perfusion

nique, whereas LDPI was a scanning technique. This scanning mode resulted in long measurement times, which made LDPI less favorable for the clinical environment. This advantage decreased when LDPI became a full-field technique by introducing a high-speed CMOS-camera for the detection of the Doppler-shifted light [68–71]. From that moment on, both techniques had a measurement time in the millisecond range.

The introduction of the high-speed CMOS-cameras in LDPI directly reveals another advantage of LASCA over LDPI. To perform LASCA measurements an inexpensive camera which can achieve a frame-rate of 200 Hz (i.e. an integration time of 5 ms) is sufficient, whereas for LDPI, a state-of-the-art high-speed camera which can achieve a frame-rate of about 25 kHz is needed.

On the other hand, the physics behind LDPI is well-known and it is shown that, for low blood concentrations, the concentration of red blood cells and their average velocity are both linearly represented by the perfusion estimation given in LDPI. Bonner and Nossal [22] published a widely accepted theoretical model of laser Doppler measurements to determine these parameters of blood flow in tissue.

For LASCA and related speckle contrast techniques, a model linking the measurement outcome to the perfusion, is not available. The reading of LASCA is based on blurring of the speckles on the detector. To link this blurring with the average velocity of red blood cells, assumptions should be made about an appropriate velocity distribution (e.g. Lorentzian, Gaussian, Voigt) the fraction of moving red blood cells and other parameters (e.g. particle size). With the wide variety of biological applications, this is a major challenge. So yet there is no proper model linking the speckle contrast to the perfusion. To our knowledge, determination of the concentration of red blood cells with LASCA has not been shown to be possible.

Another difference between laser speckle contrast techniques and LDPI is the opportunity to apply high-pass filtering (e.g. above 100 Hz) to the recorded signals in LDPI to filter out movement artifacts. For laser speckle contrast techniques filtering out those artifacts is not possible, which is a major disadvantage. Another disadvantage of laser speckle contrast techniques is shown in figure 2.4. The exposure time is a parameter which can be chosen freely, however the choice of the integration time influences the calculated contrast values drastically. Both contrast images in figure 2.4 show the same area of growing blood vessels of a chicken embryo and its chorio-allantoic membrane. The black arrows in the images indicate the heart and the major

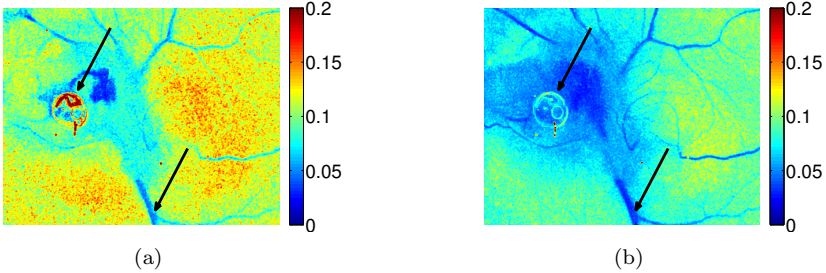


Figure 2.4: LASCA contrast maps of the heart of a chicken embryo. (a) taken with an integration time of 15 ms and (b) taken with an integration time of 40 ms. The black arrows indicate the heart and the major feeding vessel.

feeding vessel. With a short integration time (i.e. 15 ms, figure 2.4(a)) the contrast image shows mainly fast moving blood cells (i.e. blood vessels round the heart) whereas with a long integration time (i.e. 40 ms, figure 2.4(b)) the contrast image highlights slower moving blood cells (i.e. blood vessels further away from the heart). So the choice of the integration time determines what can be seen in the image.

To illustrate how images look like produced by several contrast techniques discussed here, figure 2.5 shows the same sample imaged with LASCA, LSI, LSFG and compared with LDPI. With capsicum cream (Midalgan, Remark Groep BV, Meppel, the Netherlands), a perfusion increasing cream, a pattern was written on the right hand of a volunteer (male, 28 yr). The tissue was imaged twice, once with a frame rate of 125 Hz (an integration time of 8 ms) for LASCA, LSI and LSFG and once with a frame rate of 27 kHz (an integration time of $37 \mu\text{s}$) for LDPI. In each measurement the f-number was chosen to avoid saturation. The data obtained at a low frame rate were processed with LASCA (5×5 pixels), LSI (25 images) and LSFG, the resulting images are shown in figure 2.5(a)-(c) respectively. The second measurement was processed with LDPI (i.e. first moment of the power spectrum from 0 till 13.5 kHz) and normalized with DC, the resulting image is shown in figure 2.5(d). In comparison with LDPI, LSI and LSFG give a good indication of areas with high and low perfusion. The lack of spatial resolution of LASCA compared to the other techniques is also clearly illustrated.

Forrester *et al.* [32] compared LDPI with some of the laser speckle contrast

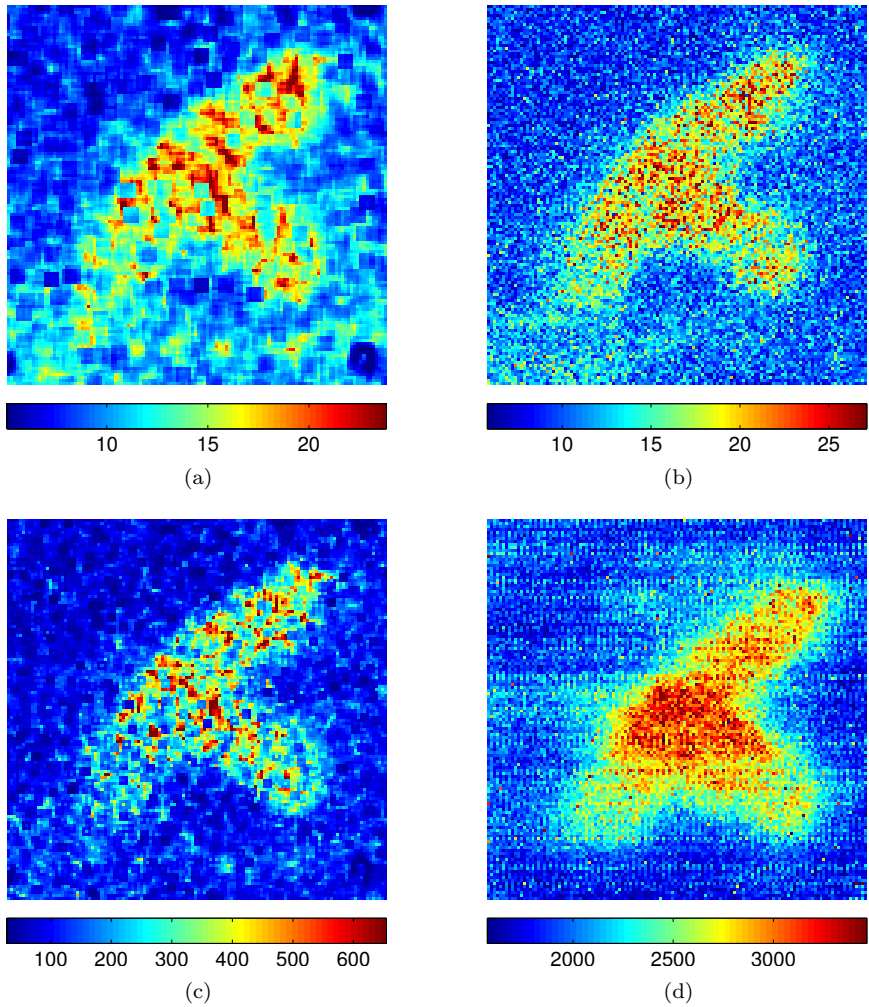


Figure 2.5: Comparison of 3 speckle contrast techniques discussed here with laser Doppler perfusion imaging. On the right hand of a volunteer a pattern was written with capsaicin cream, a perfusion increasing cream, and imaged with the different techniques. (a) The inverse of the contrast determined with LSI, (b) the inverse of the contrast determined with LSI, (c) MBR determined with LSF and (d) the perfusion determined with LDPI. The contrast, MBR and perfusion values are shown in the colorbar.

techniques discussed in this paper. They imaged digits of a human hand and the joint capsule and muscle in a rabbit knee, and suggested that laser speckle contrast techniques are a good and fast alternative for LDPI and therefore should be further developed. Furthermore, the higher temporal resolution of LASCA made it more sensitive to the hyperaemic response after an occlusion. Besides Forrester *et al.*, several other researchers have performed a comparison between both techniques [27, 71–73]. Briers [27] compared both technique from a more theoretical point of view and postulated the essential equivalence of both techniques. He therefore encouraged some cross fertilization of ideas between both techniques. Serov and Lasser [71] compared LASCA and LDI in their hybrid imaging system. They not only compared imaging quality and speed, but also sensitivity for flow parameters such as speed and concentration. In their measurements LASCA turned out be faster (i.e 10 frames per second) but had a poorer spatial resolution. Thompson and Andrews [73] postulated a method to gain the quantitative advantages of LDPI while keeping the speed of LASCA. They claim that by making use of a temporal autocorrelation function of the LASCA measurement, a perfusion index comparable to the index of LDPI can be obtained.

2.7 Conclusions

Speckle contrast techniques are gaining interest in the field of tissue perfusion imaging. In this paper, we have presented the principles and various implementations of the speckle contrast methods, reviewed the contribution of these techniques to the field of perfusion imaging and described their technical development.

Speckle contrast techniques have advantages over their main counterpart, laser Doppler perfusion imaging (LDPI). Speckle contrast techniques need only one or a few frames to determine the tissue perfusion, which makes it fast. They also need a low frame rate camera only, which makes them inexpensive techniques. But they also have one major disadvantage with respect to LDPI; the readings in LDPI can be related to the Doppler effect which is described by a theory which is widely accepted and understood. For LASCA this is not the case, since, for example, it is still unknown which velocity distribution (e.g. Voigt, Lorentzian or Gaussian) should be used. The need to assume a specific velocity distribution to relate the speckle

contrast to the tissue perfusion makes the technique less generally applicable.

Once there is consensus about a theoretical model for LASCA which connects the contrast unambiguously to the perfusion level, it can become one of the leading techniques for measuring tissue perfusion maps.

References

1. H. Fuji, T. Asakura, K. Nohira, Y. Shintomi & T. Ohura (1985). “Blood flow observed by time-varying laser speckle”. *Optics Letters*, **10**(3), 104–106.
2. B. Ruth (1990). “Blood flow determination by the laser speckle method”. *International Journal of Microcirculation: Clinical Experiments*, **9**, 21–45.
3. S. S. Ulyanov (1998). “Speckled speckle statistics with a small number of scatterers: Implication for blood flow measurement”. *Journal of Biomedical Optics*, **3**(3), 237–245.
4. S. S. Ulyanov & V. V. Tuchin (2000). “Use of low-coherence speckled speckles for bioflow measurements”. *Applied Optics*, **39**(34), 6385–6389.
5. A. K. Dunn, H. Bolay, M. A. Moskowitz & D. A. Boas (2001). “Dynamic imaging of cerebral blood flow using laser speckle”. *Journal of Cerebral Blood Flow and Metabolism*, **21**(3), 195–201.
6. R. Bray, K. Forrester, C. Leonard, R. McArthur, J. Tulip & R. Lindsay (2003). “Laser Doppler imaging of burn scars: A comparison of wavelength and scanning methods”. *Burns*, **29**(3), 199–206.
7. C. J. Stewart, R. Frank, K. R. Forrester, J. Tulip, R. Lindsay & R. C. Bray (2005). “A comparison of two laser-based methods for determination of burn scar perfusion: Laser Doppler versus laser speckle imaging”. *Burns*, **31**, 744–752.
8. E. La Hei, A. Holland & H. Martin (2006). “Laser Doppler imaging of paediatric burns: Burn wound outcome can be predicted independent of clinical examination”. *Burns*, **32**, 550–553.

9. F. F. M. de Mul, J. Blaauw, J. G. Aarnoudse, A. J. Smit & G. Rakhorst (2007). “Diffusion model for iontophoresis measured by laser-Doppler perfusion flowmetry, applied to normal and preeclamptic pregnancies”. *Journal of Biomedical Optics*, **12**(1), 14032–1.
10. M. J. Leahy, J. G. Enfield, N. T. Clancy, J. O’Doherty, P. McNamara & G. E. Nilsson (2007). “Biophotonic methods in microcirculation imaging”. *Medical Laser Application*, **22**, 105–126.
11. K. Wårdell, A. Jakobsson & G. E. Nilsson (1993). “Laser Doppler perfusion imaging by dynamic light scattering”. *IEEE Transactions on biomedical Engineering*, **40**(4), 309–316.
12. S. Webster & J. D. Briers (1994). “Time-integrated speckle for the examination of movement in biological systems”. In L. J. Cerullo, K. S. Heiferman, H. Liu, H. Podbielska, A. O. Wist & L. J. Zamorano (eds.) *Clinical Applications of Modern Imaging Technology II, Proc. SPIE*, vol. 2132, pp. 444–452.
13. H. Zhao, R. H. Webb & B. Ortel (2002). “Review of noninvasive methods for skin blood flow imaging in microcirculation”. *Journal of Clinical Engineering*, **27**(1), 40–47.
14. Y. Aizu & T. Asakura (1991). “Bio-speckle phenomena and their application to the evaluation of blood flow”. *Optics & Laser Technology*, **23**(4), 205–219.
15. J. D. Briers (2001). “Laser Doppler, speckle and related techniques for blood perfusion mapping and imaging”. *Physiological Measurements*, **22**, R35–R66.
16. J. D. Briers (2007). “Laser speckle contrast imaging for measuring blood flow”. *Optica Applicata*, **XXXVII**, 139–152.
17. D. D. Duncan, S. J. Kirkpatrick & R. K. Wang (2008). “Statistics of local speckle contrast”. *Journal of the Optical Society of America A: Optics and Image Science, and Vision*, **25**(1), 9–15.
18. J. W. Goodman & G. Parry (1975). *Laser Speckle and Related Phenomena*. Springer-Verlag, New York.
19. J. D. Briers & S. Webster (1995). “Quasi real-time digital version of single-exposure speckle photography for full-field monitoring of velocity or flow fields”. *Optics Communications*, **116**, 36–42.

2 Review of laser speckle contrast techniques for visualizing tissue perfusion

20. J. D. Briers & G. J. Richards (1997). “Laser speckle contrast analysis (LASCA) for flow measurement”. In C. Gorecki (ed.) *Optical Inspection and Micromeasurements II, Proc. SPIE*, vol. 3098, pp. 211–221.
21. G. J. Richards & J. D. Briers (1997). “Laser speckle contrast analysis (LASCA): A technique for measuring capillary blood flow using the first order statistics of laser speckle patterns”. In *IEE Colloquium (Digest)*, 124, pp. 11–1. London, UK.
22. R. Bonner & R. Nossal (1981). “Model for laser Doppler measurements of blood flow in tissue”. *Applied Optics*, **20**(12), 2097–2107.
23. J. C. Ramirez-San-Juan, J. S. Nelson & B. Choi (2006). “Comparison of lorentzian and gaussian based approaches for laser speckle imaging of blood flow dynamics”. In V. V. Tuchin, J. A. Izatt & J. G. Fujimoto (eds.) *Coherence Domain Optical Methods and Optical Coherence Tomography in Biomedicine X, Proc. SPIE*, vol. 6079, pp. 380–383.
24. A. F. Fercher & J. D. Briers (1981). “Flow visualization by means of single-exposure speckle photography”. *Optics Communications*, **37**(5), 326–330.
25. J. C. Ramirez-San-Juan, R. Ramos-Garcia, I. Guizar-Iturbide, G. Martinez-Niconoff & B. Choi (2008). “Impact of velocity distribution assumption on simplified laser speckle imaging equation”. *Optics Express*, **16**(5), 3197–3203.
26. D. D. Duncan, S. J. Kirkpatrick & J. C. Gladish (2008). “What is the proper statistical model for laser speckle flowmetry?” In V. V. Tuchin & L. V. Wang (eds.) *Complex Dynamics and Fluctuations in Biomedical Photonics V, Proc. SPIE*, vol. 6855, pp. 685502–685502–7.
27. J. D. Briers (1996). “Laser Doppler and time-varying speckle: A reconciliation”. *Journal of The Optical Society of America, A*, **13**(2), 345–350.
28. H. Cheng, Q. Luo, S. Zeng, S. Chen, J. Cen & H. Gong (2003). “Modified laser speckle imaging method with improved spatial resolution.” *Journal of Biomedical Optics*, **8**(3), 559–564.
29. R. Grousson & S. Mallick (1977). “Study of flow pattern in a fluid by scattered laser light”. *Applied Optics*, **16**(9), 2334–2336.

30. T. Iwai & K. Shigeta (1990). “Experimental study on the spatial correlation properties of speckled speckles using digital speckle photography”. *Japanese journal of applied physics*, **29**, 1099–1102.
31. P. Li, S. Ni, L. Zhang, S. Zeng & Q. Luo (2006). “Imaging cerebral blood flow through the intact rat skull with temporal laser speckle imaging”. *Optics Letters*, **31**, 1824–1826.
32. K. R. Forrester, C. Stewart, J. Tulip, C. Leonard & R. C. Bray (2002). “Comparison of laser speckle and laser Doppler perfusion imaging : measurement in human skin and rabbit articular tissue”. *Medical & Biological Engineering & Computing*, **40**, 687–697.
33. K. R. Forrester, J. Tulip, C. Leonard, S. C. & C. Bray, Robert (2004). “A laser speckle imaging technique for measuring tissue perfusion”. *IEEE Transactions On Biomedical Engineering*, **51**(11), 2074–2084.
34. N. Konishi, Y. Tokimoto, K. Kohra & H. Fujii (2002). “New laser speckle flowgraphy system using CCD camera”. *Optical Review*, **9**(4), 163–196.
35. Y. K. Tan, W. Z. Liu, Y. S. Yew, S. H. Ong & J. S. Paul (2004). “Speckle image analysis of cortical blood flow and perfusion using temporally derived contrasts”. In *International Conference on Image Processing ICIP 2004, Proc.IEEE*, vol. 5, pp. 3323–3326.
36. T. M. Le, J. S. Paul, H. Al-Nashash, A. Tan, A. R. Luft, F. S. Sheu & S. H. Ong (2007). “New insights into image processing of cortical blood flow monitors using laser speckle imaging”. *IEEE Transactions on Biomedical Engineering*, **26**(6), 833–842.
37. A. B. Parthasarathy, W. J. Tom, A. Gopal, X. Zhang & A. K. Dunn (2008). “Robust flow measurement with multi-exposure speckle imaging”. *Optics Express*, **16**(3), 1975–1989.
38. E. Archbold & A. E. Ennos (1972). “Displacement measurement from double-exposure laser photographs”. *Optica Acta*, **19**(4), 253–271.
39. K. Iwata, T. Hakoshima & R. Nagata (1978). “Measurement of flow velocity distribution by multiple-exposure speckle photography”. *Optics Communications*, **25**(3), 311–314.
40. Y. Ganilova, P. Li, D. Zhu, N. Lin, H. Chen, Q. Luo & S. Ulyanov (2006). “Digital speckle-photography, LASCA and cross-correlation

- techniques for study of blood microflow in isolated vessel”. In V. V. Tuchin (ed.) *Saratov Fall Meeting 2005: Optical Technologies in Biophysics and Medicine VII, Proc. SPIE*, vol. 6163, p. 616319. SPIE.
41. J. D. Briers & S. Webster (1996). “Laser speckle contrast analysis (LASCA): a non-scanning, full-field technique for monitoring capillary blood flow”. *Journal of Biomedical Optics*, **1**, 174–179.
 42. J. D. Briers (2001). “Time-varying laser speckle for measuring motion and flow”. In D. A. Zimnyakov (ed.) *Coherent Optics of Ordered and Random Media*, vol. 4242, pp. 25–39.
 43. X. W. He & J. D. Briers (1998). “Laser speckle contrast analysis (LASCA): a real-time solution for monitoring capillary blood flow and velocity”. In E. A. Hoffman (ed.) *Physiology and Function from Multi-dimensional Images, Proc. SPIE*, vol. 3337, pp. 98–107.
 44. J. D. Briers, G. Richards & X. W. He (1999). “Capillary blood flow monitoring using laser speckle contrast analysis (LASCA)”. *Journal of Biomedical Optics*, **4**(1), 164–175.
 45. G. J. Richards & J. D. Briers (1997). “Capillary-blood-flow monitoring using laser speckle contrast analysis (LASCA): improving the dynamic range”. In V. V. Tuchin, H. Podbielska & B. Ovrzyn (eds.) *Coherence Domain Optical Methods in Biomedical Science and Clinical Applications, Proc. SPIE*, vol. 2981, pp. 160–171.
 46. J. D. Briers & X. W. He (1998). “Laser speckle contrast analysis (LASCA) for blood flow visualization: improved image processing”. In A. V. Priezzhev, T. Asakura & J. D. Briers (eds.) *Optical Diagnostics of Biological Fluids III, Proc. SPIE*, vol. 3252, pp. 26–33.
 47. D. A. Zimnyakov, A. B. Mishin, A. A. Bednov, C. Cheung, V. V. Tuchin & A. G. Yodh (1999). “Time-dependent speckle contrast measurements for blood microcirculation monitoring”. In A. V. Priezzhev & T. Asakura (eds.) *Optical Diagnostics of Biological Fluids IV, Proc. SPIE*, vol. 3599, pp. 157–166.
 48. D. A. Zimnyakov & A. B. Misnin (2001). “Blood microcirculation monitoring by use of spatial filtering of time-integrated speckle patterns: potentialities to improve the depth resolution”. In A. V. Priezzhev & G. L. Cote (eds.) *Optical diagnostics and sensing of biological fluids and glucose and cholesterol monitoring, Proc. SPIE*, vol. 4263, pp. 73–82.

-
49. F. C. MacKintosh, J. X. Zhu, D. J. Pine & D. A. Weitz (1989). "Polarization memory of multiply scattered light". *Phys.Rev.B*, **40**(13), 9342–9345.
 50. S. Yuan, A. Devor, D. A. Boas & A. K. Dunn (2005). "Determination of optimal exposure time for imaging of blood flow changes with laser speckle contrast imaging". *Applied Optics*, **44**(10), 1823–1830.
 51. B. Choi, J. C. Ramirez-San-Juan, J. Lotfi & J. S. Nelson (2006). "Linear response range characterization and in vivo application of laser speckle imaging of blood flow dynamics". *Journal of Biomedical Optics*, **11**(4), 041129.
 52. R. Nothdurft & G. Yao (2005). "Imaging obscured subsurface inhomogeneity using laser speckle". *Optics Express*, **13**(25), 10034–10039.
 53. A. C. Völker, P. Zakharov, B. Weber, F. Buck & F. Scheffold (2005). "Laser speckle imaging with an active noise reduction scheme". *Optics Express*, **13**(24), 9782–9787.
 54. R. Bandyopadhyay, A. S. Gittings, S. S. Suh, P. K. Dixon & D. J. Durian (2005). "Speckle-visibility spectroscopy: A tool to study time-varying dynamics". *Review of Scientific Instruments*, **76**(9), 093110.
 55. P. Zakharov, A. Völker, A. Buck, B. Weber & F. Scheffold (2006). "Quantitative modeling of laser speckle imaging". *Optics Letters*, **31**(23), 3465–3467.
 56. H. Cheng & T. Q. Duong (2007). "Simplified laser-speckle-imaging analysis method and its application to retinal blood flow imaging". *Optics Letters*, **32**(15), 2188–2190.
 57. G. DaCosta (1995). "Optical remote sensing of heartbeats". *Optics Communications*, **117**, 395–398.
 58. A. Sadhwani, K. T. Schomacker, G. J. Tearney & N. S. Nishioka (1996). "Determination of teflon thickness with laser speckle.i. potential for burn depth diagnosis". *Applied Optics*, **35**(28), 5727–5735.
 59. J. Kubota (2002). "Effects of diode laser therapy on blood flow in axial pattern flaps in the rat model". *Lasers in Medical Science*, **17**, 146–153.

2 Review of laser speckle contrast techniques for visualizing tissue perfusion

60. B. Choi, N. M. Kang & J. S. Nelson (2004). "Laser speckle imaging for monitoring blood flow dynamics in the in vivo rodent dorsal skin fold model". *Microvascular Research*, **68**(2), 143–146.
61. J. S. Paul, A. R. Luft, E. Yew & F.-S. Sheu (2006). "Imaging the development of an ischemic core following photochemically induced cortical infarction in rats using Laser Speckle Contrast Analysis (LASCA)." *Neuroimage*, **29**(1), 38–45.
62. B. Kruijt, H. S. de Bruijn, A. van der Ploeg-van den Heuvel, H. J. C. M. Sterenborg & D. J. Robinson (2006). "Laser speckle imaging of dynamic changes in flow during photodynamic therapy". *Lasers in Medical Science*, **21**(4), 208–212.
63. T. K. Smith, B. Choi, J. C. Ramirez-San-Juan, J. S. Nelson, K. Osann & K. M. Kelly (2006). "Microvascular blood flow dynamics associated with photodynamic therapy, pulsed dye laser irradiation and combined regimens". *Lasers in Surgery and Medicine*, **38**(5), 532–539.
64. D. Zhu, W. Lu, Y. Weng, H. Cui & Q. Luo (2007). "Monitoring thermal-induced changes in tumor blood flow and microvessels with laser speckle contrast imaging". *Applied Optics*, **46**(10), 1911–1917.
65. K. Murari, N. Li, A. Rege, X. Jia, A. All & N. Thakor (2007). "Contrast-enhanced imaging of cerebral vasculature with laser speckle". *Applied Optics*, **46**(22), 5340–5346.
66. S. K. Nadkarni, B. E. Bouma, T. Helg, R. Chan, E. Halpern, A. Chau, M. S. Minsky, J. T. Motz, S. L. Houser & G. J. Tearney (2005). "Characterization of atherosclerotic plaques by laser speckle imaging". *Circulation*, **112**, 885–892.
67. S. K. Nadkarni, B. E. Bouma, J. de Boer & G. J. Tearney (2008). "Evaluation of collagen in atherosclerotic plaques: the use of two coherent laser-based imaging methods". *Lasers in Medical Science*.
68. A. Serov, W. Steenbergen & F. F. M. de Mul (2002). "Laser Doppler perfusion imaging with a complimentary metal oxide semiconductor image sensor". *Optics Letters*, **27**(5), 300–302.
69. A. Serov, B. Steinacher & T. Lasser (2005). "Full-field laser Doppler perfusion imaging and monitoring with an intelligent CMOS camera". *Optics Express*, **13**(10), 3681–3689.

70. A. Serov & T. Lasser (2005). “High-speed laser Doppler perfusion imaging using an integrating CMOS image sensor”. *Optics Express*, **13**(17), 6416–6428.
71. A. Serov & T. Lasser (2006). “Combined laser Doppler and laser speckle imaging for real-time blood flow measurements”. In G. L. Coté & A. V. Priezzhev (eds.) *Optical Diagnostics and Sensing VI, Proc. SPIE*, vol. 6094, pp. 33–40.
72. M. J. Draijer, E. Hondebrink, T. G. van Leeuwen & W. Steenbergen (2008). “Connecting laser Doppler perfusion imaging and laser speckle contrast analysis”. In G. L. Coté & A. V. Priezzhev (eds.) *Optical Diagnostics and Sensing VIII, Proc. SPIE*, vol. 6863, pp. 68630C–68630C–8.
73. O. B. Thompson & M. K. Andrews (2008). “Spectral density and tissue perfusion from speckle contrast measurements”. In J. A. Izatt, J. G. Fujimoto & V. V. Tuchin (eds.) *Coherence Domain Optical Methods and Optical Coherence Tomography in Biomedicine XII, Proc. SPIE*, vol. 6847, pp. 68472D–68472D–7.

3

The Twente Optical Perfusion Camera: system overview and performance for video rate laser Doppler perfusion imaging

This chapter has been published as : M.J. Draijer, E. Hondebrink, T.G. van Leeuwen, and W. Steenbergen (2009) "The Twente Optical Perfusion Camera: system overview and performance for video rate laser Doppler perfusion imaging", *Optics Express* **17**(5), 3211-3225

Abstract – We present the Twente Optical Perfusion Camera (TOPCam), a novel laser Doppler perfusion imager based on CMOS technology. The tissue under investigation is illuminated and the resulting dynamic speckle pattern is recorded with a high speed CMOS camera.

Based on an overall analysis of the signal-to-noise ratio of CMOS cameras, we have selected the camera which best fits our requirements. We applied a pixel-by-pixel noise correction to minimize the influence of noise in the perfusion images.

We can achieve a frame rate of 0.2 fps for a perfusion image of 128×128 pixels (imaged tissue area of $7 \times 7 \text{ cm}^2$) if the data is analyzed online. If the analysis of the data is performed offline, we can achieve a frame rate of 26 fps for a duration of 3.9 seconds. By reducing the imaging size to 128×16 pixels, this frame rate can be achieved for up to half a minute.

We show the fast imaging capabilities of the system in order of increasing perfusion frame rate. First the increase of skin perfusion after application of capsicum cream, and the perfusion during an occlusion-reperfusion procedure at the fastest frame rate allowed with online analysis is shown. With the highest frame rate allowed with offline analysis, the skin perfusion revealing the heart beat and the perfusion during an occlusion-reperfusion procedure is presented.

3.1 Introduction

Laser Doppler perfusion imaging (LDPI) [1–7] and related techniques like laser speckle contrast analysis (LASCA) [4–6, 8–10] and laser speckle imag-



Figure 3.1: (a) Schematic overview of the measurement head (footprint $21,5 \times 28$ cm) and (b) photo of the entire TOPCam system.

ing (LSI) [11, 12] are established techniques for determining skin perfusion maps, for instance to diagnose burns [6, 13–18], to study cerebral blood flow in small animals [19], and for drug uptake studies (e.g., using iontophoresis) [20].

In commercially available LDPI devices the area under investigation is scanned with a narrow laser beam. Using beam scanning, obtaining a perfusion image of 64×64 pixels takes approximately 3 minutes. This long scanning time impedes the observation of fast perfusion changes, for instance during reperfusion after occlusion. To obtain real time reperfusion images a refresh rate of approximately 25 Hz is needed. Also from the perspective of the patient it is sometimes strongly desirable to have a short imaging time, e.g., for burn patients, and in general for young children and elder patients.

Here we present the Twente Optical Perfusion Camera (TOPCam), a novel laser Doppler perfusion imager based on CMOS technology [3, 21–23] which allows real time acquisition of dynamic laser speckle patterns generated by the tissue perfusion. We discuss various instrumental aspects and present performance studies on phantoms and *in-vivo* measurements.

3.2 The Twente Optical Perfusion Camera

A schematic overview and a photo of the TOPCam is shown in figure 3.1. The TOPCam is equipped with a 671 nm DPSS laser with a power of 400 mW (ML-III-671, CNI-laser). By a mirror the laser light is guided through two filter wheels, which contain filters for adjusting the light intensity by use of a neutral density filter and the beam shape by an engineered diffuser (RPC Photonics). This engineered diffuser transforms the laser beam to a homogeneous square (5% spatial variation in homogeneity) of approximately 7×7 centimeter at 40 cm distance (i.e., the normal working distance). With another mirror the laser light is directed toward the skin. Backscattered laser light from the skin is focused with a motorized zoom lens (lens : T6Z5710M-CS, Computar; controler : CBZ230, Computar) on the high speed CMOS camera (Fastcam 1024PCI, Photron) which can achieve a frame rate of 27 kHz for an area of 128×128 pixels. Using that frame rate, 1024 raw speckle images were recorded and transferred to the computer for analysis. The time trace for every pixel was Fourier transformed using FFT and the power spectrum $S(\omega)$ is obtained. Perfusion maps are generated by calculating for each pixel the first moment of the power spectrum according to :

$$M_1 = \int_{50Hz}^{13.5kHz} \omega S(\omega) d\omega \quad (3.1)$$

To normalize the perfusion image for the amount of light reflected from the tissue, the perfusion image was divided by the DC image (i.e., the mean pixel-by-pixel intensity values), as is commonly used in commercially available laser Doppler perfusion imagers.

3.2.1 Camera selection based on signal-to-noise ratio

To select the high speed camera which fits our requirements the best, we predicted the signal-to-noise ratio (SNR) of several cameras, based on their specifications.

In LDPI the signal is formed by the AC-component of the time fluctuating photo current (i_{AC}). So the SNR is defined as :

$$SNR_{CMOS} = \frac{\langle i_{AC}^2 \rangle}{\langle i_{noise}^2 \rangle} \quad (3.2a)$$

The AC-component of the laser Doppler signal can be written as [24]:

$$\langle i_{AC}^2 \rangle = \gamma(2 - \gamma) \frac{\langle i_{DC} \rangle^2}{2N} \quad (3.2b)$$

with γ the fraction Doppler-shifted photons, N the number of speckles per pixel and i_{DC} the DC-component of the photo current. Furthermore we have assumed the backscattered light to be completely depolarised, leading to a factor 2 in the denominator of equation 3.2b. Under the assumption of a homogeneous laser beam, homogeneous and isotropic diffuse backscattering, this DC-component is given by [25] :

$$\langle i_{DC} \rangle = \frac{k_{back} P_{laser}}{\#pixels} \frac{\pi r^2}{4\pi Z^2} \frac{\lambda}{hc} \eta Q q_e \quad (3.2c)$$

with k_{back} the diffuse reflectivity of the tissue, P_{laser} the laser power, $\#pixels$ the number of pixels over which the laser light is divided, r the radius of the lens, Z the distance between the lens and the sample, λ the laser wavelength, h the constant of Planck, c the speed of light, η the fill factor of the CMOS chip, Q the quantum efficiency of the CMOS chip and q_e the charge of one electron.

The number of speckles on one pixel (N) is equal to the ratio of the area of the pixel (A_{pixel}) to the speckle area ($A_{speckle}$) :

$$N = \frac{A_{pixel}}{A_{speckle}} \quad (3.2d)$$

The speckle size is given by :

$$A_{speckle} = \frac{\lambda^2}{\Omega} = \lambda^2 \frac{R^2}{\pi r^2} \quad (3.2e)$$

with Ω the solid angle of the lens on the CMOS chip and R the distance between the lens and the CMOS chip. The noise is composed of shot noise ($2q_e \langle i_{DC} \rangle$), dark noise ($2q_e i_{dark}$) and quantization noise ($2q_e i_{AD}$) (i.e., i_{AD} is the current which corresponds to the number of quantization electrons, which equals the well capacity divided by the number of bit levels) [26] :

$$\langle i_{noise}^2 \rangle = 2q_e (\langle i_{DC} \rangle + i_{dark} + i_{AD}) B_R \quad (3.2f)$$

with B_R the bandwidth of the high speed CMOS camera.

3 The Twente Optical Perfusion Camera: system overview and performance

Table 3.1: Values of the different parameters in equation 3.2 used to predict the SNR of several high speed CMOS cameras.

parameter	CCi4	Redlake HS-4	Phantom V7.1	1024PCI FastCam
λ (nm)	632	671	671	671
r (mm)	17	14	14	14
γ	1	0.1	0.1	0.1
k_{back} ^a	0.5	0.5	0.5	0.5
f_{sample} (kHz)	3.3	30	30	30
B_R (kHz)	20	100	100	100
image size (px)	40×40	128×128	128×128	128×128
imaged area (cm)	$\varnothing 2$	5×5	5×5	5×5
R (mm)	17.526 ^b	17.526 ^b	17.526 ^b	17.526 ^b
Z (cm)	85	42.8	31.1	40.3
pixel pitch (μm)	7	16	22	17
Q	0.2	0.37	0.4	0.3
fill factor	0.6	0.62	0.65	0.6
bit depth	10	8	10	10
well capacity (electrons)	$55e3$	$60e3$	$80e3$	$60e3$

^a based on Monte Carlo simulations.

^b defined distance for a C-mount lens.

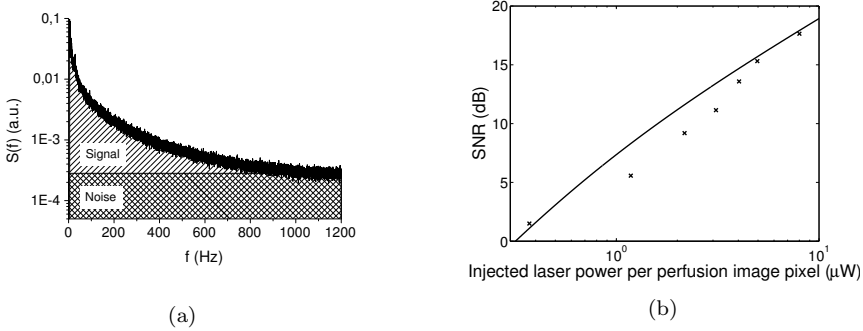


Figure 3.2: (a) schematic overview of the signal part (/ -hatched) and noise part (\times -hatched) for determining the SNR from the power spectrum. (b) comparison between the measured SNR (\times) and the SNR (solid line) calculated with equation 3.2.

To test how accurately the SNR can be predicted by equation 3.2a-3.2f, we measured and calculated the SNR for a CMOS camera available in our lab (CCi4, C-Cam). The parameters which are used to calculate the SNR according to equation 3.2 are shown in table 3.1. To measure the SNR we obtained the perfusion map of a Delrin disk with a hole filled with *IntraLipid* 4% (Fresenius Kabi) for different light intensities (i.e., different P_{laser} in equation 3.2c). As laser source we used a 10 mW HeNe laser with a wavelength of 632 nm. With a lens the laser beam was enlarged to a diameter of approximately 2 cm. To vary the amount of light falling on the sample a rotatable polarizer was positioned between the laser and the sample. Based on the laser Doppler signal from the area with *IntraLipid*, we determined the power spectrum. From this power spectrum we extracted the SNR: the average amplitude of the plateau for higher frequencies was taken to be the noise level. The noise part was determined by calculating the area under the noise level. The signal part was taken by calculating the area under the power spectrum after subtracting the noise part. This is schematically shown in figure 3.2(a). The SNR was determined by dividing the signal part by the noise part. Figure 3.2(b) shows a comparison between the average measured SNR in 10×10 pixels and the calculated SNR based on equation 3.2.

Figure 3.2(b) shows that the predictions provided by equation 3.2a-3.2f are sufficiently accurate to be used as a tool for selection of a CMOS camera for

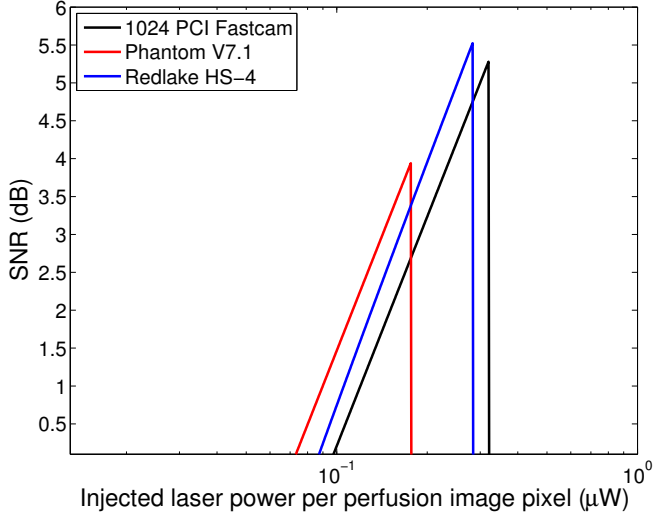


Figure 3.3: The predicted SNR for possible CMOS cameras in high speed LDPI as a function of injected laser power per perfusion image pixel.

LDPI. Figure 3.3 shows the predicted SNR for several high speed cameras which we considered for LDPI. The parameters which are used to calculate the SNR are shown in table 3.1. The well capacity is the number of electrons a pixel can detect before getting saturated. This number is used to determine the amount of injected laser power which saturates the camera and results in a SNR of 0. In the simulations the image size is kept constant at 128×128 pixels while the imaged tissue area is taken equal to $5 \times 5 \text{ cm}^2$, resulting in a constant laser power per pixel (i.e., constant i_{DC}) and a different magnification for all cameras. As expected, more laser power will increase the SNR. The main reason for the higher SNR for the Phantom compared to the Redlake and FastCam is the difference in quantum efficiency Q in equation 3.2c. The truncation of the predicted SNR values for a certain laser power is due to saturation of the pixels. With a certain amount of light falling on a pixel, the well is completely filled and $\langle i_{AC} \rangle$ drops to 0 resulting in a SNR of 0. The highest SNR for a given amount of injected light can be obtained by the *Redlake HS-4*, however, in practical use we found both cameras to be equivalent so we have selected the *1024PCI FastCam*.

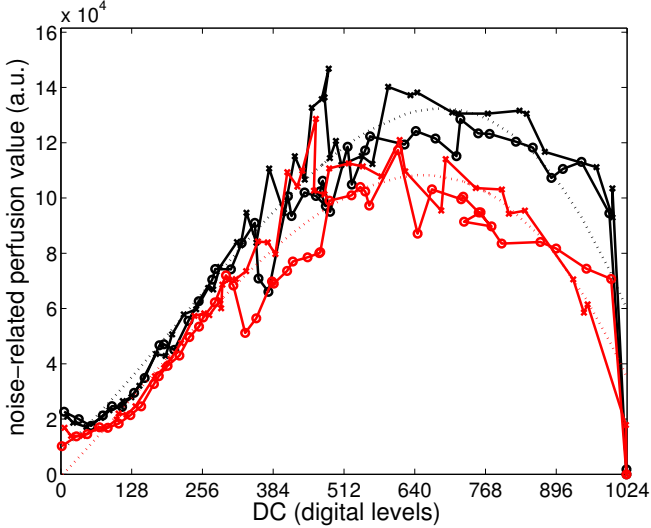


Figure 3.4: Typical examples of the perfusion values due to noise as a function of DC on day 1 (o), day 4 (x) and the correction curves based on a 3^{rd} order fit (dashed lines).

3.2.2 Noise correction

Noise in the generated raw signals will lead to an offset in the measured perfusion values. To correct for that, we measured for all pixels individually the perfusion signal as a function of the amount of light backscattered from a block of Delrin, illuminated by light of a light emitting diode (LED) of 630 nm. The light from a LED is incoherent and Delrin is a static medium, so all perfusion signal can be classified as noise. A 3^{rd} order fit through these measurements results in a noise correction curve for each pixel. Examples of measured noise curves (i.e., M_1 as a function of the DC value) for 2 separate pixels, measured on 2 separate days, and the 3^{rd} order fits (i.e., best fit through the data of both days) are shown in figure 3.4. An increase in DC results in an increase in shot noise in equation 3.2f, which explains the larger noise with increasing DC. The exact reason for the decrease after 650 digital levels is not known yet. In view of our experience with other cameras, we believe that this is a feature of the specific device. The end result of noise-estimation based on the asymptotic value of the power spectrum, or based on the detected DC level will be the same. However, during measurements

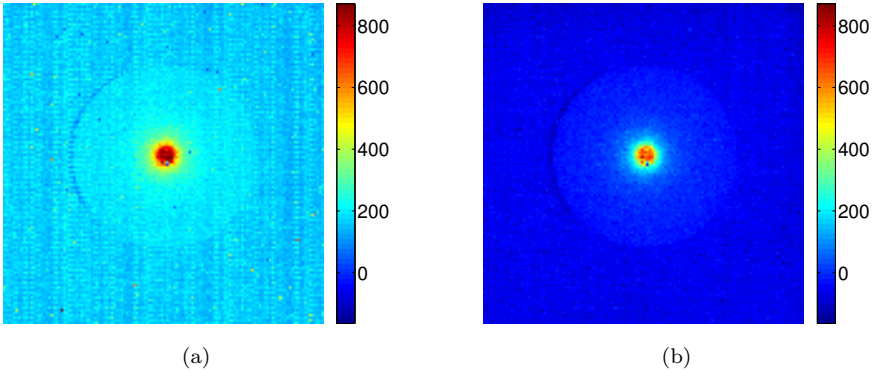


Figure 3.5: (a) DC-normalized raw perfusion image (128×128 pixels) of a piece of Delrin of 40 mm in diameter with a hole of 4 mm in diameter, placed on green surgery paper. The hole was filled with *IntraLipid 20%*. (b) the DC-normalized noise corrected perfusion image of the same sample.

the use of the DC level for noise estimation algorithmically more simple.

Based on the DC-value of each pixel, the measured perfusion value can be corrected by subtraction of a value given by the 3^{rd} order correction function. Figure 3.5 shows a DC-normalized uncorrected as well as noise-corrected perfusion image for a circular piece of Delrin with holes of various diameter, placed on green surgery paper. The hole of 4 mm in diameter was filled with *IntraLipid 20%*.

3.2.3 Speed performance of system

Table 3.2 gives an overview of the current speed of the TOPCam in numbers for two different image sizes (i.e., 128×128 pixels and 128×16 pixels). The TOPCam can be used in two different modes of data analysis, referred to as online and offline. In the online mode the data for a single perfusion frame are recorded and immediately analyzed before the next measurement is performed. In the offline mode the analysis is postponed, first the data for all measurements are recorded and afterwards the data are analyzed. The online mode allows for a measurement series of unlimited duration, with the perfusion frame rate limited by the transfer speed of the camera (0.2 fps). In the offline mode, a maximum perfusion framerate of 26 fps can be

achieved that is related to the raw image capture frame rate. The duration of a recording in offline mode is limited by the memory of the camera, as indicated in table 3.2. The table also indicates that the reduction in time is not linear with the amount of data transferred or the amount of data stored. This is probably caused by overhead in the data-transfer and storage (e.g., handshaking in the transfer-protocol, time needed by the computer to creating a file -regardless of the image size-).

3.3 Demonstration of real time imaging capabilities

The main advantage of the TOPCam over commercially available LDPI devices is the imaging speed. In this section examples of the faster imaging opportunities of the TOPCam will be shown.

Table 3.2: Overview of the system speed averaged over 5 measurements for an 10-bits recording of a sequence of 1024 raw images at a frame rate of 27 kHz.

	128 × 128 px	128 × 16 px
data acquisition (msec)	38	38
data transfer (msec)	3096	2705
storage (msec)	1366	1150
signal processing (msec)	998	159
length of offline perfusion recording with current memory ^a (sec)	3.87	30.95
length of offline perfusion recording with maximal memory ^b (sec)	46.44 ^c	371.40 ^c

^a current memory is 2 Gb

^b maximal memory is 24 Gb

^c based on extrapolation of current amount of memory

3 The Twente Optical Perfusion Camera: system overview and performance

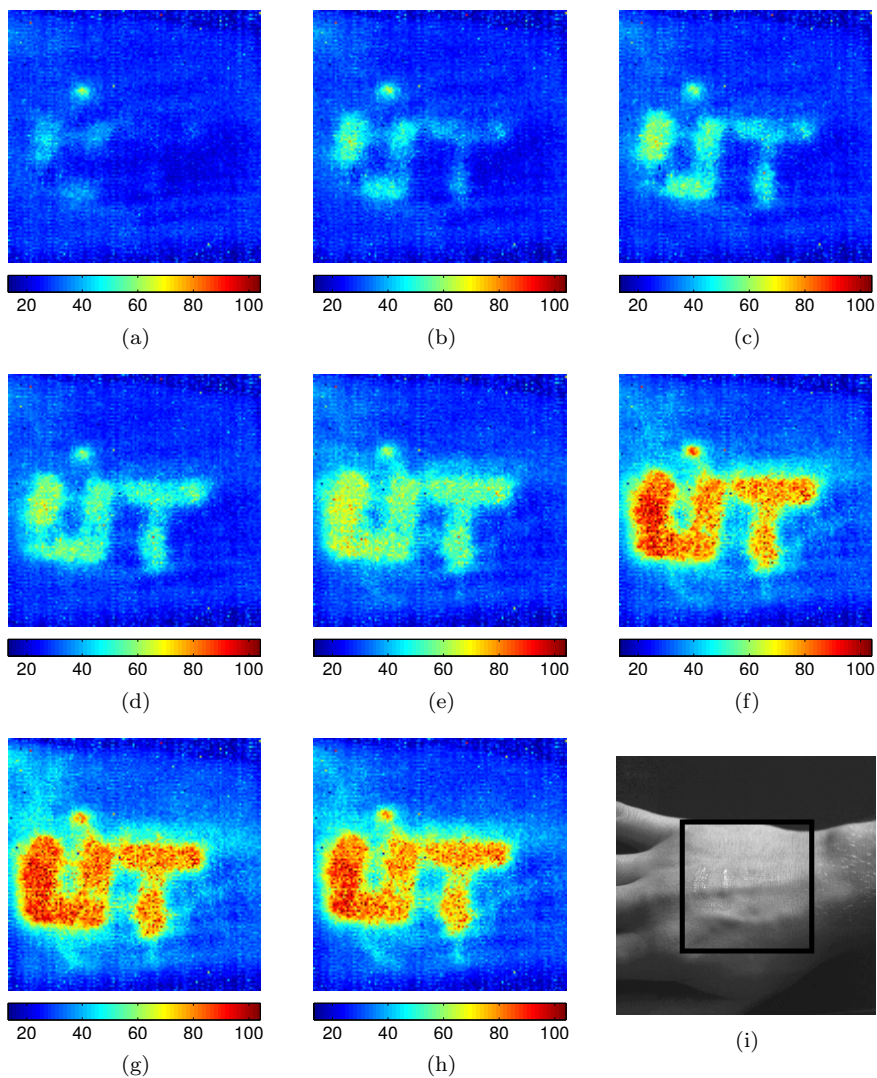


Figure 3.6: The letters UT ('University of Twente') written with capsicum cream on the back of the hand of a volunteer. DC-normalized perfusion image (128×128 pixels) after (a) 3:41 min, (b) 4:32 min, (c) 5:13 min, (d) 7:14 min, (e) 11:36 min, (f) 12:08 min, (g) 13:48 min and (h) 15:13 min. (i) Photo of the hand taken with the CMOS camera, the black square indicates the area in which the perfusion is measured.

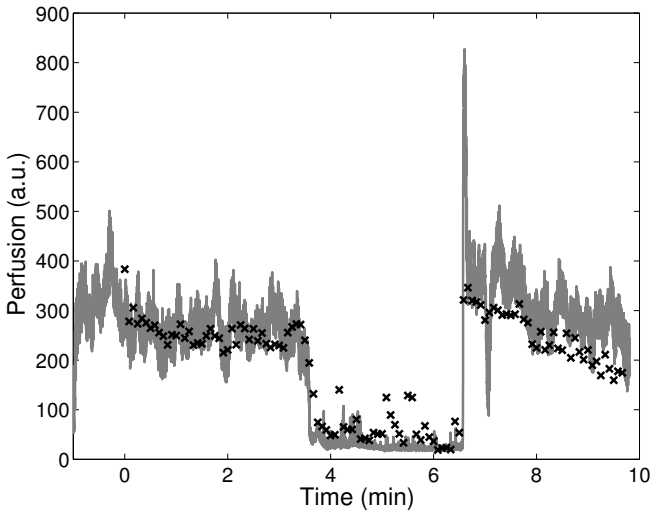


Figure 3.7: Comparison of the readings of the TopCAM (x) and the Periflux5000 (Perimed, Sweden) during an occlusion-reperfusion procedure on the wrist of a volunteer.

3.3.1 Methods and results

Online recording

For the first example the online mode was chosen to follow an increase in perfusion over a longer period of time (e.g 15 minutes). With capsicum cream (Midalgan, Remark Groep BV, Meppel, the Netherlands), a perfusion increasing cream, the letters UT were written on the dorsal side of the hand of the subject (male, 32 yr). Immediately after application of the cream the measurement was started and approximately every 45 seconds a perfusion measurement was performed. Figure 3.6 shows a selection of the sequence of DC-normalized perfusion images as well as a photo taken with the CMOS camera, the black square indicates the area in which is measured. Normal perfusion is indicated by blue whereas increased perfusion is shown in red. The images show a clear increase in perfusion over time due to the cream.

To investigate how the reading of the TOPCam corresponds to the reading of a commercially available fiber optic laser Doppler flow meter, we used

the TOPCam in online mode together with the Periflux5000 with fiberoptic probe 145-198 (Permed AB, Sweden). Measurements were performed on the thenar eminence (Periflux5000) and the wrist (TopCam) of a healthy subject (male, 26 yr). The Periflux5000 recorded 32 samples per second whereas the TOPCam recorded a perfusion image every 5 seconds. The Periflux5000 and TOPCam can not measure at the same location so the probe of the Periflux5000 was placed next to the area imaged by the TOPCam. Approximately 3.5 minutes after starting the TOPCam measurement occlusion was applied by inflating a blood pressure cuff around the upper arm of the subject. After 3 minutes the occlusion was released and the measurements continued for another 3 minutes [27]. Figure 3.7 shows the result of this comparison. The value for the perfusion of the TOPCam is obtained by taking the average value of the whole perfusion image after noise correction and normalization with DC. The reading of the Periflux5000 is multiplied with a factor 3.6 to scale it with the TOPCam. A clear decrease during the occlusion and an increase after the occlusion are present.

Offline recording

Offline recording was chosen for the third example : following fast changing perfusion levels (e.g., the heart beat) in the dorsal side of the hand of the subject (female, 23 yr) in rest. Due to the available memory of 2 Gb in the CMOS camera we measured only for 3.8 seconds with an image size of 128×128 pixels. The recording is shown in figure 3.8. In figure 3.8(a) the average value of each perfusion image is shown as a function of time. Figure 3.8(b) - (d) show the perfusion images at positions B, C and D, respectively, in figure 3.8(a) and figure 3.8(e) show the DC image at position B in figure 3.8(a).

To increase length of the recorded sequence, the image size was reduced to 128×16 pixels whereas the data were stored as 12-bits (i.e., requiring twice the amount of memory compared to 10 bits), resulting in an increase of the length of the recorded sequence in offline mode to 15.5 seconds. An occlusion was applied by inflating a blood pressure cuff around the upper arm of a healthy subject (male, 27 yr). The measurement on the wrist was started 3 minutes after the occlusion was applied. Approximately 3 seconds after the start of the measurement the occlusion was released. These results are shown in figure 3.9. In figure 3.9(a) the average value of each perfusion image is shown as a function of time, and figure 3.9(b) and (c) show the

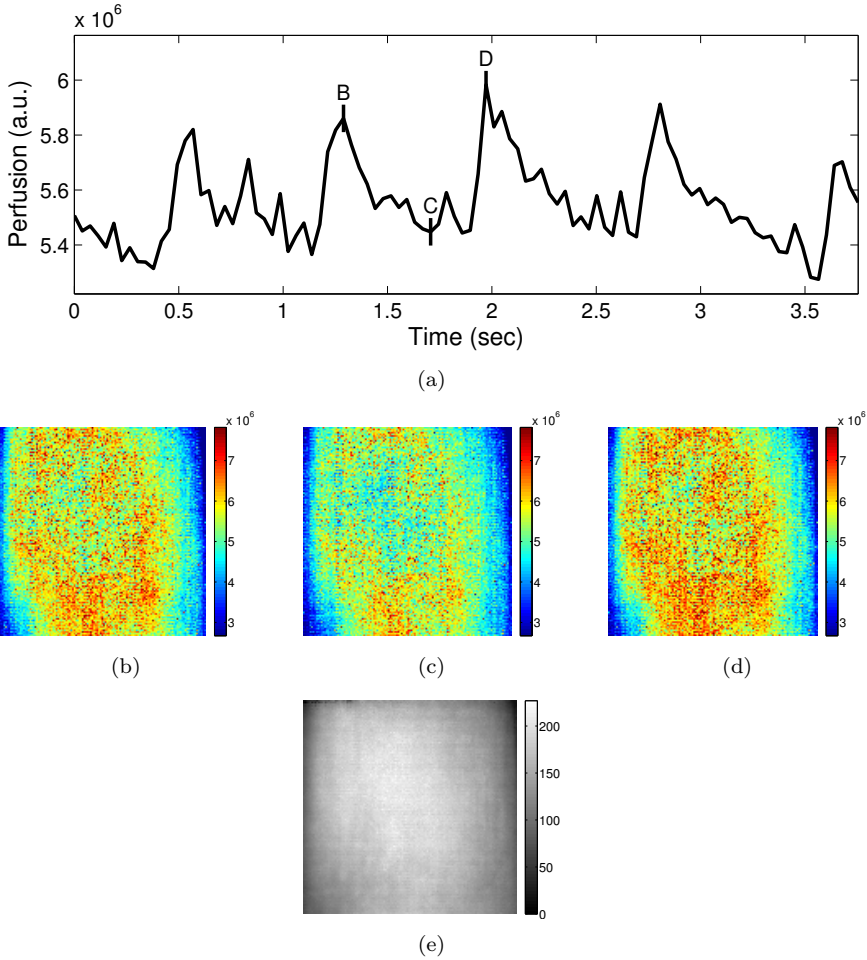


Figure 3.8: Continuous recording of 128×128 pixel perfusion images in the hand of a healthy subject. (a) the average value of each perfusion image as function of time. (b) - (d) perfusion images at times B, C and D in figure (a) and (e) the DC image at times B in figure (a).

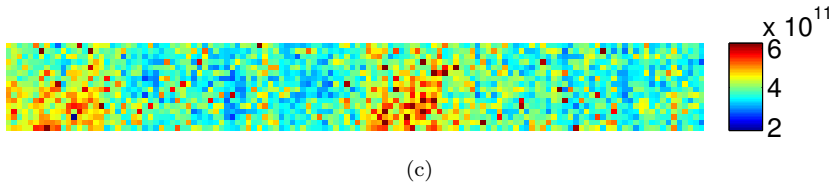
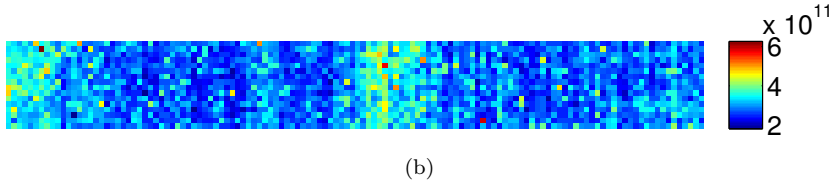
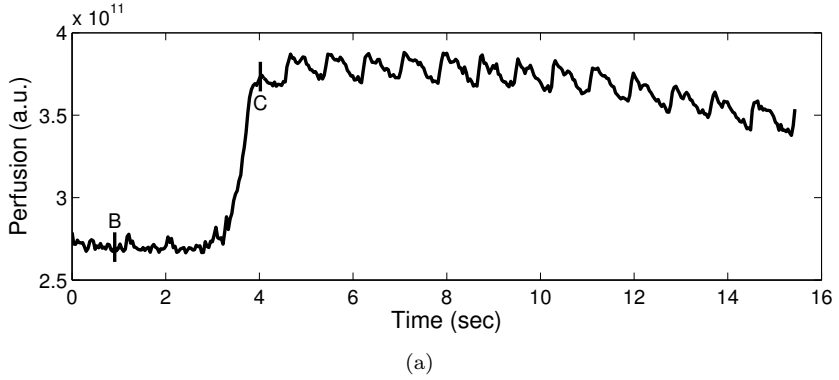


Figure 3.9: Continuous recording of 128×16 pixel perfusion images in the wrist of a healthy subject. (a) the average value of each perfusion image as function of time. (b) and (c) perfusion images at times B and C in figure (a).

perfusion images at positions B and C, respectively, in figure 3.9(a). A clear increase in perfusion is visible after release of the occlusion.

3.4 Discussion

In this study, various instrumental aspects of the TOPCam have been described and the capabilities for fast imaging of skin perfusion are demonstrated. To correct for the noise in the CMOS camera, noise correction

curves were measured, which for each pixel relate the noise generated contribution of the first order moment to the DC-level of that pixel. These curves were fitted with a 3^{rd} order polynomial and the coefficients were stored. However, this fitting can induce a small error in the calculation of the noise level. This can be seen in figure 3.4 where for some DC-values a clear difference between the raw noise curve and the fitted noise correction curve is visible. Figure 3.4 also shows noise measurements for the same pixel on two different days. The difference between these two measurements, which could be a temperature effect in the camera, gives an indication of the reproducibility of the noise correction curves. For low DC-levels a nice agreement is present between the measurements on the different days. For higher DC-levels a difference is visible between the two days. So the amount of noise differs significantly from one day to another. This day-by-day difference also induces a non-perfect estimation of the noise level, which results in an under- or overestimation of the perfusion level. Figure 3.5(b) shows the consequences of these differences between days and inaccurate noise estimation as a result of the fitting. In the ideal case the Delrin and background should both give a zero perfusion level. Due to the non-perfect pixel-by-pixel noise correction a difference is visible between the perfusion level of the Delrin and the background. The level of noise is only dependent on the properties of the camera and the detected DC level of the light, so the noise level obtained empirically on Delrin can also be used for in-vivo measurements. In figure 3.5(a) vertical stripes are present, these stripes are suppressed in figure 3.5(b) due to the applied noise correction. For low DC-values (e.g below 128 digital levels) the 3^{rd} order deviates from the measured curves. A 4^{th} or higher order polynomial fit removed this deviation but resulted in a deviation for higher DC-values, which is undesirable because the measurements are usually performed in that range of DC values.

The TOPCam allows us to follow the increase of perfusion in an extended tissue area, e.g., in response to the application of capsicum cream (figure 3.6). In all the images a spot with higher perfusion than the surrounding tissue is visible. This is caused by a small wound which was present at the hand of the subject during the measurement. Furthermore, TOPCam imaging revealed that the capsicum cream does not only increase the perfusion at the location where the cream was applied, but also slightly in the area around it.

In the comparison between the TOPCam and the fiberoptic laser Doppler probe (figure 3.7), a difference can be observed between the signals measured

by the TOPCam and the probe, which might be caused by the different regions probed by the fiberoptic probe and the TOPCam. Another difference between both devices is the algorithm used to process the signal and the different measurement depth. Due to this difference in measurement depth, both devices measure a slightly different part of the micro circulation which can explain the difference in perfusion. Another difference between the two measurements is an overshoot with a duration of a few seconds after the release of the occlusion measured with the laser Doppler probe, which is not recorded by the TOPCam. A zoom-in on the overshoot (not shown) reveals that during the overshoot the TOPCam was processing the data from the previous measurement, and therefore could not measure the overshoot. Another striking detail is the variation in the signal from the TOPCam during the occlusion. Because the signal for the TOPCam is obtained by averaging over a large number of pixels, the pixel to pixel variations in optoelectronic properties should cancel out. The exact reason for this difference is not known yet.

The average time between the peaks in the continuous measurement (i.e., figure 3.8) is 746 milliseconds, resulting in a heart beat frequency of 80 beats per minute, which is in the range of normal heart frequencies. In between the heart beats some smaller variations are visible. These variations occur at a time scale of approximately 0.1 second. When the pressure wave of blood arrives at a vascular branch in larger vessels, part of the wave hits the wall and reflects back where it interferes with the end of the pressure wave. This causes variations at the time scale of approximately 0.1 second, so called dicrotic notches. However, it is unlikely that these flow variations reach the micro circulation. These small excursions of the flux signal are probably caused by overall tissue motion due to the pressure waves in the larger arteries. In the center of the DC image (figure 3.8(e)) an area with a slightly higher intensity due to curvature of the hand is visible. In the perfusion images this area is visible with a lower perfusion, indicating the perfusion image is over-normalized.

After the release of the occlusion in the longer continuous measurement (figure 3.9) the same variations can be observed in the flux signal. The average time between the heart beat peaks is 825 milliseconds, which corresponds with a heart beat frequency of 73 beats per minute, which is in the normal range. However, during the occlusion the average perfusion level does not approach zero. This can partially be explained by the non-perfect pixel-by-pixel noise correction as discussed above. A possible other explanation is

that the blood pressure cuff was not inflated completely, so the blood supply was not fully blocked. As was the case in the comparison between the TOPCam and the laser Doppler probe from Perimed (figure 3.7), in this figure a steady decrease is visible after the first increase of perfusion after release of the occlusion. After 11 seconds the perfusion already dropped to 70% of the difference between the baseline and the first increase.

Table 3.2 shows that the most time consuming part in the imaging process of the TOPCam is the transfer of data from the camera to the computer to process the data. This long time is mainly caused by the protocol used by the camera to communicate with the computer. Improving this protocol will result in a considerable increase of imaging speed for uninterrupted perfusion imaging. Furthermore processing could be improved by making use of parallel processing (e.g., graphics card or dual/quatro core processor) resulting in a further increase of imaging speed.

One of the major benefits of a high speed camera based on CMOS image array technology to image perfusion is the fast imaging speed, which is superior to that of scanning beam laser Doppler perfusion imagers. Furthermore it gives the opportunity to make a photo with the same sensor that was used for the measurement. In this way the perfusion image can simply be overlaid with the photo for easy orientation. However, using a high speed CMOS camera also has some drawbacks. Due to the different amplifiers for different pixel columns, fixed pattern noise will be induced in the measurements, resulting in images which are noisier than those produced by scanning beam laser Doppler perfusion imagers. However, this issue will probably be solved by further technological sophistication. In newer CMOS-cameras, already a smaller fixed pattern noise is observed. Furthermore, analog filtering of the photocurrent fluctuations is not possible with commercial CMOS imaging arrays, so high pass filtering (i.e., to suppress moving artifacts) and low pass filtering (i.e., to prevent aliasing) can not be done. To be able to perform analog filtering custom made CMOS imaging arrays are required [28]. Due to the high imaging speed, motion artifacts will play a minor role and by selecting a high frame rate, the possibility of aliasing can be reduced. We have shown that current high speed CMOS cameras enable real time perfusion imaging, but with a lower signal-to-noise ratio than a scanning beam imager. However, since the high speed feature allows for multiple imaging and averaging, this difference in signal-to-noise ratio might partly be overcome.

3.5 Conclusion

In conclusion, we have presented the Twente Optical Perfusion Camera (TOPCam), a novel laser Doppler perfusion imager based on CMOS image array technology. To correct for the noise in the CMOS camera, noise correction curves based on a 3rd order fit through the measured noise were determined. This non-perfect fit results in an under- or overestimation of the perfusion level.

The TOPCam can be used in two different imaging modes. In the online mode data for one perfusion frame are recorded and immediately analyzed before the next measurement is performed. Using this imaging mode we can achieve a frame rate of 0.2 fps without time limitation. In the offline mode the analysis is postponed, first the data for all measurements are recorded before the data are analyzed. Using this imaging mode we can achieve a frame rate of 26 fps for 3.87 seconds (i.e perfusion images of 128×128 pixels) up to 15.47 seconds (i.e perfusion images of 128×32 pixels) or even longer if the data are stored as 10-bit instead of 12 bit data. Using a lens with a focal length of 12 mm, we can image an area of approximately 7×7 centimeter at 40 cm distance (i.e., the normal working distance) on 128×128 pixels.

The imaging speed of the TOPCam is superior to scanning beam laser Doppler perfusion imagers. Further research is needed to characterize the imaging quality and imaging properties (e.g., measurement depth, resolution, response to different tissue types) of the TOPCam with respect to scanning beam laser Doppler perfusion imagers.

References

1. R. Bonner & R. Nossal (1981). “Model for laser Doppler measurements of blood flow in tissue”. *Applied Optics*, **20**(12), 2097–2107.
2. Y. Aizu & T. Asakura (1991). “Bio-speckle phenomena and their application to the evaluation of blood flow”. *Optics & Laser Technology*, **23**(4), 205–219.
3. A. Serov, W. Steenbergen & F. F. M. de Mul (2002). “Laser Doppler perfusion imaging with a complimentary metal oxide semiconductor image sensor”. *Optics Letters*, **27**(5), 300–302.

4. J. D. Briers (1996). “Laser Doppler and time-varying speckle: A reconciliation”. *Journal of The Optical Society of America, A*, **13**(2), 345–350.
5. J. D. Briers (2001). “Laser Doppler, speckle and related techniques for blood perfusion mapping and imaging”. *Physiological Measurements*, **22**, R35–R66.
6. C. J. Stewart, R. Frank, K. R. Forrester, J. Tulip, R. Lindsay & R. C. Bray (2005). “A comparison of two laser-based methods for determination of burn scar perfusion: Laser Doppler versus laser speckle imaging”. *Burns*, **31**, 744–752.
7. M. J. Draijer, E. Hondebrink, T. G. van Leeuwen & W. Steenbergen (2008). “Connecting laser Doppler perfusion imaging and laser speckle contrast analysis”. In G. L. Coté & A. V. Priezzhev (eds.) *Optical Diagnostics and Sensing VIII, Proc. SPIE*, vol. 6863, pp. 68630C–68630C–8.
8. A. F. Fercher & J. D. Briers (1981). “Flow visualization by means of single-exposure speckle photography”. *Optics Communications*, **37**(5), 326–330.
9. J. D. Briers, G. Richards & X. W. He (1999). “Capillary blood flow monitoring using laser speckle contrast analysis (LASCA)”. *Journal of Biomedical Optics*, **4**(1), 164–175.
10. M. J. Draijer, E. Hondebrink, T. G. van Leeuwen & W. Steenbergen (2009). “Review of laser speckle contrast techniques for visualizing tissue perfusion”. *Lasers in Medical Science*, **24**(4), 639–651.
11. H. Cheng, Q. Luo, S. Zeng, S. Chen, J. Cen & H. Gong (2003). “Modified laser speckle imaging method with improved spatial resolution.” *Journal of Biomedical Optics*, **8**(3), 559–564.
12. H. Cheng & T. Q. Duong (2007). “Simplified laser-speckle-imaging analysis method and its application to retinal blood flow imaging”. *Optics Letters*, **32**(15), 2188–2190.
13. Z. B. M. Niazi, T. J. H. Essex, R. Rapini, D. Scott, N. R. McLean & M. J. M. Black (1993). “New laser Doppler scanner, a valuable adjunct in burn depth assessment”. *Burns*, **19**(6), 485–489.
14. S. A. Pape, C. A. Skouras & P. O. Byrne (2001). “An audit of the use of laser Doppler imaging (LDI) in the assessment of burns of intermediate depth”. *Burns*, **27**, 233–239(7).

15. F. W. Kloppenberg, G. I. Beerthuis & H. J. ten Duis (2001). “Perfusion of burn wounds assessed by laser Doppler imaging is related to burn depth and healing time.” *Burns*, **27**, 359–363.
16. E. J. Droog, W. Steenbergen & F. Sjöberg (2001). “Measurement of depth of burns by laser Doppler perfusion imaging”. *Burns*, **27**, 561–568.
17. R. Bray, K. Forrester, C. Leonard, R. McArthur, J. Tulip & R. Lindsay (2003). “Laser Doppler imaging of burn scars: A comparison of wavelength and scanning methods”. *Burns*, **29**(3), 199–206.
18. E. La Hei, A. Holland & H. Martin (2006). “Laser Doppler imaging of paediatric burns: Burn wound outcome can be predicted independent of clinical examination”. *Burns*, **32**, 550–553.
19. A. K. Dunn, H. Bolay, M. A. Moskowitz & D. A. Boas (2001). “Dynamic imaging of cerebral blood flow using laser speckle”. *Journal of Cerebral Blood Flow and Metabolism*, **21**(3), 195–201.
20. F. F. M. de Mul, J. Blaauw, J. G. Aarnoudse, A. J. Smit & G. Rakhorst (2007). “Diffusion model for iontophoresis measured by laser-Doppler perfusion flowmetry, applied to normal and preeclamptic pregnancies”. *Journal of Biomedical Optics*, **12**(1), 14032–1.
21. A. Serov, B. Steinacher & T. Lasser (2005). “Full-field laser Doppler perfusion imaging and monitoring with an intelligent CMOS camera”. *Optics Express*, **13**(10), 3681–3689.
22. A. Serov & T. Lasser (2005). “High-speed laser Doppler perfusion imaging using an integrating CMOS image sensor”. *Optics Express*, **13**(17), 6416–6428.
23. M. J. Draijer, E. Hondebrink, W. Steenbergen & T. G. van Leeuwen (2007). “Laser Doppler perfusion imaging with a high-speed CMOS-camera”. In C. D. Depeursinge (ed.) *Novel Optical Instrumentation for Biomedical Applications III, Proc. SPIE*, vol. 6631, p. 66310N.
24. A. Serov, W. Steenbergen & F. F. M. de Mul (2001). “Prediction of the photodetector signal generated by Doppler-induced speckle fluctuations: theory and some validations”. *J. Opt. Soc. Am. A*, **18**(3), 622–630.
25. E. Hecht (1998). *Optics*. Addison-Wesley, 3 ed.

26. G. Rieke (2003). *Detection of Light*. Cambridge University Press, 2 ed.
27. A. Humeau, J. L. Saumet & J. P. L. Huillier (2000). “Simplified model of laser Doppler signals during reactive hyperaemia”. *Medical & Biological Engineering & Computing*, **38**, 80–87.
28. Q. Gu, B. R. Hayes-Gill & S. P. Morgan (2008). “Laser Doppler blood flow complementary metal oxide semiconductor imaging sensor with analog on-chip processing”. *Applied Optics*, **47**(12), 2061–2069.

4

Burn imaging with a whole field laser Doppler perfusion imager based on a CMOS imaging array

This chapter has been published as : H.E. van Herpt, M.J. Draijer, E. Hondebrink, M.N. Nieuwenhuis, G. Beerthuizen, T.G. van Leeuwen, and W. Steenbergen (2009) "Burn imaging with a whole field laser Doppler perfusion imager based on a CMOS imaging array", in press *Burns*

Abstract – Laser Doppler perfusion imaging (LDPI) has been proven to be a useful tool in predicting the burn wound outcome in an early stage. A major disadvantage of scanning beam LDPI devices is their slow scanning speed, leading to patient discomfort and imaging artifacts. We have developed the Twente Optical Perfusion Camera (TOPCam), a whole field laser Doppler perfusion imager based on a CMOS imaging array, which is two orders of magnitude faster than scanning beam LDPI systems. In this paper the first clinical results of the TOPCam in the setting of a burn centre are presented. The paper shows perfusion images of burns of various degrees. While our system encounters problems caused by blisters, tissue necrosis, surface reflection and curvature in a manner similar to scanning beam imagers, it poses a clear advantage in terms of procedure time. Image quality in terms of dynamic range and resolution appears to be sufficient for burn diagnosis. Hence, we made important steps in overcoming the limitations of LDPI in burn diagnosis imposed by the measurement speed.

4.1 Introduction

Proper determination of the burn depth is crucial for the choice of the optimal wound treatment. In burns with an intermediate depth (also called partial thickness burns), the early prognostication of the likely burn wound outcome is difficult during the first days after injury [1, 2]. In these intermediate burn depths, even experienced burn surgeons have an accuracy of their clinical assessment of burn depth of 60-80% [3–7]. In literature several potential objective methods to determine burn depth in an early stage after injury are reported, one of which is laser Doppler perfusion imaging (LDPI).

The superficial partial thickness burns have a more active microcirculation compared to normal 'unaffected' skin, while the microcirculation in deep

partial thickness burn wounds is impaired or lost [8]. These differences are used in the burn assessment with LDPI: the superficial partial thickness burns show perfusion values greater than those of unaffected skin, whereas the deep partial thickness burns have perfusion values lower than unaffected skin [9, 10].

Various researchers have investigated the accuracy of LDPI measurements in burn diagnosis and showed a high accuracy [2, 11–14] which makes LDPI a powerful tool in the field of burn depth assessment.

Most commercially available laser Doppler perfusion imagers are scanning beam devices that require the patient not to move for a few minutes. Since a vulnerable group of burn patients is younger children there is a need for a faster full-field imaging system like laser speckle contrast analysis (LASCA) [15] or LDPI with high speed cameras [16, 17]. LASCA has the disadvantage that the relation between the contrast and the perfusion is unknown, whereas LDPI has proven to be useful in burn care. The Twente Optical Perfusion Camera (TOPCam), a novel laser Doppler perfusion imager, reduces the total acquisition time to just 38 ms. [18]. The TOPCam has a short acquisition time thanks to the use of a high speed CMOS camera, in combination with illumination of a large tissue area. Another advantage of this device is its ability to render photographic images of the tissue site with the same sensor, which makes it easy to merge the perfusion and topographic images.

The aim of this study was to evaluate the capability and efficacy of the TOPCam to measure perfusion differences in burn wounds. Since it is reported that for example blisters, curvature and crusts can influence the perfusion values in the LDPI measurement [8, 10], the effects of different wound appearances are investigated and also a comparison with a commercial scanning beam LDPI device, a PIM II system (Permed AB, Sweden), is performed.

4.2 Subjects and methods

4.2.1 Patients

In the period between June-August 2007 inpatients and outpatients of the Burn Center in the Martini Hospital Groningen (the Netherlands) were asked to participate in the study on a strictly voluntary basis. Patients with psychiatric problems, multi-system trauma and children under 16 years old were excluded. For safety reasons no measurements were performed on burns on the head of a patient.

The study was approved by the Medical Ethics Committee of the Martini Hospital.

4.2.2 Equipment

Our whole field LDPI device (the TOPCam), including its signal processing, is described in detail in reference [18]. The TOPCam uses a diffused laser beam (400 mW, $\lambda = 671 \pm 0.1$ nm, class 2M) that illuminates a tissue area of 5×5 cm² up to 15×15 cm² at once. The used CMOS chip has 1024×1024 pixels but only an area of 128×128 pixels is used; each pixel acts as an individual detector. The whole setup was mounted on a trolley with an articulated arm. The microcirculatory flux parameter measured with the TOPCam is the DC-normalized first moment of the power spectrum.

The CMOS camera also provides a black-and-white photograph from the same location as the perfusion image. The taken photograph visualizes a larger area than the measured area and indicates the measured area for orientation purposes afterwards.

The measurement control and signal processing are performed by LabView 8.5 (National Instruments). The range of the color scale of the perfusion images is set in such a way that the lowest and highest 0.5% values are not taken into account, to avoid the influence of some faulty pixels.

The commercial scanning beam LDPI system available in the Burn Centre of the Martini Hospital is a PeriScan PIM II System (Perimed AB, Sweden) with a class 2 laser with a maximum output power of 1 mW, a beam diameter of 1 mm and a wavelength of 670 nm. The system can measure up to 64×64

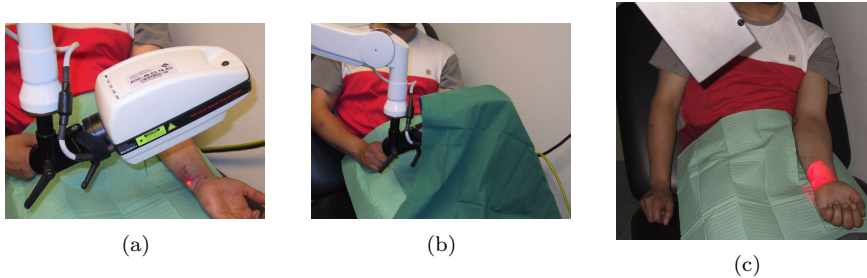


Figure 4.1: (a) The PIM II scan head is placed at 15 cm distance from the wound. Before starting the measurement the laser spot is placed on the middle of the wound, with the beam perpendicular to the wound surface. (b) A cloth covers the scan head of the PIM II, to shield the measurement from ambient light. (c) The TOPCam is placed at approximately 41 cm distance from the wound. The diffused light beam is projected on the wound with approximately perpendicular incidence.

measurement points in a maximum scan area of approximately $30 \times 30 \text{ cm}^2$. It has one photodetector to detect the backscattered light, the measured parameter was the DC-normalized first moment of the power spectrum, expressed in manufacturer specific Perfusion Units. The color scale of the perfusion images is set to a fixed minimum and maximum for interpretation by the physician. The limits of this scale are determined by earlier research about the perfusion values in different types of burns [8].

4.2.3 Clinical methodology

The TOPCam LDPI measurements and matching digital photos were all made by the first author. In the first days post burn, all wounds were treated with Flammacerium[®]; LDPI measurements were performed after cleaning the wound, prior to applying new cream and bandaging. The TOPCam imaging head was situated 41 cm above the wound surface, observing the wound as perpendicular as possible (see figure 4.1(c)). The spot size was set to $10 \times 10 \text{ cm}^2$ and a color photograph was taken with a digital camera for extra orientation purposes afterwards. The iris of the system was adjusted manually to have a maximum intensity of around 85-95% of the saturation level (displayed on the screen by the Labview program). During the measurements the room illumination was turned off and curtains or lamellas

4 Burn imaging with whole field LDPI based on a CMOS imaging array

were closed to minimize the influence of ambient light on the measurement. The patient was not shielded from the laser light and therefore was wearing special protecting glasses (Laser Vision, L5, 660-710nm).

The total measurement procedure resulted in an interruption of the nursing process for approximately 5-10 minutes, depending on the number of measured areas. On each site the measurements were made in quintuple to check the reproducibility of the results later. If the patient and the available time allowed, the wound was measured with the PIM II system as well (see figure 4.1(a) and (b)). Wounds with various etiologies were measured and if possible normal skin was included in the scanned area.

Besides showing that the system is able to measure perfusion differences in burn wounds, special attention was paid to wound appearances like blisters, dead overlapping skin and crusts. Although not the target group of LDPI systems, also measurements on full thickness burns were done to check if areas where no superficial perfusion is expected indeed do not show perfusion.

4.3 Results

In total 1023 laser Doppler perfusion images were made of 37 burn wounds of 23 patients (5 women, 18 men). The range of age was 16-66 years (mean: 37.1, sd: 15.2), the range of the total body surface area (TBSA) was 0.25-16% (mean: 4.6, sd: 4.2). The measurement series were done in the range of 1 - 21 days post burn (mean: 5, sd: 4.2). The etiology of the examined burns were fire/flash (13 patients), scald (9 patients) and contact (1 patient). The examined burns were located on the forearm (12), upper arm (6), lower leg (4), hand (4), foot (3), thorax (3), upper leg (3), buttock (1) and neck (1).

In this section a compilation of images of wound appearances like blisters, dead overlapping skin and crusts will be shown, providing a recapitulation of the most important findings.

4.3.1 Partial thickness burns

Figure 4.2(a) and (c) show typical images produced by the TOPCam. These are images of a partial thickness burn on the dorsal side of the right arm,



Figure 4.2: Partial thickness burn on the right arm around the elbow, day 2 pb. (a) Photograph taken by the TOPCam with the red box indicating the measured area. (b) Color photograph taken manually. (c) Perfusion image produced by the TOPCam.

around the elbow. The black-and-white photograph (figure 4.2(a)) is taken automatically by the TOPCam, the red box exactly indicates the perfusion image area. The color photograph shows a thin crust formed on the left side of the burn and dead skin on the right part. In the perfusion image (figure 4.2(c)) the dead skin is shown as a low perfusion area. The adjacent part with the crust indicates a higher perfusion, while the unaffected skin at the left upper corner has a measured perfusion level between that of the necrotic skin and the crust.

4.3.2 Blisters

In the burn centre in the Martini Hospital, blisters that do not impair joint movement or cause other problems, are kept intact for a maximum of five days. Figure 4.3 shows an example of perfusion images of a burn on the dorsum of a right hand with intact blister cap (figure 4.3(b)), and without the cap (figure 4.3(d)). Figure 4.3(b) shows higher perfusion values for the surrounding tissue than for the blister area. After removing the cap wound perfusion values at the cap positions were measured that are higher than the perfusion values of the surrounding unaffected tissue.

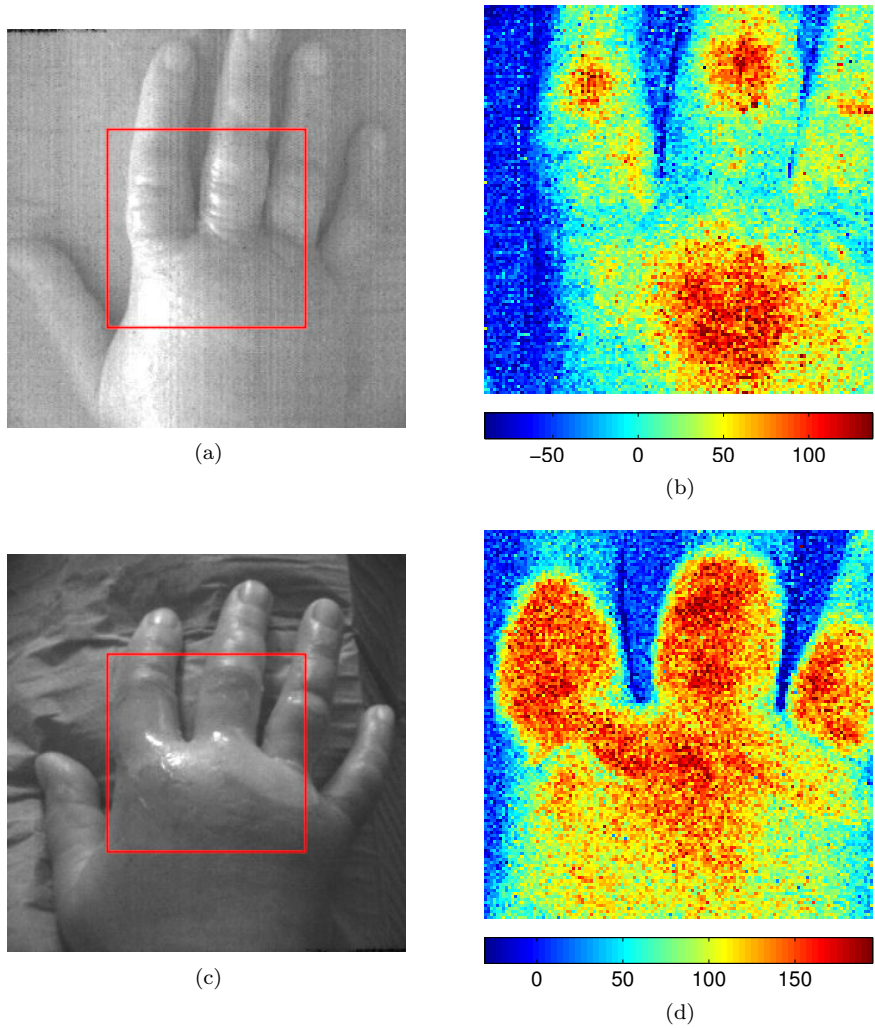


Figure 4.3: Partial thickness burn with blisters on the dorsal side of the hand, day 2 pb. (a) Photograph taken by the TOPCam before the blisters were removed. (b) Perfusion image before the blisters were removed. (c) Photograph taken by the TOPCam without the blister cap. (d) Perfusion image made after the blisters were removed.

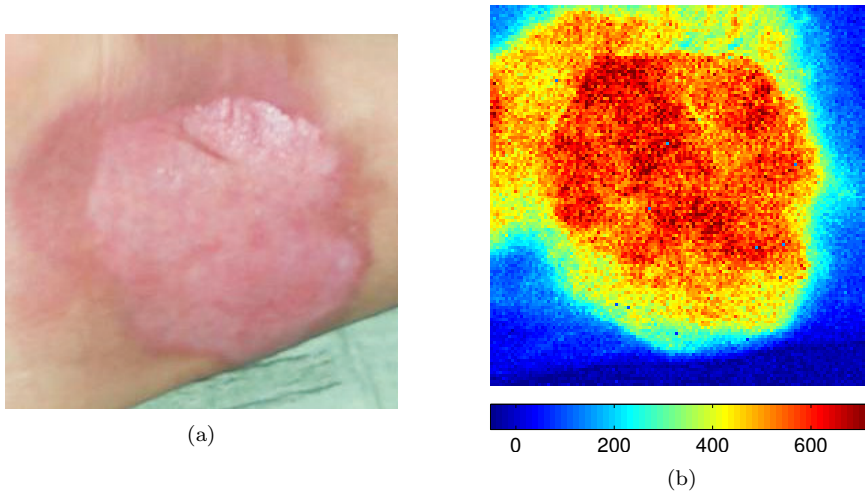


Figure 4.4: Partial thickness burn with dead skin layers on the edges. The wound was situated on the medial side of the left ankle, day 4 pb. (a) Color photograph taken manually. (b) Perfusion image.

4.3.3 Dead skin

Figure 4.2 showed a dark layer of dead skin on top of the burn, but also if the dead overlying skin looks less damaged, it influences the measurements. Figure 4.4 shows a measurement performed on a partial thickness burn on the left ankle. The blister cap was removed just before the measurement. However, on the edges not all dead skin was removed. The surrounding unaffected skin has lower perfusion values (i.e., blue) than the area where the superficial skin layer was removed. The affected edges where the dead layer not was removed shows higher perfusion values than the normal skin, but lower than the area in the centre of the wound.

4.3.4 Crusts

Flammacerium forms a crust on the wound, which impedes visual inspection and possibly also LDPI measurements [19, 20].

Figure 4.5 shows images of two crusts on the same patient. The perfusion

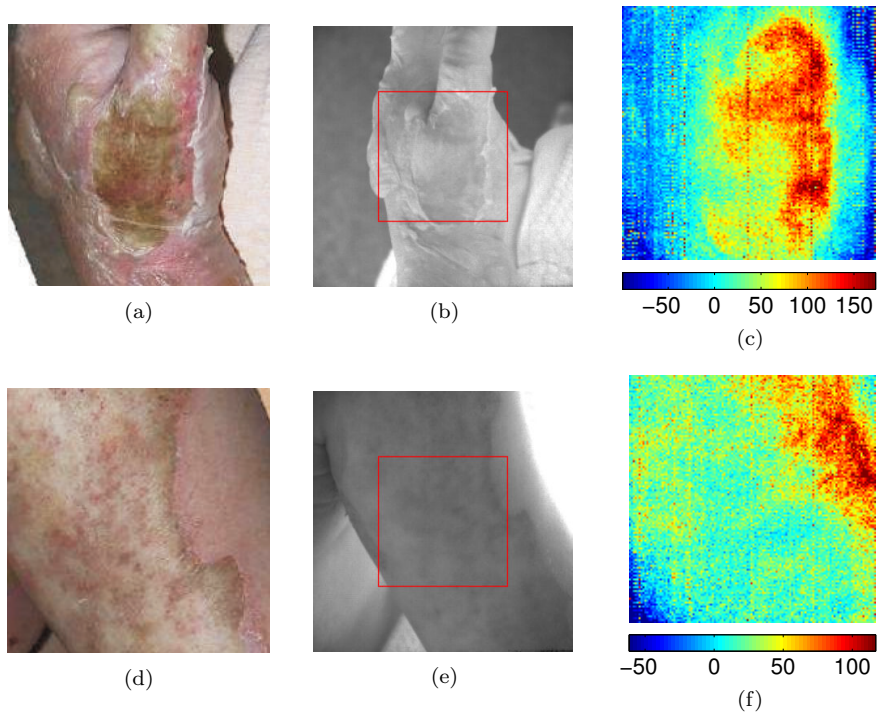


Figure 4.5: Partial thickness burn (2 days pb) with a crust on top. (a)-(c) Dorsal side of the left hand and (d)-(f) ventral side of the left upper arm. (a)&(d) Color photograph taken manually. (b)&(e) Photograph taken by the TOPCam. (c)&(f) Perfusion image.

image of the hand (figure 4.5(c)) shows on the right side an increased perfusion at the location of the crust. The perfusion image of the arm (figure 4.5(f)) shows no high perfusion at the crust location. The edge of the wound is well perfused, while the crust area shows the same lower perfusion values as the unaffected skin.

4.3.5 Comparison with the PIM II

To compare the TOPCam with a scanning beam imager, a partial thickness burn is imaged with both devices. Figure 4.6(a)-(c) shows the images ob-

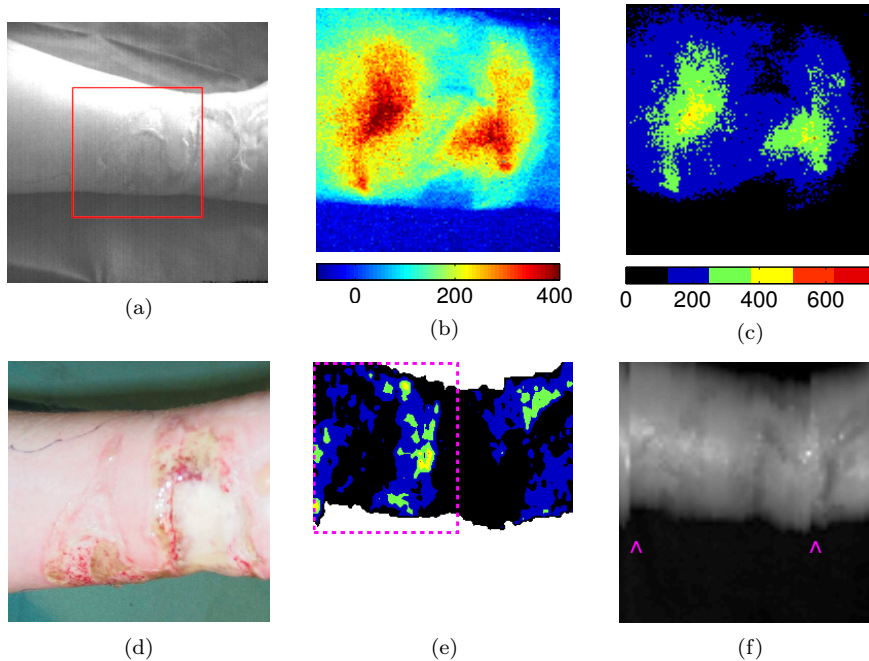


Figure 4.6: Full thickness burn on the ventral side of the left forearm, 2pb. The images are made with the TOPCam and the PIM II. (a) Photograph made by the TOPCam. (b) Perfusion image by the TOPCam displayed on the usual TOPCam scale. (c) Perfusion image by the TOPCam displayed on the PIM II six color scale with a fixed scale from 0 to 750. (d) Color photograph made manually. (e) PIM II perfusion image displayed on the PIM II six color scale with a fixed scale from 0 to 6.2 Perfusion Units. (f) PIM II DC image. The purple box in image (e) indicates the area measured with the TOPCam as well, the purple arrows in image (f) indicate two places where movement artefacts can be seen.

tained with the TOPCam, figure 4.6(e)-(f) with the PIM II system (color scale from 0 till 6.2 Perfusion Units). On the right side of the TOPCam image (figure 4.6(b)) a part of the full thickness burn was imaged and shows low perfusion values (lower than unaffected surrounding skin), as is expected for full thickness burn. The TOPCam perfusion image is presented on two different scales. The first one (figure 4.6(b)) is the color scale normally used with the TOPCam (i.e., 256 colors; blue to red; minimal and maximum values chosen to exclude the lowest and highest 0.5% values), whereas in

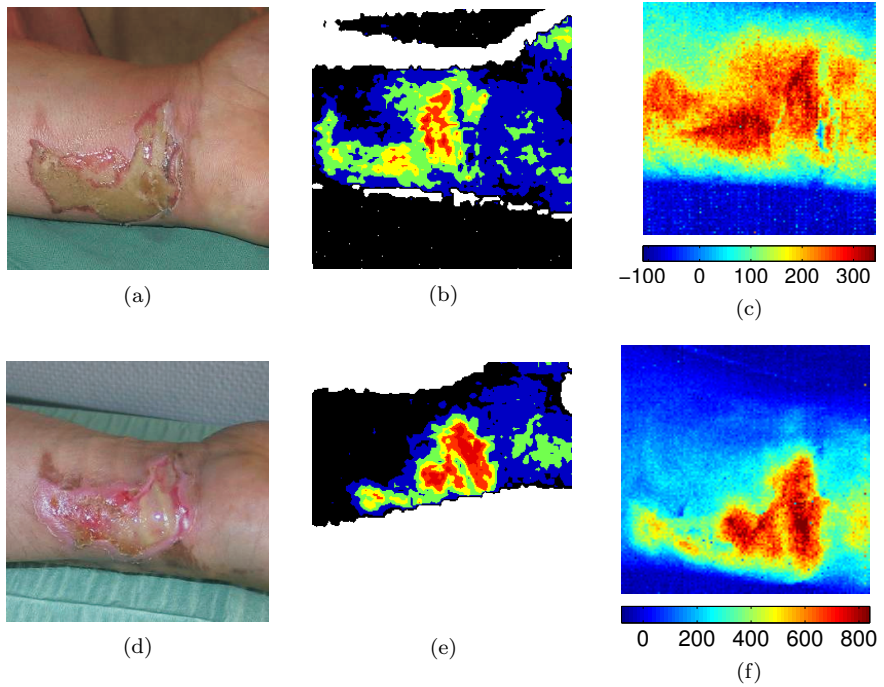


Figure 4.7: Partial thickness burn on the ventral side of the left forearm, (a) Color photograph made manually on day 2 pb (b) PIM II perfusion image on day 2pb displayed on the PIM II six color scale with a fixed scale from 0 to 6.2 Perfusion Units (c) TOPCam perfusion image on day 2 pb (d) Color photograph made manually on day 9 pb (e) PIM II perfusion image on day 9pb displayed on the PIM II six color scale with a fixed scale from 0 to 6.2 Perfusion Units (f) TOPCam perfusion image on day 9 pb.

figure 4.6(c) the scale is fixed from 0 to 750 (arbitrary chosen) and the color scale of the PIM II (i.e., 6 colors; black to red) is adopted to compare the TOPCam image with the PIM II image. In figure 4.6(e) the PIM II image is displayed with the fixed color scale that is normally used in the burn centre for interpretation of the images. The DC image (figure 4.6(f)) is the only orientation indication afterwards; the two arrows in this image indicate two places where movement artifacts show up. The purple lined box in figure 4.6(e) indicates the area that is imaged with the TOPCam.

Another example of a partial thickness burn wound that is imaged with

both systems is given in figure 4.7. The wound on the ventral side of the left wrist is imaged on day 2 and 9 days pb. The perfusion images of the PIM II system (figure 4.7(b) and (e)) and TOPCam (figure 4.7(c) and (f)) are displayed on their own color scale.

4.4 Discussion

4.4.1 General aspects

The results presented in this paper show the capability of the TOPCam to measure perfusion differences in burn wounds with various etiologies. Our results show high speed CMOS imaging technology, in combination with illumination of a large tissue area, is suitable for obtaining perfusion images of burn wounds.

The use of a high speed CMOS camera drastically reduces the measurement time with respect to a scanning beam device. This is a major advantage because it gives the opportunity to measure on patients for which a short measurement time is needed (e.g., young children) and who cannot be measured with a scanning beam device.

The perfusion images are all made with a illuminated tissue area of approximately $10 \times 10 \text{ cm}^2$. Due to the amount of curvature present in the human body, there is no need for increasing this size, except for measurements on the chest where a larger area can be favorable.

The figures also show the great advantage of taking a photograph of the wound with the same camera as was used for obtaining the perfusion image. In this way the black-and-white photo can be overlaid with the perfusion image for easy orientation afterwards. During some measurements the black-and-white photographs were under- or overexposed. Further adjustment of the software for automatic exposure time should solve this problem. Also the laser stability should be further improved; due to laser instability, clearly distinguishable excursions in the measured perfusion levels occurred, affecting the entire image.

4.4.2 Blisters

The measurements performed on blisters (figure 4.3) showed the troubles concerning the prediction of burn depth when a blister is present. The high perfusion that showed up in the wound after removing the blister cap (figure 4d) could possibly also be present while the cap is still on top. In that case, the system was not able to measure through the thick layer of blister fluid. Another possibility is that as a consequence of a biological reaction that took place after removal of the cap, the perfusion in the dermis below the blister, did suddenly increase.

4.4.3 Dead skin

The results of the measurements where dead skin was overlying a part of the wound (figure 4.4) suggest that the TOPCam can measure through dead skin, although dead skin influences the perfusion values. The open area of the wound in figure 4.4 shows higher perfusion than the covered wound area. It is doubtful that the covered wound edges are less likely to cure than the middle of the wound. The wound area underneath the dead skin in figure 4.2 did recover within two weeks without intervention. Therefore care should be taken when interpreting the perfusion images of wounds with overlying dead skin.

4.4.4 Crust

The low perfusion values on the left and right side of the perfusion image of the burn with a crust on top (figure 4.5(c)) are expected because on these parts of the hand still a layer of dead skin is present and the skin is also strongly curved which influences the measurement [10]. Due to this curvature it is not possible to include unaffected skin, which makes it harder to judge the measurement. However, this image shows that the system can measure enhanced perfusion at the area of the crust. Unfortunately without a reference it gives no clue if the perfusion measured in this wound is high enough for spontaneous healing within 2 weeks. The wound on the upper arm (figure 4.5(f)) shows perfusion values that are the same as the little part of normal skin included in the right top corner. A recovering wound should show higher perfusion values than normal skin. It is not totally

sure that the TOPCam was able to measure through the crust to measure the presence or absence of perfusion in the dermis. However, if increased perfusion indicates spontaneous healing within two weeks, it turned out that the images produced on day 2 pb (figure 4.5(f)) corresponded with the outcome in terms of healing capacity.

Because of the variations in time and space of the thickness and optical properties of the crust, more measurements should be performed to determine if the system can reproduce the correlation between perfusion image and burn depth in wounds with crusts on top. Perfusion readings through crust may either reflect the real perfusion value, the optical density of the crust, or both. There might be a relationship between the crust's optical density and the effect of Flammacerium on the underlying tissue. Additional research must reveal the significance of perfusion readings on crusts.

4.4.5 PIM II

Figure 4.6 and 4.7 show great similarity in the perfusion images made with the PIM II and TOPCam. However, figure 4.6 shows the possible influence of the color scale on the interpretation of the resulting images. The TOPCam used with the standard research settings (figure 4.6(b)) results in an image that suggests a better perspective than the PIM II system did (figure 4.6(e)). In the PIM II perfusion image both burned areas appear as black, whereas in the TOPCam image the obviously deep part is dark blue, while the other part is light blue and yellow. This difference is mainly caused by differences in color and scaling, as is illustrated in figure 4.6(b) and (c). Changing the color scale and its range and resolution influences the appearance of the image. Figure 4.6(c) shows that with changing the colors and the maxima and minima of the color scale, the perfusion images of the PIM II and TOPCam look the same.

In many cases, local experience in using LDPI in burn diagnosis is based on the use of a specific color scale, often chosen by the manufacturer. Newer generation LDPI imagers (e.g., the PIM III) use other color scales. If in the future a new system will be introduced in the burn centre, clinicians should have to put some effort in learning how to interpret these images.

If the future system will use a fixed scale as well, it is important to limit the variations in the iris adjustment. In the TOPCam, the iris of the system

has to be closed manually till the maximum intensity is at 95% of the saturation value of the camera. Especially with specularly reflecting surfaces the maximum intensity is fluctuating, making it impossible to adjust the iris exactly till the maximum intensity is 95%. Improper adjustment can influence the perfusion readings and therefore a fixed color scale would easily lead to misinterpretation of the perfusion images.

The images in figure 4.7 of both systems indicate good recovering capabilities of the wound, whereas at 9 days pb the wound is still open and wet. This illustrates there are always more factors (in this case probably an infection) that influence the recovery time of a wound.

The short measurement time of the TOPCam is a major advantage over the PIM II, as well as the opportunity to make a black-and-white photograph for easy orientation afterwards. Furthermore, Rajan *et al.* [21] have shown that in scanning beam imaging the perfusion readings are much stronger influenced by the optical properties of the tissue under investigation than in the whole field imaging strategy of the TOPCam and similar systems. The remaining influence of tissue optical properties is caused by their effect on the path length and penetration depth of the light. This may be overcome in future systems by an approach using low coherence light, as shown by Varghese *et al.* [22], which enables path length specific measurements.

4.5 Conclusion

In conclusion, we have shown that the TOPCam is able to measure perfusion differences in burn wounds. Several superficial partial thickness burns are imaged and, if increased perfusion indicates spontaneous healing within two weeks, showed good agreement with the outcome in terms of healing capacity. The measurements also indicate that the spatial image resolution of the TOPCam is sufficient for the diagnostic purposes in a burn centre.

Our whole field technique encounters similar problems as scanning beam LDPI devices for blisters, crusts, necrotic skin and skin curvature. However, the major increase in measurement speed removes one of the possible obstacles for the clinical acceptance of the technique.

References

1. D. M. Heimbach, M. A. Afromowitz, L. H. Engrav, J. A. Marvin & B. Perry (1984). "Burn depth estimation—man or machine". *Journal of Trauma*, **24**(5), 373–378.
2. S. A. Pape, C. A. Skouras & P. O. Byrne (2001). "An audit of the use of laser Doppler imaging (LDI) in the assessment of burns of intermediate depth". *Burns*, **27**, 233–239(7).
3. K. G. Grsu (1978). "An experimental study for diagnosis of burn depth". *Burns*, **4**(2), 97–103.
4. M. Godina, M. Derganc & A. Brcic (1978). "The reliability of clinical assessment of the depth of burns". *Burns*, **4**(2), 92–96.
5. B. Alsbjörn, J. Micheels & B. Sørensen (1984). "Laser Doppler flowmetry measurements of superficial dermal, deep dermal and subdermal burns". *Scandinavian Journal of plastic and reconstructive surgery*, **18**(1), 75–79.
6. Z. B. M. Niazi, T. J. H. Essex, R. Rapini, D. Scott, N. R. McLean & M. J. M. Black (1993). "New laser Doppler scanner, a valuable adjunct in burn depth assessment". *Burns*, **19**(6), 485–489.
7. E. K. Yeong, R. Mann, M. Goldberg, L. Engrav & D. Heimbach (1996). "Improved accuracy of burn wound assessment using laser Doppler". *Journal of Trauma*, **40**(6), 956–961.
8. F. W. Kloppenberg, G. I. Beerthuis & H. J. ten Duis (2001). "Perfusion of burn wounds assessed by laser Doppler imaging is related to burn depth and healing time." *Burns*, **27**, 359–363.
9. A. Mandal (2006). "Burn wound depth assessment – is laser Doppler imaging the best measurement tool available?" *International Wound Journal*, **3**(2), 138–144.
10. E. J. Droog, W. Steenbergen & F. Sjöberg (2001). "Measurement of depth of burns by laser Doppler perfusion imaging". *Burns*, **27**, 561–568.
11. C. L. Riordan, M. McDonough, J. M. Davidson, R. Corley, C. Perlov, R. Barton, J. Guy & L. B. Nanney (2003). "Noncontact laser Doppler

- imaging in burn depth analysis of the extremities”. *Journal of Burn Care & Research*, **24**(4), 177–186.
12. J. C. Jeng, A. Bridgeman, L. Shivnan, P. M. Thornton, H. Alam, T. J. Clarke, K. A. Jablonski & M. H. Jordan (2003). “Laser Doppler imaging determines need for excision and grafting in advance of clinical judgment: a prospective blinded trial”. *Burns*, **29**(7), 665–670.
 13. S. Monstrey, H. Hoeksema, J. Verbelen, A. Pirayesh & P. Blondeel (2008). “Assessment of burn depth and burn wound healing potential”. *Burns*, **34**(6), 761–769.
 14. H. Hoeksema, K. van de Sijpe, T. Tondu, M. Hamdi, K. van Landuyt, P. Blondeel & S. Monstrey (2009). “Accuracy of early burn depth assessment by laser Doppler imaging on different days post burn”. *Burns*, **35**(1), 36–45.
 15. C. J. Stewart, R. Frank, K. R. Forrester, J. Tulip, R. Lindsay & R. C. Bray (2005). “A comparison of two laser-based methods for determination of burn scar perfusion: Laser Doppler versus laser speckle imaging”. *Burns*, **31**, 744–752.
 16. A. Serov, W. Steenbergen & F. F. M. de Mul (2002). “Laser Doppler perfusion imaging with a complimentary metal oxide semiconductor image sensor”. *Optics Letters*, **27**(5), 300–302.
 17. A. Serov, B. Steinacher & T. Lasser (2005). “Full-field laser Doppler perfusion imaging and monitoring with an intelligent CMOS camera”. *Optics Express*, **13**(10), 3681–3689.
 18. M. J. Draijer, E. Hondebrink, T. G. van Leeuwen & W. Steenbergen (2009). “The Twente Optical Perfusion Camera: system overview and performance for real time laser Doppler perfusion imaging”. *Optics Express*, **17**(5), 3211–3225.
 19. J. P. Garnera & P. S. J. Heppell (2005). “Cerium nitrate in the management of burns”. *Burns*, **31**(5), 539–547.
 20. D. Ng, S. Tay, S. Booth, P. Gilbert & B. Dheansa (2007). “The use of laser Doppler imaging for burn depth assessment after application of flammacerium”. *Burns*, **33**(3), 396–397.

21. V. Rajan, B. Varghese, T. G. van Leeuwen & W. Steenbergen (2008). “Influence of tissue optical properties on laser Doppler perfusion imaging, accounting for photon penetration depth and the laser speckle phenomenon”. *Journal of Biomedical Optics*, **13**(2), 024001.
22. B. Varghese, V. Rajan, T. G. van Leeuwen & W. Steenbergen (2007). “Path-length-resolved optical Doppler perfusion monitoring”. *Journal of Biomedical Optics*, **12**(6), 060508.

5

Time domain algorithm for accelerated determination of the first order moment of photo current fluctuations in high speed laser Doppler perfusion imaging

This chapter has been published as : M.J. Draijer, E. Hondebrink, T.G. van Leeuwen, and W. Steenbergen (2009) "Time domain algorithm for accelerated determination of the first order moment of photo current fluctuations in high speed laser Doppler perfusion imaging", *Medical & Biological Engineering & Computing*, **47**(10), 1103–1109.

Abstract – Advances in optical array sensor technology allow for the real time acquisition of dynamic laser speckle patterns generated by tissue perfusion, which in principle allows for real time laser Doppler perfusion imaging (LDPI). Exploitation of these developments is enhanced with the introduction of faster algorithms to transform photo currents into perfusion estimates using the first moment of the power spectrum.

A time domain (TD) algorithm is presented for determining the first order spectral moment. Experiments are performed to compare this algorithm with the widely used *Fast Fourier Transform* (FFT). This study shows that the TD-algorithm is twice as fast as the FFT-algorithm without loss of accuracy.

Compared to FFT, the TD-algorithm is efficient in terms of processor time, memory usage and data transport.

5.1 Introduction

Laser Doppler perfusion imaging (LDPI) [1–8] and related techniques like laser speckle contrast analysis (LASCA) [3, 4, 6, 9–13] and laser speckle imaging (LSI) [14, 15] are established techniques for determining skin perfusion maps, for instance to diagnose burns [6, 16–18] or diabetic ulcers [19], to study cerebral blood flow in humans [20] and small animals [21–23], and for drug uptake studies (e.g. using iontophoresis) [24].

In LDPI the skin is illuminated with coherent laser light. A fraction of the laser light that entered the tissue, interacts with moving red blood cells and obtains a Doppler shift. When these photons leave the tissue they interfere on the detector with each other and with light which has not obtained a Doppler shift, resulting in a time fluctuating signal. The moments of the

power spectrum $S(\omega)$ of this photoelectric current are given by :

$$M_i \propto \int_0^{\infty} \omega^i S(\omega) d\omega \quad (5.1)$$

In LDPI the zeroth order moment ($i = 0$) is a measure for the concentration of red blood cells whereas the first order moment ($i = 1$) is a measure for the flux or perfusion.

In commercially available LDPI devices the area under investigation is scanned with a narrow laser beam. Signal processing of the photoelectric current is performed by analog frequency-weighted filters. Using beam scanning, a perfusion image of 256×256 takes approximately 5 minutes. This long scanning time impedes the observation of fast perfusion changes, for instance during reperfusion after occlusion. To obtain real-time reperfusion images a refresh rate of approximately 25 Hz is needed. Also for the patient a short imaging time is desirable (e.g for burn patients, and in general for young children and elder patients). The need for reduced imaging time is solved by the introduction of CMOS imaging arrays in the field of LDPI [5, 25–27]. This ascent in optical array sensor technology allowed the real time acquisition of dynamic laser speckle patterns generated by the tissue perfusion, which in principle allows real time LDPI. Recently it is shown the relation between the first moment and tissue blood perfusion still hold for the full-field illumination scheme [27].

To take advantage of these developments the conversion of measured photo current fluctuations into perfusion estimates should be as efficient as possible. A straightforward way to calculate the perfusion in LDPI with a CMOS-camera is by making use of the Fast Fourier Transform (FFT) to calculate the power spectral density (PSD) followed by a weighted integration of the PSD over all frequencies. Calculating the perfusion using the FFT is time consuming because it has to be taken for each pixel and the spectrum has to be squared and integrated over all frequencies to obtain one number for the perfusion. Obtaining a perfusion image of 256×256 pixels takes up to 10 seconds on a personal computer with a 3.2 GHz Pentium 4 processor and 1.0 Gb RAM-memory.

Here we present and evaluate a calculation algorithm for the first order moment working in the time domain (referred to as TD) which involves less computational steps and requires less data to be transported and stored.

The term 'time domain' refers to the fact that the perfusion parameter is determined from the time series of photo current fluctuations, without the need to perform a mathematical transformation of this time series, such as a Fourier transform.

5.2 Method

5.2.1 Theory

Koelink et al. [28] described a time domain algorithm that estimates the first order moment of the photo detector current power spectrum via the second order moment. For that, the assumption was made that the power spectrum is exponentially shaped. In our approach we directly estimate the first order moment of the power spectrum.

The convolution property states that the Fourier transform of the product of two functions is the convolution of the Fourier transform of these functions :

$$\int_{-\infty}^{\infty} g(t)h(t) \exp(-i\beta t)dt = \frac{1}{2\pi} \int_{-\infty}^{\infty} G(\omega)H(\beta - \omega)d\omega \quad (5.2)$$

with $G(\omega)$ and $H(\omega)$ being the Fourier transform of $g(t)$ and $h(t)$ respectively. For $\beta = 0$ this becomes :

$$\int_{-\infty}^{\infty} g(t)h(t)dt = \frac{1}{2\pi} \int_{-\infty}^{\infty} G(\omega)H(-\omega)d\omega \quad (5.3)$$

Taking the time derivative in the time domain corresponds with multiplication with $i\omega$ in the frequency domain :

$$\frac{\partial^n}{\partial t^n} f(t) \rightarrow (i\omega)^n F(\omega) \quad (5.4)$$

So introducing $h(t) = \frac{\partial}{\partial t} g^*(t)$ and applying the property that the Fourier transform of $g^*(t)$ equals $G^*(-\omega)$, equation 5.3 reduces to:

$$\left\langle g(t) \frac{\partial}{\partial t} g^*(t) \right\rangle = \frac{1}{2\pi} \int_{-\infty}^{\infty} i\omega G(\omega)G^*(\omega)d\omega \quad (5.5)$$

We introduce the real signal $f(t)$ (i.e., $f^*(t) = f(t)$) and amplitude spectrum $A(\omega)$, which are a Fourier pair :

$$f(t) = \frac{1}{2\pi} \int_{-\infty}^{\infty} A(\omega) \exp(i\omega t) d\omega \quad (5.6)$$

as well as the power spectrum $S(\omega)$ of $f(t)$ which is defined as:

$$S(\omega) \equiv |A(\omega)|^2 = A^*(\omega)A(\omega) \quad (5.7)$$

Equation 5.5 can then be written as :

$$\left\langle f(t) \frac{\partial}{\partial t} f(t) \right\rangle = \frac{1}{2\pi} \int_{-\infty}^{\infty} i\omega S(\omega) d\omega \quad (5.8)$$

Because $i\omega S(\omega)$ is an anti-symmetric function, taking the integral from $-\infty$ to ∞ will result in a right hand side of equation 5.8 equal to 0. It can also be proven that for a statistically stationary function $f(t)$, the left hand side of equation 5.8 equals zero [29]. Hence, although correct, equation 5.8 is not useful for our purposes. However, in the field of LDPI the first moment is originally defined as [1] :

$$M_1 \equiv \int_{-\infty}^{\infty} |\omega| S(\omega) d\omega \quad (5.9)$$

In equation 5.8, the right hand side being zero is the result of a balance between the integrals from $-\infty$ to zero and zero to ∞ . Replacing $i\omega$ with $|\omega|$ on the right hand side of equation 5.8 makes the right hand side unequal to zero, and equal to M_1 as defined by equation 5.9. Equally, we can break the balance in the left hand side of equation 5.8 by replacing it with the time average of $\left| f \frac{\partial f}{\partial t} \right|$. Next, we assume that the equal but opposite parts which cancel both the right and left sides of equation 5.8, are equal to each other. This is still a mainly intuitive step, which mathematical justification is being searched for. However, it is a tempting step leading to :

$$M_1 \approx 2\pi \left\langle \left| f(t) \frac{\partial f(t)}{\partial t} \right| \right\rangle \quad (5.10)$$

We emphasize that equation 5.10 will probably provide an approximation of the first order moment as defined by equation 5.9 rather than being an exact

5 Time domain algorithm for accelerated determination of perfusion in high speed LDPI

result of straightforward mathematics. Hence, for calculating the first order moment of the power spectrum, we can reduce the number of computational steps in comparison with the FFT-based method : equation 5.10 shows that the first order moment can be estimated from the fluctuating part of the photocurrent signal and its time derivative. Since

$$\left| f(t) \frac{\partial f(t)}{\partial t} \right| = \text{sign} \left(f(t) \frac{\partial f(t)}{\partial t} \right) f(t) \frac{\partial f(t)}{\partial t}$$

mathematical justification of equation 5.10 may be found by studying the spectral properties of $\text{sign} \left(f(t) \frac{\partial f(t)}{\partial t} \right)$. In our future research we will investigate the mathematical justification of equation 5.10 along this line.

5.2.2 Materials

When the light intensity fluctuations are digitally recorded, the input signal $f(t)$ is converted into a discrete signal consisting of samples f_i . Equation 5.10 can be discretized as

$$M_1 = \frac{2\pi\nu_s}{N} \sum_{i=0}^{N-1} |f_i (f_{i+1} - f_i)| \quad (5.11)$$

with ν_s the sample frequency, f_i the i^{th} sample of f and N the total number of samples of f . Trials were performed with various discretisations of equation 5.11. Taking the time derivative with f_{i-1} and f_i or f_i and f_{i+1} gave comparable results.

Equation 5.10 and its discretization in equation 5.11 represent the TD-algorithm and give an expression for the first order moment of $S(\omega)$ in terms of the samples of f . So using the TD-algorithm gives the opportunity to determine the perfusion with some simple mathematical operations in the time domain which do not require large computational power or time.

To test the accuracy of the TD-algorithm, several scattering objects were imaged with a homebuilt laser Doppler perfusion imager (LDPI) using a 10 bits CMOS-camera and a 300 mW laser emitting at 671 nm to illuminate an area of approximately 10×10 centimeters. This setup is described in detail in reference [27]. 1024 images of 128×128 pixels were obtained at a frame rate of 27 kHz, resulting in 16384 raw time traces of 1024 samples each.

Afterwards DC-subtraction (i.e. subtracting the mean value) was applied to focus on fluctuations in the comparison rather than on the mean value. Without this subtraction the outcome of the TD-algorithm would mainly be determined by the offset introduced by the DC-value rather than by the fluctuations.

The first sample consisted of a cylindrical piece of Delrin of 40 mm in diameter with a hole of 4 mm in diameter filled with *IntraLipid 20%* (Fresenius Kabi) and placed on green surgery paper. The second comparison was performed on human tissue. The ring and little fingers of the right hand of a volunteer (male, 26 yr), positioned on a black cloth, were imaged. The last comparison was performed during an occlusion and the reperfusion afterwards [30]. The occlusion was applied by inflating a blood pressure cuff around the upper arm of a healthy subject (male, 27 yr). The measurement on the wrist was started 3 minutes after the occlusion was applied. Approximately 5 seconds after the start of the measurement the occlusion was released. The data was afterwards processed with both algorithms. For every perfusion image of 128×32 pixels the average value was determined based in the complete image and plotted as a function of time.

Based on these time traces the first order spectral moment was calculated with the TD-algorithm and FFT-algorithm. For the FFT-algorithm we integrated over all frequencies present in the signal, so from 0 till 13.5 kHz. Calculations were performed using Labview 7.1 (National Instruments) and Matlab 7.2 (the MathWorks) on a personal computer with a 3.2 GHz Pentium 4 processor and 1.0 Gb RAM-memory. For comparison a scatter plot is made in which the value obtained with the FFT-algorithm is plotted as a function of the value obtained with the TD-algorithm, as well as a linear fit through these values (solid line) and its 95% confidence interval. As guidance to the eye the line $\text{FFT} = \text{TD}$ (dotted line) is drawn and the correlation coefficient (r) is given. This allows to analyse the correlation between the two estimates.

Furthermore, the two algorithms are compared using the Bland-Altman method [31, 32]. This involves plotting the difference of the values obtained with the two methods versus their average value. The black solid line in the Bland-Altman plot indicates the mean difference and the dashed lines indicate the mean plus and minus twice the standard deviation of the difference between the estimates. When the points are normally distributed, 95% of all points lays between these two dashed lines. To visualize the trend in the data, the data is divided into horizontal bins with a size of 1000. In these

5 Time domain algorithm for accelerated determination of perfusion in high speed LDPI

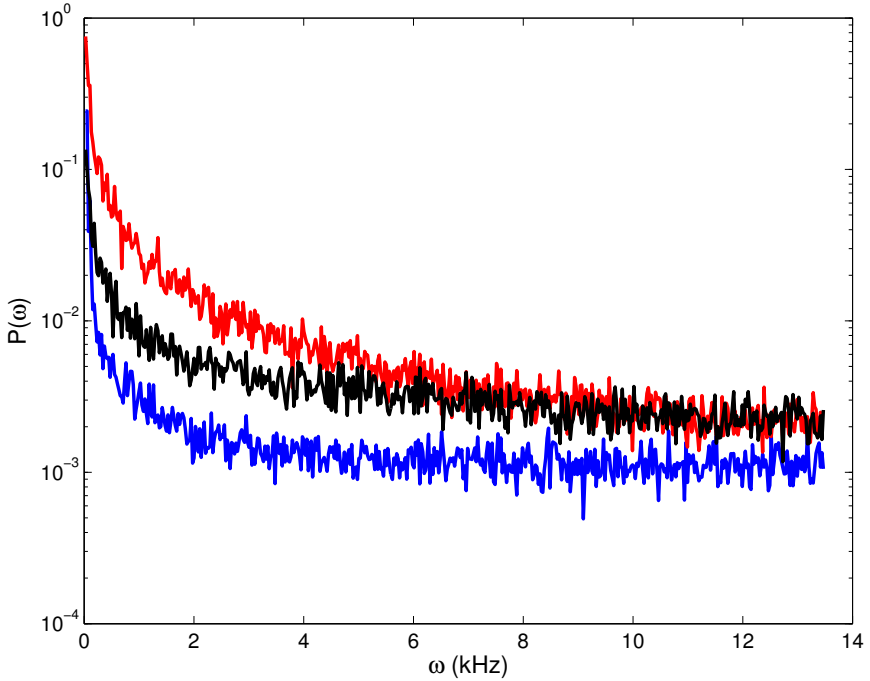


Figure 5.1: The power spectra of Delrin (blue line), Intralipid (red line) and human tissue (black line) averaged over an area of 5×5 pixels.

bins the mean value is determined and plotted (red line).

Each point in the scatterplot as well as in the Bland-Altman-plot corresponds with the analysis of the time trace of one pixel.

To compare both algorithms with respect to calculation time, the time needed to calculate the perfusion for an image of 256×256 pixels for different lengths of the time signal was measured for both algorithms using MatLAB and LabVIEW.

5.3 Results

To give an impression of the variation in spectral content included in our measurements, three types of power spectra are shown in figure 5.1. The spectra have been obtained in regions of 5×5 pixels, situated in the image of the Delrin part of the first object, the Intralipid part of the first object, and the tip of the finger.

For the cylindrical Delrin sample containing some Intralipid, the resulting images of the first order moments with FFT and TD algorithms, as well as the scatter plot of FFT-results versus TD-results and Bland-Altman plot are shown in figure 5.2(a)-(d), respectively. The slope of the linear fit of the scatter plot is 0.8229 with a 95% confidence interval of [0.8221 0.8238].

The results obtained from the hand of the volunteer are shown in figure 5.3. The slope of the linear fit in the scatter plot is 1.1319 with a 95% confidence interval of [1.1314 1.1324].

Figure 5.4 shows the perfusion during an occlusion and reperfusion calculated with the FFT-algorithm (black line) and TD-algorithm (red line).

The calculation time with both algorithms using MatLAB and LabVIEW as function of the number of raw speckle images involved in the calculation of the spectral first moment, is shown in figure 5.5 along with the calculation time as reported by Serov et al. using the FFT-approach [25].

5.4 Discussion

5.4.1 Comparison of both algorithms

The spectra in figure 5.1 show that static Delrin causes the least broadening, while Intralipid shows the highest spectral broadening, as must be expected. Figure 5.1 gives an impression of the large variety of spectral shapes in the data sets which are used to compare the TD and FFT algorithms.

As is shown in figure 5.2 and 5.3 the perfusion maps for the several measured samples differ slightly between both algorithms. The scatter plots for the perfusion (figure 5.2(c) and 5.3(c)) show a narrow cloud instead of a straight

5 Time domain algorithm for accelerated determination of perfusion in high speed LDPI

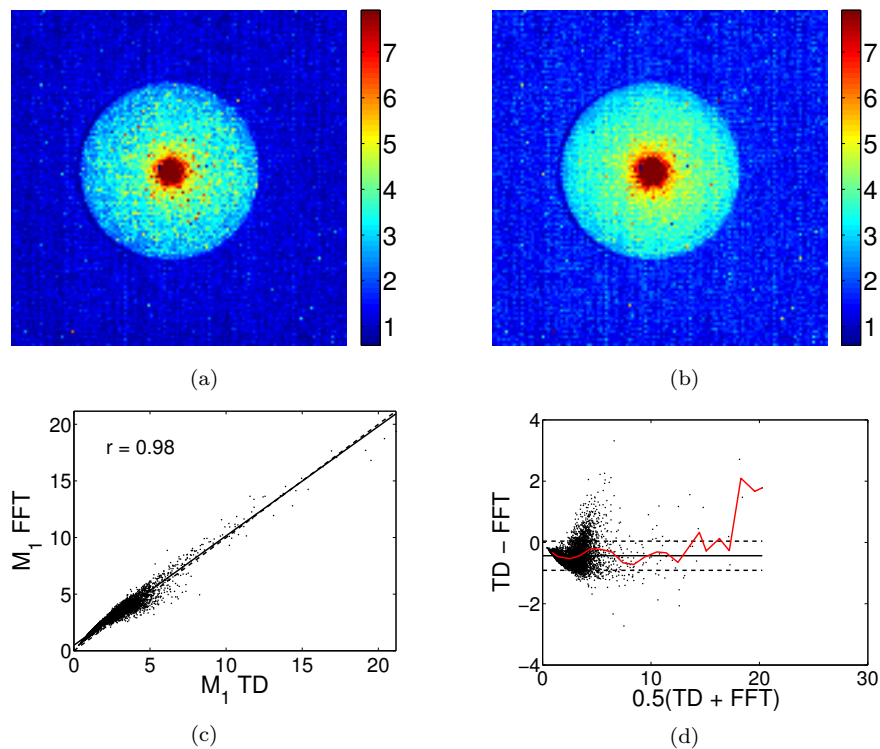


Figure 5.2: 128×128 pixel images of the perfusion obtained from a cylindrical piece of Delrin of 40 mm in diameter with a hole of 4 mm in diameter and placed on green surgery paper, the hole was filled with *IntraLipid 20%* (imaged area approx. 7×7 cm). Perfusion plots with (a) the TD-algorithm, (b) the FFT-algorithm and (c) scatter plot of FFT-results versus TD-results (solid line: linear fit; dashed line: $TD=FFT$) and (d) Bland-Altman plot of both perfusion plots, the red line indicates the average value of $TD-FFT$ over horizontal intervals of 1000.

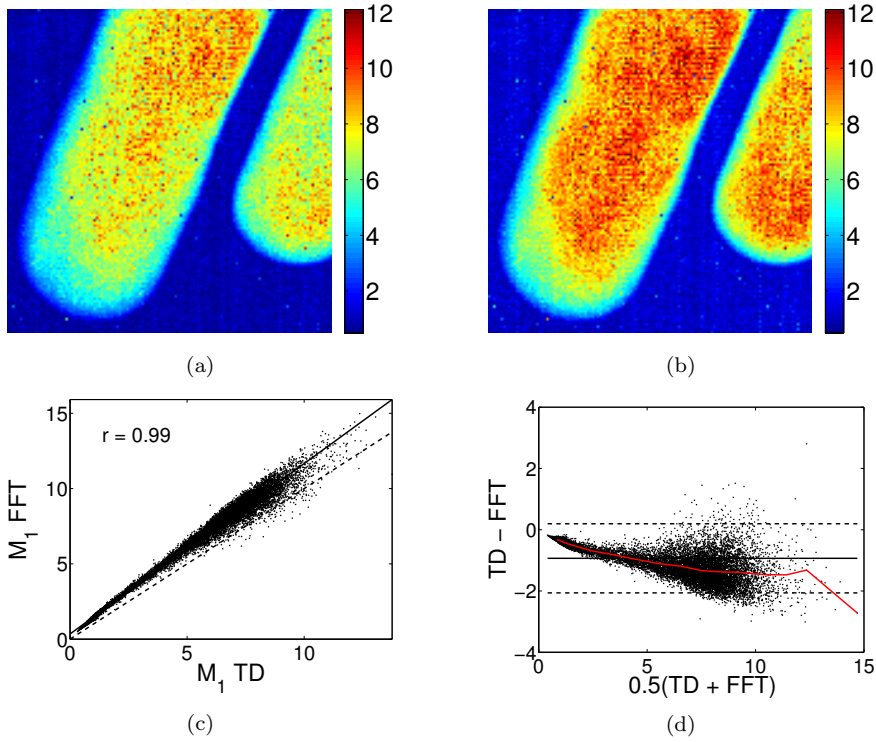


Figure 5.3: 128×128 pixel images of the perfusion of the finger tips of the hand of a volunteer (imaged area approx. 4×4 cm).

(a) perfusion plot with the TD-algorithm, (b) perfusion plot with the FFT-algorithm and (c) the scatter plot of FFT-results versus TD-results (solid line: linear fit; dashed line: TD=FFT) and (d) Bland-Altman plot of both perfusion plots, the red line indicates the average value of TD-FFT over horizontal intervals of 1000.

line indicating there is some difference between the TD-algorithm and the FFT-algorithm. This difference can also be seen in the Bland-Altman plots (figure 5.2(d) and 5.3(d)) where there is a deviation from the black solid line (i.e. the mean difference) and the cloud is not equally distributed around the solid line. The differences in the perfusion images seem largest for the images of skin perfusion (figure 5.3). However, this is mainly a visual effect due to the large color differences within the range of image values. A more quantitative comparison is given by the scatter plots and Bland-Altman plots.

5 Time domain algorithm for accelerated determination of perfusion in high speed LDPI

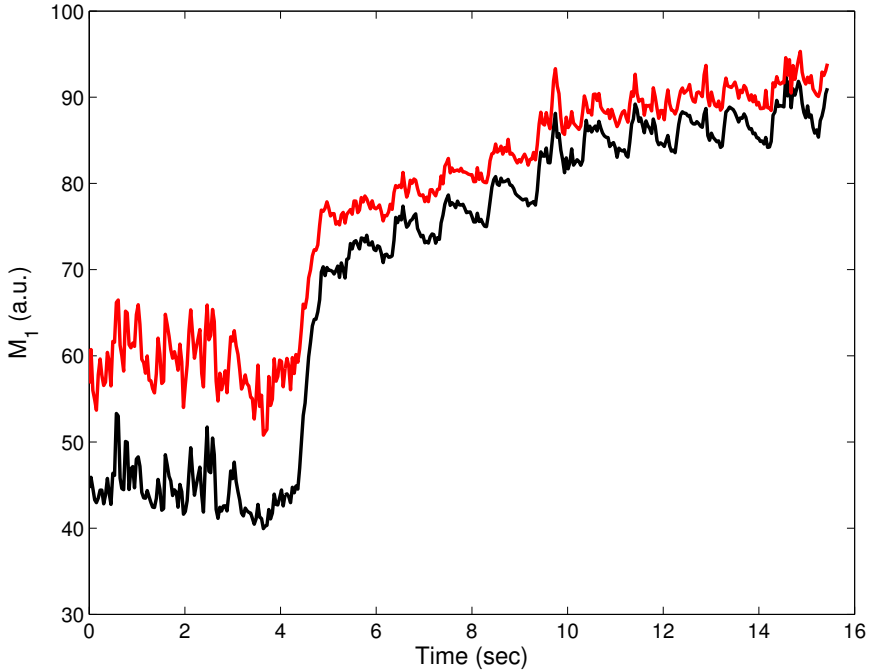


Figure 5.4: Perfusion as a function of time during occlusion and reperfusion calculated with the FFT-algorithm (black line) and the TD-algorithm (red line).

The agreement between TD and FFT in terms of absence of random variations, is best for the first order moment values obtained in static regions, hence on cloth material and Delrin. In these regions, first order moments are found in the interval between 0 and 2.5, where the scatter plots show relatively small random variations compared to the first order moments exceeding values of 2.5. In these regions, the perfusion image is largely caused by noise in the photo current. In this case the signal is more evenly spread in the spectral domain than signals caused by Brownian motion or real perfusion. This suggests that the TD-signal can deal better with high- than low frequency signal components. This difference can have several reasons, a possible source of error in the TD-results is the discretisation applied in this algorithm.

In spite of the differences between the TD and the FFT-algorithm as ob-

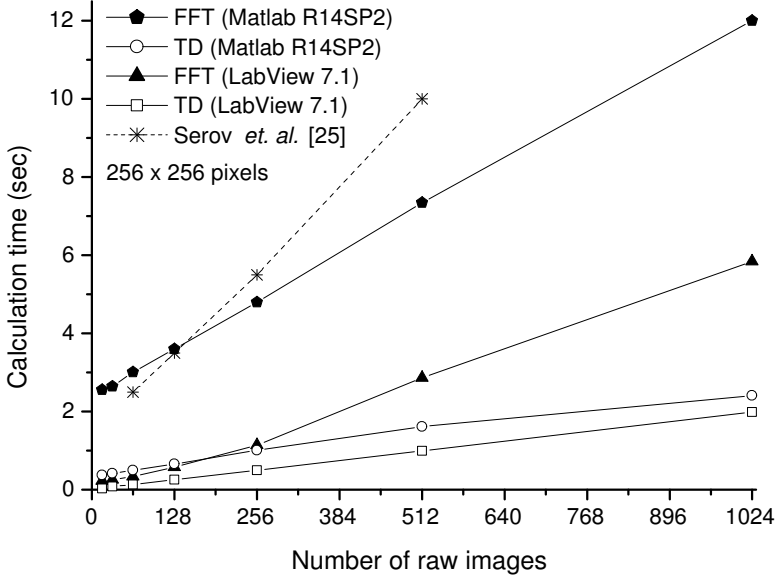


Figure 5.5: Calculation time for the TD-algorithm and the FFT-algorithm for an image of 256×256 pixels for two software packages, as a function of the number of raw images.

served in the scatter plots, the perfusion images obtained with both methods are similar. This similarity can be shown in two ways. First, when a ROI is selected on the finger in figure 5.3(a) and 5.3(b) (not shown), the standard deviation within these two ROIs is between the 10% and 15%. This is in the same order as the difference between the values of the two ROIs. So the difference between the TD and the FFT-algorithm can largely be explained based on statistical grounds. Secondly, the average curve in the BA plots (red line), shows that the systematic difference between TD and FFT is approximately 15%. Note that the large excursions of the mean difference for high image values are in those regions where only a few values contribute to the BA-plots. This is also in the same order as the standard deviation within the two ROIs. So both methods give similar results and will lead to the same judgment by the physician. Clinical judgment will be based not

5 Time domain algorithm for accelerated determination of perfusion in high speed LDPI

on separate pixel values, but on the perfusion in a larger tissue area. So the difference between the FFT-algorithm and the TD-algorithm can be seen as noise superimposed on the image plus a systematic difference of maximal 15%. The interpretation by the physician will not be influenced by the difference between the perfusion maps.

The small difference between the TD-algorithm and the FFT-algorithm is also visible in the comparison of both algorithms during the occlusion-reperfusion procedure (figure 5.4). With both algorithms the heart beat is nicely visible after release of the occlusion. The average time between the heart beat peaks is 920 milliseconds, which corresponds with the heart beat frequency of 65 beats per minute. In the reperfusion stage an offset is visible of less than 5%. For low perfusion levels (i.e. during the occlusion) this offset has increased.

In contrast to LDPI, the lower integration limit for the FFT-algorithm was set to 0 Hz, which implies that all frequencies are taken into account and both algorithms should be equal sensitive to low frequencies. Noise correction was not applied in both algorithms. This explains why in both algorithms perfusion is still visible during the occlusion.

5.4.2 Calculation speed

As is shown in figure 5.5 the TD-algorithm is at least twice as fast as the FFT-algorithm, so the TD-algorithm is a good alternative for the FFT-algorithm in laser Doppler perfusion imaging. The more raw images are taken into account, the bigger the saving of time is. Tests (out of the scope of this article so not shown) to determine the accuracy of the calculated perfusion level as a function of the number of raw images, reveal that at least 512 images, but preferably more, should be taken into account to obtain a proper perfusion image.

5.4.3 Implementing TD on high speed CMOS-cameras

CMOS-cameras which are equipped with a programmable memory for data acquisition can implement the discretized version of the TD-algorithm easily which brings (semi-)real time perfusion imaging within reach. Memory requirements are low, since the TD-algorithm only needs two raw frames

for obtaining a preliminary perfusion plot. Every new raw frame can then be used for producing a new perfusion plot by combining it in a weighted way with the previous perfusion plot and the previous raw frame. In this way, the perfusion map will converge to a statistically accurate value, and a perfusion value update can be performed when a new frame is available. In this way perfusion variations in time can be followed with minimum transport and data storage. The memory requirements are slightly increased by the fact that in practice the raw signal must be high pass filtered to suppress the influence of signal artifacts which often occur at frequencies below 20 Hz. One way of implementing high-pass filtering in time-domain is by making use of spectral inversion [33]. In this technique the low-pass filtered signal obtained by a moving average filter is subtracted from the unfiltered signal. Since the low frequency components are subtracted from the original signal, only the high frequency components appear in the output and the signal is high-pass filtered. When spectral inversion is implemented in a moving way it can be incorporated in the TD-algorithm. The use of a moving average approach implies that the number of frames to be stored in memory is larger than two, but still much lower than the amount needed to perform a complete Fast Fourier Transform. In this way low frequencies can be filtered out, although it will probably not be as good as high-pass filtering in the FFT-algorithm. This means that the time-domain algorithm is possibly more sensitive to low frequencies in the power spectrum, caused for instance by heart-beat related rhythmic blood volume variations (the photoplethysmographic signal) [34] or motion artifacts.

5.5 Conclusion

In conclusion, we have shown that the TD-algorithm can be a good alternative for the FFT-algorithm. The TD-algorithm provides a suitable approximation of the first order moment rather than being an estimator based on a rigorous mathematical analysis. The new algorithm can determine the perfusion in LDPI twice as fast as the FFT-algorithm and gives equivalent perfusion images. Furthermore the TD-algorithm gives the possibility to perform on-the-fly estimation because it only needs a few new frames to update a previous perfusion estimation. This results in lower memory requirements compared to the memory needed to perform an FFT, which is a major advantage of the TD-algorithm.

References

1. R. Bonner & R. Nossal (1981). “Model for laser Doppler measurements of blood flow in tissue”. *Applied Optics*, **20**(12), 2097–2107.
2. Y. Aizu & T. Asakura (1991). “Bio-speckle phenomena and their application to the evaluation of blood flow”. *Optics & Laser Technology*, **23**(4), 205–219.
3. J. D. Briers (1996). “Laser Doppler and time-varying speckle: A reconciliation”. *Journal of The Optical Society of America, A*, **13**(2), 345–350.
4. J. D. Briers (2001). “Laser Doppler, speckle and related techniques for blood perfusion mapping and imaging”. *Physiological Measurements*, **22**, R35–R66.
5. A. Serov, W. Steenbergen & F. F. M. de Mul (2002). “Laser Doppler perfusion imaging with a complimentary metal oxide semiconductor image sensor”. *Optics Letters*, **27**(5), 300–302.
6. C. J. Stewart, R. Frank, K. R. Forrester, J. Tulip, R. Lindsay & R. C. Bray (2005). “A comparison of two laser-based methods for determination of burn scar perfusion: Laser Doppler versus laser speckle imaging”. *Burns*, **31**, 744–752.
7. A. Humeau, W. Steenbergen, H. Nilsson & T. Strömberg (2007). “Laser Doppler perfusion monitoring and imaging: novel approaches”. *Medical & Biological Engineering & Computing*, **45**, 421–435.
8. V. Rajan, B. Varghese, T. G. van Leeuwen & W. Steenbergen (2008). “Review of methodological developments in laser Doppler flowmetry”. *Lasers in Medical Science*.
9. A. F. Fercher & J. D. Briers (1981). “Flow visualization by means of single-exposure speckle photography”. *Optics Communications*, **37**(5), 326–330.
10. H. Fujii (1994). “Visualisation of retinal blood flow by laser speckle flowgraphy”. *Medical & Biological Engineering & Computing*, **32**, 302–304.
11. J. D. Briers, G. Richards & X. W. He (1999). “Capillary blood flow monitoring using laser speckle contrast analysis (LASCA)”. *Journal of Biomedical Optics*, **4**(1), 164–175.

12. K. R. Forrester, C. Stewart, J. Tulip, C. Leonard & R. C. Bray (2002). "Comparison of laser speckle and laser Doppler perfusion imaging : measurement in human skin and rabbit articular tissue". *Medical & Biological Engineering & Computing*, **40**, 687–697.
13. M. J. Draijer, E. Hondebrink, T. G. van Leeuwen & W. Steenbergen (2009). "Review of laser speckle contrast techniques for visualizing tissue perfusion". *Lasers in Medical Science*, **24**(4), 639–651.
14. H. Cheng, Q. Luo, S. Zeng, S. Chen, J. Cen & H. Gong (2003). "Modified laser speckle imaging method with improved spatial resolution." *Journal of Biomedical Optics*, **8**(3), 559–564.
15. S. K. Nadkarni, B. E. Bouma, T. Helg, R. Chan, E. Halpern, A. Chau, M. S. Minsky, J. T. Motz, S. L. Houser & G. J. Tearney (2005). "Characterization of atherosclerotic plaques by laser speckle imaging". *Circulation*, **112**, 885–892.
16. R. Bray, K. Forrester, C. Leonard, R. McArthur, J. Tulip & R. Lindsay (2003). "Laser Doppler imaging of burn scars: A comparison of wavelength and scanning methods". *Burns*, **29**(3), 199–206.
17. E. La Hei, A. Holland & H. Martin (2006). "Laser Doppler imaging of paediatric burns: Burn wound outcome can be predicted independent of clinical examination". *Burns*, **32**, 550–553.
18. H. E. van Herpt, M. J. Draijer, E. Hondebrink, M. N. Nieuwenhuis, G. Beerthuizen, T. G. van Leeuwen & W. Steenbergen (2009). "Burn imaging with a whole field laser Doppler perfusion imager based on a CMOS imaging array". *Burns*, **in press**.
19. S. W. Kim, S. C. Kim, K. C. Nam, E. S. Kang, J. J. Im & D. W. Kim (2008). "A new method of screening for diabetic neuropathy using laser doppler and photoplethysmography". *Medical & Biological Engineering & Computing*, **46**, 61–67.
20. A. Raabe, D. Van De Ville, M. Leutenegger, A. Szelényi, E. Hattingen, R. Gerlach, V. Seifert, C. Hauger, A. Lopez, R. Leitgeb, M. Unser, E. J. Martin-Williams & T. Lasser (2009). "Laser Doppler imaging for intraoperative human brain mapping". *NeuroImage*, **44**(4), 1284–1289.
21. K. Forrester, M. Doschak & R. Bray (1997). "In vivo comparison of scanning technique and wavelength in laser doppler perfusion imaging:

- Measurement in knee ligaments of adult rabbits”. *Medical & Biological Engineering & Computing*, **35**, 581–586.
22. A. K. Dunn, H. Bolay, M. A. Moskowitz & D. A. Boas (2001). “Dynamic imaging of cerebral blood flow using laser speckle”. *Journal of Cerebral Blood Flow and Metabolism*, **21**(3), 195–201.
 23. J. Kubota (2002). “Effects of diode laser therapy on blood flow in axial pattern flaps in the rat model”. *Lasers in Medical Science*, **17**, 146–153.
 24. F. F. M. de Mul, J. Blaauw, J. G. Aarnoudse, A. J. Smit & G. Rakhorst (2007). “Diffusion model for iontophoresis measured by laser-Doppler perfusion flowmetry, applied to normal and preeclamptic pregnancies”. *Journal of Biomedical Optics*, **12**(1), 14032–1.
 25. A. Serov, B. Steinacher & T. Lasser (2005). “Full-field laser Doppler perfusion imaging and monitoring with an intelligent CMOS camera”. *Optics Express*, **13**(10), 3681–3689.
 26. A. Serov & T. Lasser (2005). “High-speed laser Doppler perfusion imaging using an integrating CMOS image sensor”. *Optics Express*, **13**(17), 6416–6428.
 27. M. J. Draijer, E. Hondebrink, T. G. van Leeuwen & W. Steenbergen (2009). “The Twente Optical Perfusion Camera: system overview and performance for real time laser Doppler perfusion imaging”. *Optics Express*, **17**(5), 3211–3225.
 28. M. H. Koelink, F. F. M. de Mul, B. Leerkotte, J. Greve, H. W. Jentink, R. Graaff, A. C. M. Dassel & J. G. Aarnoudse (1994). “Signal processing for a laser-Doppler blood perfusion meter”. *Signal Processing*, **38**, 239–252.
 29. J. O. Hinze (1975). *Turbulence*. McGraw-Hill College.
 30. A. Humeau, J. L. Saumet & J. P. L. Huillier (2000). “Simplified model of laser Doppler signals during reactive hyperaemia”. *Medical & Biological Engineering & Computing*, **38**, 80–87.
 31. J. M. Bland & D. G. Altman (1986). “Statistical methods for assessing agreement between two methods of clinical measurement”. *The Lancet*, **1**, 307–310.

32. J. M. Bland & D. G. Altman (1995). “Comparing methods of measurement: why plotting difference against standard method is misleading”. *The Lancet*, **346**, 1085–1087.
33. S. W. Smith (1997). *The Scientist & Engineer’s Guide to Digital Signal Processing*. California Technical Pub., 1st ed edition ed.
34. M. G. D. Karlsson, H. Casimir-Ahn, U. Lönn & K. Wårdell (2003). “Analysis and processing of laser Doppler perfusion monitoring signals recorded from the beating heart”. *Medical & Biological Engineering & Computing*, **41**, 255–262.

6

**Relation between the
contrast in time integrated
dynamic speckle patterns
and the power spectral
density of their temporal
intensity fluctuations**

Abstract – Scattering fluid flow can be quantified with coherent light, either from the contrast of speckle patterns, or from the moments of the power spectra of intensity fluctuations. We present a theory connecting these approaches for the general case of mixed static-dynamic patterns of boiling speckles without prior assumptions regarding the particle dynamics. An expression is derived and tested relating the speckle contrast to the intensity power spectrum. Our theory demonstrates that in speckle contrast the concentration of moving particles dominates over the contribution of speed to the particle flux. Our theory provides a basis for comparison of both approaches when used for studying tissue perfusion.

6.1 Introduction

The speckle phenomenon is widely used for determining tissue perfusion maps [1, 2]. In general, the tissue is illuminated with coherent laser light. A fraction of the laser light interacts with moving red blood cells and obtains a Doppler shift. Doppler shifted and unshifted light which are diffusely scattered from the medium create a dynamic speckle pattern on a plane of observation. Various methods of analysing this speckle pattern have led to two separate modalities. In laser Doppler perfusion imaging (LDPI) [3] the power spectrum $P(\nu)$ of intensity fluctuations generated in the dynamic speckle pattern is analysed in terms of its moments given by :

$$M_i \equiv \int_{-\infty}^{\infty} \nu^i P(\nu) d\nu \quad (6.1)$$

where the zeroth order moment ($i = 0$) is a measure for the concentration of red blood cells and the first order moment ($i = 1$) is a measure for the flux or perfusion.

In the modality of laser speckle contrast methods, comprising laser speckle contrast analysis (LASCA) [4] and laser speckle imaging (LSI) [5] the contrast in the speckle pattern is used as a measure for perfusion [2]. In these techniques the changing speckle pattern is averaged over a time interval in the order of the speckle decorrelation-time (i.e. in the millisecond range) leading to speckle blurring. The level of blurring is quantified by the speckle contrast C , which is usually defined as the ratio of the standard deviation σ of the intensity I of the blurred image to the mean intensity $\langle I \rangle$ of the speckle pattern :

$$C \equiv \frac{\sigma}{\langle I \rangle} = \frac{\sqrt{\langle I^2 \rangle - \langle I \rangle^2}}{\langle I \rangle} \quad (6.2)$$

where the brackets denote spatial averaging. However, for ergodic speckle patterns, spatial and temporal averaging will give identical results. This will be the case for completely dynamic speckle patterns, hence without static component. The physics behind laser Doppler methods is well-known and it has been shown by Bonner and Nossal [3] that, for low blood concentrations, the concentration of red blood cells and their average velocity are both linearly represented by the perfusion estimation of equation 6.1. As yet, speckle contrast flowmetry modelling has focussed on retrieving velocity information of scattering particles rather than their flux which includes concentration [6–8]. The presence of a static speckle component is usually ignored, with two recent exceptions [8, 9]. Furthermore, models for speckle contrast flowmetry are inspired by Dynamic Light Scattering theories, implying assumptions regarding the dynamics of the particles and the associated optical intensity correlations, which is known to lead to model-dependent velocity estimations [7, 10]. Furthermore they often assume single scattering by moving particles. Here we present a theory which connects the contrast in time integrated dynamic speckle patterns and the power spectral density of temporal intensity fluctuations of non-integrated speckle patterns without prior assumptions regarding the speed distribution of particles and the extent of multiple scattering. The theory includes speckle patterns with an arbitrary large static component caused by the presence of non-Doppler shifted light. Linking speckle contrast flowmetry to a laser Doppler model may enable quantification in terms of flux rather than velocity only.

6.2 Theory

6.2.1 Transferfunction

We introduce time dependent function $f(t)$ and its moving average $u(t) = \frac{1}{T} \int_{t-T}^t f(\tau) d\tau$ with T the integration time. $F(\omega)$ and $U(\omega)$ are the Fourier transforms of $f(t)$ and $u(t)$ respectively. From general Fourier transform properties for time domain shifts and integrations [11], U and F are related as

$$U(T, \omega) = \frac{1}{i\omega T} [1 - \exp(-i\omega T)] F(\omega) \quad (6.3)$$

So the relation between $F(\omega)$ and $U(\omega)$ is given by the amplitude transfer function

$$H(T, \omega) = \frac{1}{i\omega T} [1 - \exp(-i\omega T)] \quad (6.4)$$

The gain $|H(T, \nu)|$ is given by :

$$|H(T, \nu)| = \frac{1}{T} \sqrt{\frac{1 - \cos(2\pi\nu T)}{2\pi^2\nu^2}} \quad (6.5)$$

and ν given in Hz. Figure 6.1 shows an example of $|H(T, \nu)|$ as a function of ν for integration times T of 1, 5 and 10 ms.

6.2.2 Contrast

Assume a blurred speckle pattern $I(x, t)$ in which blurring is realized by averaging a dynamic speckle pattern within window T . Assuming statistical homogeneity in time and space, this speckle pattern can be decomposed in an average value $\langle I \rangle$, a static, time independent spatial fluctuation $I_s(x)$ and a time- and space dependent fluctuation $I_T(x, t)$ which depends on the integration time T . Hence

$$I(x, t) = \langle I \rangle + I_s(x) + I_T(x, t) \quad (6.6)$$

I_s will be nonzero when part of the light producing the speckle pattern has a constant phase, for instance due to interaction with static objects only. For a fully dynamic speckle pattern, $I_s(x) = 0$ while for $T \rightarrow \infty$ also $I_T(x, t) \rightarrow 0$ and $I(x, t) \rightarrow \langle I \rangle$. These components are shown in figure 6.2 which features

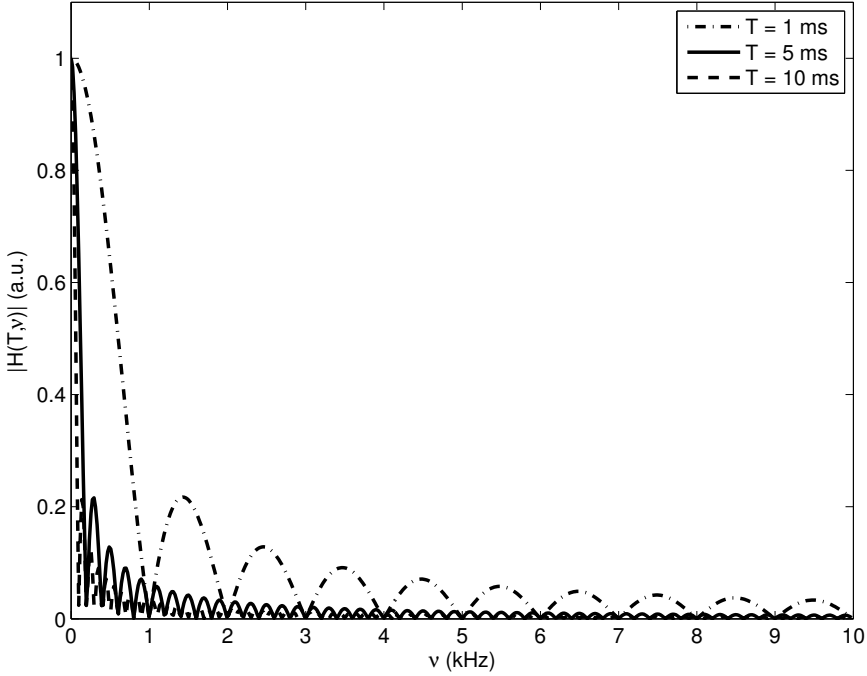


Figure 6.1: $|H(T, \nu)|$ for $T = 1$ ms, $T = 5$ ms and $T = 10$ ms.

an example of a blurred intensity I along a line in x -direction. Substituting the above form of $I(x, t)$ in equation 6.2 gives :

$$C^2 = \frac{\langle (I_s + I_T)^2 \rangle}{\langle I \rangle^2} = \frac{\langle I_s^2 \rangle + \langle I_T^2 \rangle}{\langle I \rangle^2} \quad (6.7)$$

where we assumed $\langle I_s I_T \rangle = 0$, since for each possible value of I_s , positive and negative values of I_T occur.

Furthermore, contrast as a function of integration time T can be written as :

$$C^2(T) = C^2(0) + \int_0^T \frac{dC^2}{d\tilde{T}} d\tilde{T} \quad (6.8)$$

6 Relation between contrast and power spectral density in dynamic speckle patterns

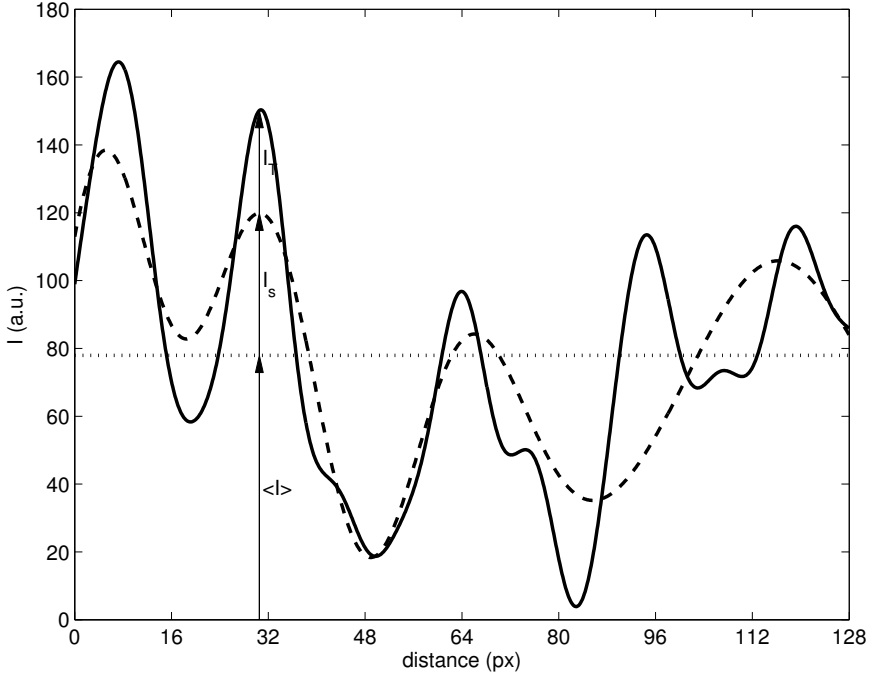


Figure 6.2: Decomposition of the blurred intensity I (solid) into average value $\langle I \rangle$ (dotted), static intensity fluctuation I_s (dashed) and time-dependent blurred fluctuation I_T .

The intensity in an unblurred polarised speckle pattern will have an exponential probability density function [12], so $C^2(0)$ equals unity. Since only $I_T(x, t)$ depends on T , substitution of equation 6.7 in equation 6.8 gives

$$C^2(T) = 1 + \frac{1}{\langle I \rangle^2} \int_0^T \frac{\partial}{\partial \tilde{T}} \langle I_T^2 \rangle d\tilde{T} \quad (6.9)$$

By using Parseval's theorem and the transfer function $H(T, \nu)$, $\langle I_T^2 \rangle$ can be written as :

$$\langle I_T^2 \rangle = \int_{-\infty}^{\infty} P(\nu) |H(T, \nu)|^2 d\nu \quad (6.10)$$

Substituting equation 6.10 into equation 6.9 results in :

$$C^2(T) = 1 + \frac{1}{\langle I \rangle^2} \int_{-\infty}^{\infty} P(\nu) \left[|H(T, \nu)|^2 \right]_0^T d\nu \quad (6.11)$$

which, using equation 6.1 with $i = 0$, reduces to

$$C^2(T) = 1 - \frac{M_0}{\langle I \rangle^2} + \frac{1}{\langle I \rangle^2} \int_{-\infty}^{\infty} P(\nu) |H(T, \nu)|^2 d\nu \quad (6.12)$$

since $|H(0, \nu)| = 1$. Equation 6.12 expresses the speckle contrast in terms of the power spectrum of the local temporal intensity fluctuations in the speckle pattern. For $T \downarrow 0$, it holds that $H(T, \nu) \rightarrow 1$ for all frequencies, reducing equation 6.12 to $C^2 = 1$, which is the required value for a snapshot of the speckle pattern. For $T \rightarrow \infty$, $H(T, \nu)$ approaches zero and the last term on the right-hand side cancels out, resulting in $C^2(T \rightarrow \infty) = 1 - M_0 / \langle I \rangle^2$. For a completely dynamic speckle pattern, the property of ergodicity leads to : $M_0 / \langle I \rangle^2 = 1$ so $C^2(T \rightarrow \infty) \rightarrow 0$. Hence, equation 6.12 shows the required behavior for extreme cases. Since $M_0 / \langle I \rangle^2 = f_D(2 - f_D)$ with f_D the fraction of Doppler shifted light [13] this limiting behavior agrees with the form given by Zakharov *et al.* [9].

6.3 Results

To validate equation 6.12, completely dynamic artificial speckle patterns are generated by making use of the concept of a copula [14] : a circular region in a square matrix is filled with complex numbers of unity amplitude and phases distributed uniformly between 0 and 2π . This matrix represents a uniform spatial distribution of complex electric field values. After Fourier transforming the matrix, and multiplying it point-by-point by its complex conjugate, an artificial speckle pattern is obtained. By shifting the circular region with complex numbers one column each time and recalculating the speckle pattern, a series of snapshots of a dynamic speckle pattern can be generated. For the speed of change of the speckle pattern, a time scale was chosen which was realistic for tissue speckle.

6 Relation between contrast and power spectral density in dynamic speckle patterns

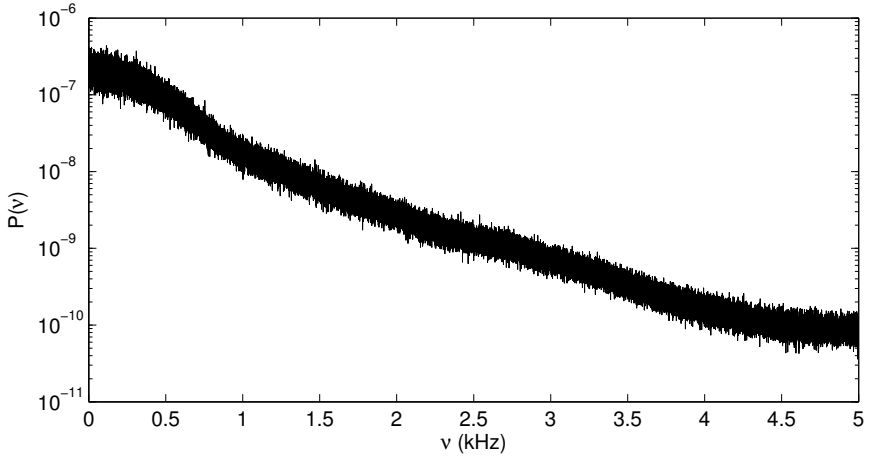


Figure 6.3: Power spectrum averaged over an area of 7×7 pixels of the artificial speckle pattern used to determine the spatial contrast.

From the dynamic speckle pattern, for 10 random pixels the time signal was extracted. Per pixel, from the time signal the contrast was determined from its definition in equation 6.2. Furthermore in each pixel, from the power spectrum of the time trace the contrast was predicted for different values of T using equation 6.12.

The spatial contrast is determined in concentric regions of 7×7 pixels around 10 random pixels. In each region, the contrast was determined from the definition in equation 6.12 as well as predicted by equation 6.2 based on the averaged power spectrum in the region. An example of an averaged power spectrum is shown in figure 6.3. The average contrast values and their standard deviations are shown in figure 6.4.

6.4 Discussion

Figure 6.4 shows that equation 6.12 allows for prediction of both temporal and spatial speckle contrast values based on the power spectra of the associated intensity fluctuations. There is a much better agreement between the measured and predicted contrast-curves for the case of temporal contrast

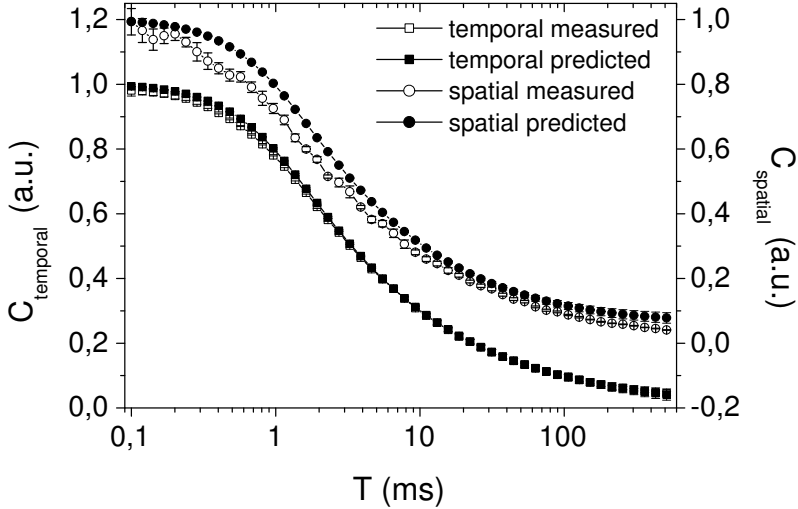


Figure 6.4: Measured (open symbols) and predicted (closed symbols) speckle contrast values for temporal (squares) and spatial (circles) contrast as a function of integration time T , for artificial speckles.

than for spatial contrast. Furthermore the error bars for temporal contrast are smaller than for spatial contrast. The discrepancy for the spatial contrast can be explained from the fact that in the limited region of interest of 7×7 pixels, the speckle pattern does not exhibit all intensity variations which are present in the complete speckle pattern. For integration time above 1 ms (i.e., which are normally used in speckle contrast techniques [2]) there is good agreement between the predicted and measured spatial contrast values. Note the fact that for integration times longer than half a second still the contrast did not reach zero, presumably due to low frequencies (e.g., below 1 Hz) which are present in the signal.

Given the suitability of the first order power spectral moment of intensity fluctuations as an estimator of particle flux within a static turbid matrix, as shown by Bonner and Nossal [3] for low particle flux, the expression derived in this paper for the contrast in blurred speckle forms the basis for further study of the degree of quantitation by speckle contrast techniques.

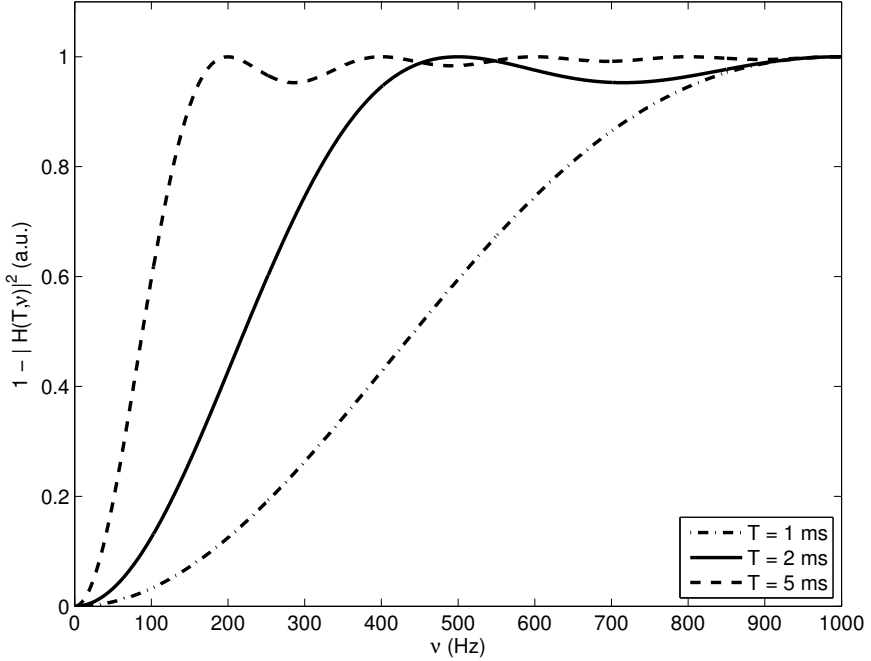


Figure 6.5: Spectral weighing functions realized by $1 - C^2$, with C the contrast of integrated speckle for integration times T of 1, 2 and 5 ms.

In this paper only a first step will be made. Clearly, equation 6.12 shows that speckle contrast provides an integral over the power spectrum $P(\nu)$ weighed with $|H(T, \nu)|^2$. A contrast function which is closest to the estimator proposed by Bonner and Nossal is $1 - C^2$, for which we can derive from equation 6.12 that :

$$1 - C^2 = \int_{-\infty}^{\infty} \left(1 - |H(T, \nu)|^2\right) P(\nu) d\nu \quad (6.13)$$

In figure 6.5 the spectral weighing function in equation 6.13 is shown for integration times of 1, 2 and 5 ms, respectively. The weighing function rises in a nonlinear manner from 0 to reach unity at $\nu = 1/T$. For $\nu > 1/T$ the weighing function shows decaying oscillations between 1 and 0.95. Hence, for integration times $5 \text{ ms} < T < 15 \text{ ms}$ realistic for speckle contrast

techniques, frequency weighing is only performed in a frequency interval between lower limit 0 Hz and higher limit $67 \text{ Hz} < \nu < 200 \text{ Hz}$. For higher frequencies, $1 - C^2$ mainly provides the zero order moment of the power spectrum. We must conclude that for realistic integration times, speckle contrast mainly provides information regarding the concentration of moving particles rather than their speed. Information about speed variations is only conveyed inasmuch as these variations affect the spectral broadening in the interval $0 < \nu < 1/T$ (in Hz). In this interval the frequency weighing is nonlinear, with an approximately 2^{nd} order weighing ($\propto \nu^2$) for $\nu \rightarrow 0$. The second order weighing can be extended to higher frequencies by reducing integration time T . For instance for the power spectrum shown in figure 6.3, with a width of 5 kHz which is typical for physiological perfusion, a second order weighing of the entire power spectrum would be obtained for an integration time of approximately 0.1 ms. This is an impractical value, since for this integration time the contrast will only be marginally smaller than 1, as shown by figure 6.4. For other flux estimators which provide higher values for lower contrast, such is $1/C$ a similar analysis may be made, although this will be mathematically less elegant.

6.5 Conclusion

In this paper, we have presented a theory which expresses the contrast in time integrated dynamic speckle patterns in terms of the power spectral density of their local temporal intensity fluctuations. The theory covers mixed static-dynamic speckle patterns, provided that they are statistically homogeneous. Verification was done with the use of fully dynamic speckle patterns which were created numerically. From our theory we can conclude that for realistic integration times $T > 5 \text{ ms}$, speckle contrast mainly provides information regarding the concentration of particles moving within a static matrix, with speed information only present for the lower end of the power spectrum. The presented theory will enable a further quantitative investigations into the use of speckle contrast as an estimator for tissue perfusion.

References

1. P. Vennemann, R. Lindken & J. Westerweel (2007). “In vivo whole-field blood velocity measurement techniques”. *Experiments in Fluids*, **42**(4), 495–511.
2. M. J. Draijer, E. Hondebrink, T. G. van Leeuwen & W. Steenbergen (2009). “Review of laser speckle contrast techniques for visualizing tissue perfusion”. *Lasers in Medical Science*, **24**(4), 639–651.
3. R. Bonner & R. Nossal (1981). “Model for laser Doppler measurements of blood flow in tissue”. *Applied Optics*, **20**(12), 2097–2107.
4. J. D. Briers & S. Webster (1996). “Laser speckle contrast analysis (LASCA): a non-scanning, full-field technique for monitoring capillary blood flow”. *Journal of Biomedical Optics*, **1**, 174–179.
5. H. Cheng, Q. Luo, S. Zeng, S. Chen, J. Cen & H. Gong (2003). “Modified laser speckle imaging method with improved spatial resolution.” *Journal of Biomedical Optics*, **8**(3), 559–564.
6. J. D. Briers & S. Webster (1995). “Quasi real-time digital version of single-exposure speckle photography for full-field monitoring of velocity or flow fields”. *Optics Communications*, **116**, 36–42.
7. J. C. Ramirez-San-Juan, R. Ramos-Garcia, I. Guizar-Iturbide, G. Martinez-Niconoff & B. Choi (2008). “Impact of velocity distribution assumption on simplified laser speckle imaging equation”. *Optics Express*, **16**(5), 3197–3203.
8. A. B. Parthasarathy, W. J. Tom, A. Gopal, X. Zhang & A. K. Dunn (2008). “Robust flow measurement with multi-exposure speckle imaging”. *Optics Express*, **16**(3), 1975–1989.
9. P. Zakharov, A. Völker, A. Buck, B. Weber & F. Scheffold (2006). “Quantitative modeling of laser speckle imaging”. *Optics Letters*, **31**(23), 3465–3467.
10. D. D. Duncan & S. J. Kirkpatrick (2008). “Can laser speckle flowmetry be made a quantitative tool?” *J. Opt.Soc.Am.A*, **25**(8), 2088–2094.
11. P. A. Lynn (1986). *Electronic signals and systems*. Macmillan, London.

12. J. W. Goodman & G. Parry (1975). *Laser Speckle and Related Phenomena*. Springer-Verlag, New York.
13. A. Serov, W. Steenbergen & F. F. M. de Mul (2001). “Prediction of the photodetector signal generated by Doppler-induced speckle fluctuations: theory and some validations”. *J. Opt. Soc. Am. A*, **18**(3), 622–630.
14. D. D. Duncan, S. J. Kirkpatrick & R. K. Wang (2008). “Statistics of local speckle contrast”. *Journal of the Optical Society of America A: Optics and Image Science, and Vision*, **25**(1), 9–15.

7

Summary and Outlook

Abstract – In this chapter a summary will be presented on high-speed laser Doppler perfusion imaging and laser speckle contrast techniques, as described in this thesis. An outlook to future improvements and applications of the instrument and techniques will be given.

7.1 Summary

Noninvasive methods to visualize blood flow in tissue are important in the clinical environment. Most methods use dynamic speckles to measure the level of perfusion. Speckle patterns are random interference pattern due to diffusely backscattered light from the skin. The most well-known techniques based on these speckle patterns are laser Doppler perfusion imaging (LDPI) and laser speckle contrast analysis (LASCA). Till recently, the advantage of the latter over the former was its being a fast full field technique rather than a point scanning technique. This advantage decreased by the introduction of high speed CMOS cameras for the detection of the Doppler-shifted light in LDPI. From that moment on, both techniques had a measurement time in the millisecond range. However, LASCA and similar laser speckle contrast techniques are still gaining interest [1, 2]. For LASCA measurements an inexpensive camera which can achieve a frame-rate of 200 Hz is sufficient, whereas for LDPI, only a state-of-the-art high-speed camera which can achieve a frame-rate of about 25 kHz is suitable.

Laser speckle contrast techniques are based on the spatial and temporal statistics of the speckle pattern. The motion of particles in the illuminated medium causes fluctuations in the speckle pattern on the detector. These intensity fluctuations blur the image and reduce the contrast to an extent that is related to the speed of the illuminated objects, such as moving red blood cells. A review of laser speckle contrast techniques so far, and a comparison of these techniques on the hand of a volunteer (figure 2.5) is

given in **chapter 2**. Laser speckle contrast techniques have advantages over their main counterpart, LDPI. Laser speckle contrast techniques need only one or a few frames to determine the tissue perfusion, which makes it fast. They also need a low frame rate camera only, which makes them relatively inexpensive. But they also have one major disadvantage with respect to LDPI; the readings in LDPI can be related to the Doppler effect which is described by Bonner and Nossal [3]; a theory which is widely accepted and understood. For laser speckle contrast techniques this is not the case, since, for example, it is still unknown which velocity distribution (e.g. Voigt, Lorentzian or Gaussian; see figure 2.2) should be used. The need to assume a specific velocity distribution to relate the speckle contrast to the tissue perfusion makes the technique less generally applicable.

In commercially available LDPI devices the area under investigation is scanned with a narrow laser beam, which is time consuming, leading to measurement times of several minutes. This long scanning time impedes the observation of fast perfusion changes (e.g. during reperfusion after occlusion) and is uncomfortable for the subject. To obtain real time perfusion images, a refresh rate of approximately 25 Hz is needed. In **chapter 3** the Twente Optical Perfusion Camera (TOPCam), an imaging system based on high-speed CMOS technology is presented. Based on an overall analysis of the signal-to-noise ratio of CMOS cameras (figure 3.3), the best camera for our purpose was selected. Pixel-by-pixel noise correction was applied to minimize the influence of noise in the perfusion images (figure 3.5). Experiments are presented which show that a frame rate of 0.2 fps for an image of 128×128 pixels (imaged tissue area of 7×7 cm²) can be achieved if the data is analyzed online. If the analysis of the data is performed offline, a frame rate of 26 fps can be achieved for a duration of 3.9 seconds (figure 3.8). By reducing the imaging size to 128×16 pixels, this frame rate can be achieved for up to half a minute. Due to this high frame rate and long imaging time, fast changing perfusion levels (e.g., the heart beat in figure 3.8) can be visualized.

The TOPCam was used to evaluate the capability and efficacy of the TOPCam to measure perfusion differences in burn wounds. In **chapter 4** these first clinical results of the TOPCam in the setting of a burn centre are presented. Several superficial partial thickness burns are imaged on 23 patients. If increased perfusion indicates spontaneous healing within two weeks, the images showed good agreement with the outcome in terms of healing capacity. The measurements also indicate that the spatial image resolution of

the TOPCam is sufficient for the diagnostic purposes in a burn centre. The TOPCam encounters problems caused by blisters, tissue necrosis, surface reflection and curvature in a manner similar to scanning beam imagers. Image quality in terms of dynamic range and resolution appears to be sufficient for burn diagnosis, and it poses a clear advantage in terms of procedure time with respect to scanning beam imagers.

In LDPI, the perfusion in one pixel is usually calculated by recording a complete time signal (e.g. 512 or 1024 points), determine the power spectrum using the Fast Fourier Transform (FFT), and obtain the first order moment of the power spectrum as a measure for the flux or perfusion. Calculating the perfusion using the FFT is time consuming because it has to be taken for each pixel and the spectrum has to be squared and integrated over all frequencies to obtain one number for the perfusion. Furthermore, this procedure puts high demands on the camera memory and data communication between camera and computer. In **chapter 5**, a Time Domain (TD) algorithm is presented for determining the first order spectral moment. This algorithm involves multiplications of an image with the difference between two subsequent images. It is shown by experiments on phantoms and in-vivo (figure 5.2 and 5.3) that the TD-algorithm can be a good alternative for the FFT-algorithm. A comparison based on a Bland-Altman analysis shows that the systematic difference between the TD algorithm and FFT algorithm is approximately 15%. In view of the inherent heterogeneity of perfusion and perfusion images, this difference is not likely to lead to a different diagnosis or conclusion regarding the tissue physiology. The TD-algorithm can determine the perfusion in LDPI twice as fast as the FFT-algorithm (figure 5.5) and gives equivalent perfusion images. Furthermore the TD-algorithm gives the possibility to perform on-the-fly estimation because it only needs a few new frames to update a previous perfusion estimation. This results in lower memory requirements compared to the memory needed to perform an FFT, which is a major advantage of the TD-algorithm.

The issue of the relation between the competing methods of laser Doppler perfusion imaging and laser speckle contrast methods is addressed in **chapter 6**. A theory is developed which expresses the contrast in time integrated dynamic speckle patterns in terms of the power spectral density of their local temporal intensity fluctuations. The theory is based on the spectral transfer function associated with the integration operation carried out by the image sensor. An expression is derived for the general case of mixed static-dynamic patterns of boiling speckles without prior assumptions re-

garding the particle dynamics. The theory was validated with the use of fully dynamic speckle patterns which were created numerically. The theory indicates that for realistic integration times (e.g. integration times > 5 ms), speckle contrast mainly provides information regarding the concentration of particles moving within a static matrix, as far as speed variations affect the low frequencies of the power spectrum of the photocurrent fluctuations (for an integration time of 5 ms: the range between 0 and 200 Hz). The theory can provide that foundation for future comparison between the LDPI and LASCA techniques for specific applications.

7.2 Outlook

7.2.1 CMOS technology

Our practical experience during the clinical trials in the setting of a burn centre learns that the scanning beam laser Doppler perfusion imagers have a better signal-to-noise ratio compared to the TOPCam. Due to the different amplifiers for different pixel columns in the CMOS chip, fixed pattern noise will be induced in the measurements, resulting in images which are noisier than those produced by scanning beam imagers. In newer CMOS-cameras, already a smaller fixed pattern noise is observed, so further technological sophistication will probably solve, or at least reduce, this issue drastically. When the fixed pattern noise is eliminated, the amount of noise does not differ significantly anymore from day to day, which improves the estimation of the noise level. Improvement of the noise estimation reduces the under- or overestimation of the perfusion level. Whole field LDPI may be further optimized by designing CMOS arrays optimized for this task, such as done by Gu *et al.* [4]. For instance, each pixel might be provided with separate outputs for the AC and DC parts of the laser Doppler signal, and further conditioning of the AC output to exploit the dynamic range of the analog-to-digital converters.

Table 3.2 shows that the most time consuming part in the imaging process of the TOPCam, is the transfer of data from the camera to the computer to process the data. This process can be accelerated by improving the protocol to utilize the full bandwidth during the transfer. By implementing the discretized version of the time domain-algorithm of **chapter 5** on

CMOS-cameras with programmable memory, this part can even be eliminated. When data-processing is performed on the camera, only the final perfusion images have to be transported to the computer. This improvement also increases the frame rate achievable with online data analysis. With the current measurement setup, every 5 seconds a new perfusion image of 128×128 pixels can be produced. When the discretized version of the TD-algorithm is implemented, it should be achievable to produce a new perfusion image of that size every 1 or 2 seconds, leading to a frame rate up to 1 fps instead of 0.2 fps. With a moving average approach implemented on the camera it may be possible to even further improve the speed of the process, eventually leading to real-time online analysis at a high frame rate.

7.2.2 LASCA versus LDPI

LDPI and LASCA are increasingly competing techniques for imaging blood flow in tissue in a non-invasive manner. Each technique has its own advantages and disadvantages. LASCA can already be performed with a low frame rate camera, which makes it a relatively inexpensive technique compared to LDPI. However, in LDPI the readings can be related to the Doppler effect which is described by Bonner and Nossal [3]. This theory is widely accepted and understood, which is not the case for LASCA. Once there is consensus about a theoretical model for LASCA which connects the contrast unambiguously to the perfusion level, it can become the major technique for measuring blood flow in tissue. Until that, for applications where visualizing of areas with and without perfusion is more important than relative perfusion (e.g. after skin grafting), LASCA is a suitable technique. For other applications where the level of perfusion and its change over time is more important (e.g. healing of burn wounds) LDPI is more suitable.

In **chapter 6** a first initiative was made for a theoretical model linking the contrast to the perfusion level. However, verification was done with the use of speckle patterns which were created numerically. Further investigation and verification of this theoretical model should be done based on measurements on phantoms or on in-vivo measurements.

7.2.3 Applications

In this thesis, the first clinical results of the TOPCam in the setting of a burn centre have been shown and the image quality in terms of dynamic range and resolution appeared to be sufficient for burn diagnosis. However, further research is needed to characterize the imaging quality and imaging properties (e.g., measurement depth, resolution, response to different tissue types) of the TOPCam with respect to scanning beam laser Doppler perfusion imagers in visualizing burns.

Besides imaging burns to predict the burn wound outcome in an early stage, there are other applications in which the TOPCam can have an added value. For example during organ transplantation (e.g. liver, kidney, etc.) where the surgeon with a quick check with the TOPCam, can see if the arteries and veins are all attached correctly. During coronary artery bypass grafting, the TOPCam can be used to measure the perfusion in the myocardial tissue to see if the intervention is successful. A final example is the potential improvement of intestinal anastomoses quality after removal of a part of the intestine. In this procedure, adequate reperfusion is essential to prevent intestinal ischemia, which is a life-threatening condition.

In chronic wound care, the TOPCam can be used to regularly image patients which have an increased chance on ulcers (i.e. diabetic ulcers or pressure ulcers), to monitor their perfusion in areas of risk. Due to the fast imaging speed of the TOPCam, this becomes a quick procedure which disturb the patient just minimal. If a decrease in perfusion is noticed, treatment can be started or adjusted.

In dermatology, during laser treatment of port wine stains, moles or other type of nevus, the TOPCam can be used to measure the perfusion in the treated region during and after the therapy. In this way the perfusion level can be monitored, and in case of an irregular trend, the physician can decide to intervene to prevent irreversible damage to the skin.

If the TOPCam is equipped with the possibility to illuminate with an array of beams rather than with a large square shaped beam, the TOPCam can also be used to obtain depth-differentiated perfusion images [5]. In this way superficial perfusion can be separated from deep perfusion.

Fast laser Doppler perfusion imaging is possible with the TOPCam, and contrast in laser speckle contrast techniques can be related to perfusion,

so a whole new range of clinical applications has come into reach because dysfunction in organs is often related to inadequate perfusion of the organs. With a small laser diode and camera, LDPI and LASCA can even be implemented in endoscopes, which opens a new clinical field: now the perfusion in the bladder, the intestine and the esophagus can be imaged noninvasively.

References

1. J. D. Briers (2001). “Laser Doppler, speckle and related techniques for blood perfusion mapping and imaging”. *Physiological Measurements*, **22**, R35–R66.
2. J. D. Briers (2007). “Laser speckle contrast imaging for measuring blood flow”. *Optica Applicata*, **XXXVII**, 139–152.
3. R. Bonner & R. Nossal (1981). “Model for laser Doppler measurements of blood flow in tissue”. *Applied Optics*, **20**(12), 2097–2107.
4. Q. Gu, B. R. Hayes-Gill & S. P. Morgan (2008). “Laser Doppler blood flow complementary metal oxide semiconductor imaging sensor with analog on-chip processing”. *Applied Optics*, **47**(12), 2061–2069.
5. B. Varghese, V. Rajan, T. G. van Leeuwen & W. Steenbergen (2007). “Path-length-resolved optical Doppler perfusion monitoring”. *Journal of Biomedical Optics*, **12**(6), 060508.

Nederlandse samenvatting

Technieken om niet-invasief de doorbloeding van weefsel te meten zijn een belangrijke bron van informatie in een klinische omgeving. De meeste van deze technieken zijn gebaseerd op ‘speckle’ patronen (vlekkenpatronen door interferentie van gereflecteerd licht). De bekendste technieken die gebruik maken van zo’n specklepatroon zijn ‘laser Doppler perfusion imaging’ (LDPI) en ‘laser speckle contrast analysis’ (LASCA). Tot voor kort had de laatste als voordeel dat deze een ‘full field’ techniek was in plaats van een techniek die het oppervlakte scant. Dit voordeel verdween door de introductie van hogesnelheid CMOS-camera’s voor het detecteren van Doppler-verschoven licht in LDPI. Vanaf dat moment hadden beide technieken een meettijd in de orde van milliseconden. Toch zijn LASCA en andere laser contrast technieken nog wel in opmars [1, 2]. Voor LASCA metingen is namelijk een simpele camera met een framerate van 200 Hz voldoende, terwijl voor LDPI een ‘state-of-the-art’ hogesnelheidscamera met een framerate van 25 kHz noodzakelijk is.

Laser speckle contrast technieken zijn gebaseerd op de ruimtelijke- en tijdsafhankelijke statistiek van het specklepatroon. De beweging van deeltjes in het belichte medium veroorzaakt fluctuaties in de intensiteit van het specklepatroon op de detector. Deze fluctuaties vervagen het beeld, en verlagen daardoor het contrast op een manier die afhankelijk is van de snelheid van de bewegende deeltjes, bijvoorbeeld rode bloedcellen. Een overzicht van bestaande laser speckle contrast technieken en een vergelijking van de resultaten met deze technieken op menselijk weefsel is gegeven in **hoofdstuk 2**. Laser speckle contrast technieken hebben voordelen ten opzichte van hun belangrijkste concurrent, LDPI. Laser speckle contrast technieken zijn sneller omdat ze slechts één of slechts enkele frames nodig hebben om de doorbloed-

ing in weefsel te kunnen bepalen. Zij hebben bovendien voldoende aan een camera met een lage framerate, wat ze relatief goedkoop maakt. Zij hebben echter een groot nadeel ten opzichte van LDPI; de uitkomst van LDPI kan gerelateerd worden aan het Doppler-effect wat beschreven is door een theorie welke breed geaccepteerd en begrepen is. Voor laser speckle contrast technieken is dit echter niet het geval, omdat bijvoorbeeld nog steeds onduidelijkheid is welke snelheidsdistributie (Voigt, Lorentziaans of Gaussisch) aangenomen moet worden. De noodzaak voor het doen van deze aanname om het contrast te kunnen relateren aan de doorbloeding van het weefsel, maakt deze techniek minder goed algemeen bruikbaar.

In de LDPI apparaten die momenteel op de markt zijn wordt het te onderzoeken oppervlakte gescand met een smalle laserbundel. Het scannen van het hele oppervlak neemt veel tijd in beslag, dit leidt tot meettijden van enkele minuten. Deze lange meettijd verhindert het waarnemen van snelle doorbloedingveranderingen (bijvoorbeeld reperfusie na een occlusie) en is onaangenaam voor de patiënt. Om realtime perfusie opnames te maken, is een framerate van ongeveer 25 Hz nodig. In **hoofdstuk 3** is de “Twente Optical Perfusion Camera” (TOPCam) gepresenteerd, een systeem gebaseerd op hogesnelheid CMOS technologie. Uitgaande van een algemene analyse van de signaal-ruis-verhouding van CMOS camera’s, is de meest optimale camera voor ons doel geselecteerd. Pixel-voor-pixel ruiscorrectie is toegepast om de invloed van ruis op de perfusiebeelden te minimaliseren. Ook worden er metingen getoond die laten zien dat als de data online geanalyseerd wordt, een framerate van 0,2 beelden per seconden haalbaar is voor opnames van 128×128 pixels (een gebied van 7×7 cm²). Als de analyse van de data offline plaatsvindt, kan een framerate van 26 beelden per seconde gehaald worden voor een duur van 3,9 seconden. Wordt de beeldgrootte verlaagd tot 128×16 pixels, dan kan deze framerate gedurende een halve minuut gehaald worden. Door deze hoge framerate in combinatie met de relatief lange periode die getoond kan worden, kunnen snelle variaties in de doorbloeding (zoals bijvoorbeeld ten gevolge van de hartslag) getoond worden.

De mogelijkheden van de TOPCam om doorbloedingsverschillen in brandwonden te meten zijn onderzocht. In **hoofdstuk 4** zijn deze eerste klinische testen van de TOPCam in een brandwondencentrum gepresenteerd. Bij 23 patiënten zijn verschillende oppervlakkige tweedegraads brandwonden gemeten. Als verhoogde doorbloeding een indicatie is voor spontane genezing binnen twee weken, vertonen de opnames een goede overeenkomst met het genezingsvermogen. De metingen hebben ook aangetoond dat de ruimtelijke

resolutie van de TOPCam voldoende is voor diagnostische doeleinden in een brandwondencentrum. De TOPCam ondervindt dezelfde soort problemen bij blaren, weefselnecrose, reflectie en rondingen als de bestaande scannende apparaten. Verder blijkt de beeldkwaliteit in termen van dynamische bereik en resolutie voldoende voor de diagnose van brandwonden, en heeft de TOPCam in vergelijking met bestaande scannende apparaten een duidelijk voordeel voor wat betreft de meettijd.

Gewoonlijk wordt in LDPI de doorbloeding in een pixel berekend door het complete tijdsignaal van een pixel (bv 512 of 1024 punten) op te slaan en het vermogenspectrum van dit tijdsignaal te berekenen met de Fast Fourier Transformatie (FFT). Vervolgens wordt het eerste moment van het vermogenspectrum genomen als een maat voor de doorbloeding. Het berekenen van de doorbloeding op basis van de FFT neemt veel tijd in beslag omdat dit voor elke pixel afzonderlijk gedaan moet worden en omdat het spectrum gekwadeerd en geïntegreerd moet worden over alle frequenties om één getal te krijgen als maat voor de doorbloeding. Bovendien stelt dit hoge eisen aan het geheugen in de camera en de communicatie tussen camera en computer. In **hoofdstuk 5** is een Tijd Domein (TD) algoritme gepresenteerd voor het berekenen van het eerste spectrale moment. Het algoritme bevat het vermenigvuldigen van een opname met het verschil ten opzichte van de vorige opname. Op basis van zowel metingen op fantomen als in-vivo metingen is aangetoond dat het TD-algoritme een goed alternatief is voor het FFT-algoritme. Een vergelijking op basis van Bland-Altman analyse laat zien dat het systematische verschil tussen het TD-algoritme en het FFT-algoritme ongeveer 15% is. Gezien heterogeniteit in weefseldoorbloeding in de praktijk, is het niet waarschijnlijk dat dit verschil zal leiden tot een andere diagnose of conclusie met betrekking tot de fysiologie van het weefsel. Het TD-algoritme kan de doorbloeding in LDPI twee keer zo snel berekenen als het FFT-algoritme maar geeft gelijkwaardige resultaten. Verder biedt het TD-algoritme de mogelijkheid om on-the-fly benaderingen te doen omdat er slechts enkele nieuwe opnames nodig zijn om de vorige benadering aan te passen. Dit stelt lagere eisen aan het benodigde geheugen op de camera, wat een groot voordeel is van het TD-algoritme boven het FFT algoritme.

De relatie tussen de concurrerende technieken van laser Doppler perfusion imaging en laser speckle contrast analysis komt in **hoofdstuk 6** aan bod. Er is een theorie ontwikkeld die het contrast van in tijd geïntegreerde dynamische specklepatronen uitdrukt in termen van de intensiteitfluctuaties in de tijd van het vermogenspectrum. De theorie is gebaseerd op de spectrale

overdrachtsfunctie die hoort bij de integratie zoals die door de beeldsensor uitgevoerd wordt.

Er is een uitdrukking afgeleid voor het algemene geval van een gemengd statisch-dynamische patroon van ‘boiling’ speckles waarbij geen rekening is gehouden met de dynamica van deeltjes. De theorie is gevalideerd met behulp van volledig dynamische specklepatronen die numeriek gegenereerd waren. De theorie laat zien dat voor realistische integratietijden (bv integratietijden > 5 ms), het specklecontrast hoofdzakelijk informatie bevat met betrekking tot de concentratie van bewegende deeltjes, omdat snelheidsvariëaties enkel de lage frequenties van het vermogensspectrum van de intensiteitsfluctuaties beïnvloeden (voor een integratietijd van 5 ms: het gebied tussen 0 en 200 Hz). Deze theorie kan de basis vormen voor verder onderzoek naar het verbinden van LDPI en LASCA voor specifieke toepassingen.

Bibliografie

1. J. D. Briers (2001). “Laser Doppler, speckle and related techniques for blood perfusion mapping and imaging”. *Physiological Measurements*, **22**, R35–R66.
2. J. D. Briers (2007). “Laser speckle contrast imaging for measuring blood flow”. *Optica Applicata*, **XXXVII**, 139–152.

Dankwoord

Na 4 jaar full-time onderzoek en bijna een jaar part-time schrijven ben ik dan eindelijk zo ver dat mijn proefschrift af is. Op de omslag en op het titelblad staat dan wel alleen mijn naam, dat wil niet zeggen dat ik het allemaal alleen gedaan heb.

Om te beginnen had ik hulp van Erwin, mijn technicus. Hoeveel promovendi kunnen zeggen dat ze een eigen technicus hadden; een technicus voor zichzelf... ik had die luxe. Erwin, dank voor je LabVIEW- & electronica-kennis waar ik dankbaar gebruik van heb mogen maken, en dank je voor de plezierige tijd we hadden met het knutselen aan de TOPCam en de reisjes naar Stockholm en Utrecht.

Dank ook aan Wiendelt die een dag na mijn afstuderen informeerde hoe mijn sollicitatiegesprek die dag bij een andere universiteit in Nederland was gegaan, en *en-passant* een interessant promotieonderzoek onder mijn aandacht bracht. Het sollicitatiegesprek dat volgende was een interessant toneelstukje, en de uiteindelijke uitkomst ligt hier voor ons.

Wiendelt, een congres is volgens mij voor jou een soort retraite : als jij was weggeweest kon je rekenen op een wiskundige afleiding van het een of ander. Dit is uiteindelijk toch de basis geworden van hoofdstuk 5 & 6. Mijn dank daarvoor.

Ton, hoewel jij het meeste begeleiden hebt moeten overgedragen aan Wiendelt, en wij elkaar daardoor niet heel veel spraken, bleek jij toch een goed beeld van mijn sterke en zwakke punten te hebben. Dat werd duidelijk toen jij tijdens de sabbatical van Wiendelt het functioneringsgesprek van hem mocht -of moest- overnemen. Ik was aangenaam verrast.

Roy, ik denk ook met veel plezier terug aan onze tijd bij BPE. Je begon als

mijn afstudeerbegeleider, waarna je binnen enkele jaren promotie maakte tot collega en kamergenoot. Dat je dat laatste binnen een paar maanden voor gezien hield en naar de overkant van de gang verhuisde en mij alleen achterliet in “*Little India*” heb ik je ondertussen vergeven.

Roy, hoewel jouw onderzoek een heel andere kant op ging dan het mijne, was jij toch een vraagbaak voor allerlei kleinere en grotere vraagstukken, mijn dank daarvoor. Met plezier denk ik ook terug aan de lol en gezelligheid die we in het lab en op & onderweg naar congressen hadden.

Babu, Vinay and Kiran, thank you for tolerating me in Hogekamp as a Dutchman in “Little India”. It was always interesting to see your astonishment about some Dutch uses and habits, just as well as I was astonished by some of your uses and habits. Thanks to these cultural differences, we had a nice atmosphere in our office and in the laboratory.

Ook Erik, Ganeshram, Bart en Liesbeth, mijn ‘nieuwe’ kamergenoten in de Zuidhorst, bedankt voor de gezelligheid en gespreken over al dan niet biochemische en biofysische onderwerpen.

Heleen, jij als master-afstudeerder en gedeelde eerste auteur van een van de artikelen, maar ook Koen, Jurjen, Peter en Justin, jullie als bachelor-afstudeerders, hartelijk dank voor het werk wat jullie hebben gedaan. Ik vond het leuk om jullie te begeleiden bij de verschillende projecten.

Bjorn, Hans-Eric, Frederik, Daniel and all other Perimed-employees, thanks for your cooperation in the research and the nice high-speed camera you bought us. Hopefully I’ll see the TOPCam commercially available within a couple of years.

Collega BMO’ers : hartelijk dank voor de werkbesprekingen de afgelopen jaren. Ondanks dat ik soms het gevoel had als enige op de centimeter en seconde-schaal bezig te zijn, en weinig tot niks met chemie van doen had, waren het toch vaak leerzame uurtjes. Dank voor de opbouwende opmerkingen en slimme ideeën die ik van jullie kreeg.

Sylvia, bedankt voor de leuke tijd binnen BPE en je ondersteuning bij de minder wetenschappelijke kanten van het onderzoek : als er weer wat geregeld moest worden wist jij bijna altijd bij wie ik moest zijn of welk formulier daarvoor nodig was.

En last-but-not-least : Marjon dank je voor de steun die je gaf bij het afronden van mijn proefschrift, Benne dank voor het ontwerpen van de omslag

van mijn proefschrift, en pap dank je voor het corrigeren van de Nederlandse teksten.

Publications

Published

M.J. Draijer, E. Hondebrink, T.G. van Leeuwen & W. Steenbergen (2006). “Novel approaches in perfusion imaging of superficial microcirculation”. *Journal of Vascular Research*, **43**(Suppl. 1), 5.

M.J. Draijer, E. Hondebrink, W. Steenbergen & T.G. van Leeuwen (2007). “Laser Doppler perfusion imaging with a high-speed CMOS-camera”. In C.D. Depeursinge (ed.) *Novel Optical Instrumentation for Biomedical Applications III, Proc. SPIE*, vol. 6631, p. 66310N.

M.J. Draijer, E. Hondebrink, T.G. van Leeuwen & W. Steenbergen (2008). “Connecting laser Doppler perfusion imaging and laser speckle contrast analysis”. In G.L. Coté & A.V. Priezzhev (eds.) *Optical Diagnostics and Sensing VIII, Proc. SPIE*, vol. 6863, pp. 68630C–68630C–8.

M.J. Draijer, E. Hondebrink, T.G. van Leeuwen & W. Steenbergen (2009). “Review of laser speckle contrast techniques for visualizing tissue perfusion”. *Lasers in Medical Science*, **24**(4), 639–651.

M.J. Draijer, E. Hondebrink, T.G. van Leeuwen & W. Steenbergen (2009). “The Twente Optical Perfusion Camera: system overview and performance for real time laser Doppler perfusion imaging”. *Optics Express*, **17**(5), 3211–3225.

M.J. Draijer, E. Hondebrink, T.G. van Leeuwen & W. Steenbergen (2009). “Time domain algorithm for accelerated determination of the first order moment of photo current fluctuations in high speed laser Doppler perfusion

imaging”. *Medical & Biological Engineering & Computing*, **47**(10), 1103–1109.

In Press

H.E. van Herpt, M.J. Draijer, E. Hondebrink, M.N. Nieuwenhuis, G. Beerthuizen, T.G. van Leeuwen & W. Steenbergen (2009). “Burn imaging with a whole field laser Doppler perfusion imager based on a CMOS imaging array”. *Burns*.

Curriculum Vitae

Matthijs Draijer is geboren op 22 maart 1980 in Almelo. Het grootste gedeelte van zijn basisschooltijd heeft hij echter doorlopen in Arnhem op de Pieter Jongelingschool, waarna hij in 1998 zijn VWO-diploma haalde op het Greijdanus College in Zwolle. In 2004 rondde Matthijs zijn studie Technische Natuurkunde aan de Universiteit Twente binnen de vakgroep Biofysische Technieken (BFT) af met het onderzoek “A method to determine the blood content in superficial tumors using photo acoustics”, een onderzoek naar de mogelijkheid om met fotoakoestiek (geluid opwekken door middel van korte laserpulsen) de dichtheid van bloedvaten in oppervlakkige huidtumoren te bepalen. Kort na het afronden van deze studie is hij in januari 2005 aan dezelfde universiteit en binnen dezelfde vakgroep begonnen met zijn promotieonderzoek waarvan dit proefschrift de neerslag is.

Sinds 15 december 2008 is hij werkzaam als klinisch fysicus in opleiding met als specialisatie algemene klinische fysica in een gecombineerde aanstelling bij het Spaarne Ziekenhuis in Hoofddorp en het VU Medisch Centrum in Amsterdam. Vanuit het Spaarne Ziekenhuis is hij gestationeerd in het Kenemer Gasthuis in Haarlem.